

**Search for New Massive Long-Lived Neutral Particles
decaying to Photons in pp Collisions at $\sqrt{S} = 8$ TeV**

A DISSERTATION
SUBMITTED TO THE FACULTY OF THE GRADUATE SCHOOL
OF THE UNIVERSITY OF MINNESOTA
BY

Tambe Ebai Norbert

IN PARTIAL FULFILLMENT OF THE REQUIREMENTS
FOR THE DEGREE OF
Doctor of Philosophy

Prof. Yuichi Kubota

July, 2015

**© Tambe Ebai Norbert 2015
ALL RIGHTS RESERVED**

Acknowledgements

Humility is not about thinking less of yourself, rather, humility is thinking about yourself less.

There are many people that have earned my gratitude for their contribution to my time in graduate school.

I want to thank my supervisor Prof. Yuichi Kubota, who gave me countless failure-tolerant opportunities throughout my PhD. Before I knew him, the fear of failure always did paralyzed me, not anymore.

The universe is unbiased, she chooses to reveal herself to all who have the correct attitude.

Tambe E. Norbert

So I would claim you are profoundly misled by thinking about physics as similar to logic or number theory. Its not! its dynamical evolution, and most results of physics problems are not nice numbers like 1 or π or even e^π .

by Prof. Matt Strassler

Dedication

No, I have nothing against Mr. Einstein. He is a kind person and has done many good things, some of which will become part of the music. I will write to him and try to explain that the ether exists, and that its particles are what keep the Universe in harmony, and the life in eternity.

Nikola Tesla

The Universe is unbiased, she chooses to reveal herself to whomever she wants.

Tambe E. Norbert

Abstract

We performed a search for delayed photons produced during proton-proton collisions with center of mass energy, $\sqrt{S} = 8$ TeV. We use timing measurements made using the electromagnetic calorimeter to search for these delayed photons. In the absence of excess events over standard model prediction, we produce limits on the cross section, $\sigma_{\tilde{\chi}_1^0} > 0.02$ pb, for the production and decay of the lightest neutralino, $\tilde{\chi}_1^0$, with mass, $m_{\tilde{\chi}_1^0} \geq 235$ GeV/c^2 , and lifetime, $\tau_{\tilde{\chi}_1^0} \geq 35$ ns, as described in supersymmetry. We also show that using only timing information of the CMS electromagnetic calorimeter as observable, the CMS detector is sensitive to neutralino with lifetime up to 30 ns and mass, $m_{\tilde{\chi}_1^0} \approx 260$ GeV/c^2 . Description of how the electromagnetic calorimeter is used to make timing measurements and its performance is presented.

Contents

Acknowledgements	i
Dedication	ii
Abstract	iii
List of Tables	vii
List of Figures	ix
1 Introduction	1
2 Phenomenology of Long-Lived Particles	6
2.1 The Standard Model of Particle Physics	6
2.1.1 Main Components of the SM	7
2.1.2 Spontaneous Symmetry Breaking	13
2.1.3 Limitations of the Standard Model	16
2.2 Beyond Standard Model Physics	17
2.2.1 Supersymmetry	18
2.2.2 Minimal Supersymmetric Standard Model	19
2.3 Gauge Mediated Supersymmetry Breaking Models	23
2.3.1 Phenomenology	23
2.3.2 Long-Lived Particles in GMSB Models	25
2.4 Previous Search Experiments	31

3 Hadron Collider and Detector	33
3.1 Large Hadron Collider	33
3.1.1 Overview	33
3.1.2 Colliding Energy	34
3.1.3 Luminosity	35
3.1.4 LHC Bunch Structure	36
3.2 Compact Muon Solenoid	40
3.2.1 Overview	40
3.2.2 Calorimeter	42
3.2.3 Muon Chambers	47
3.2.4 Triggering	49
4 Time Reconstruction and Resolution	50
4.1 Electromagnetic Calorimeter Readout Electronics	50
4.2 Time Reconstruction	52
4.3 ECAL Time Performance from Test Beam	54
4.3.1 ECAL Time Resolution	54
4.4 ECAL Time Performance from Collision	56
4.4.1 Time Calibrations	57
4.4.2 Time Bias	62
4.4.3 ECAL Time Performance With Z Events	64
5 Event Reconstruction	68
5.1 Event Reconstruction Overview	68
5.2 Supercluster Reconstruction	68
5.3 Track and Vertex Reconstruction	70
5.4 Photon and Electron Reconstruction	71
5.5 Muon Reconstruction	74
5.6 Jet Reconstruction	76
5.7 Missing Transverse Energy Reconstruction	77
5.8 Anomalous Signals	78

6 Search Analysis for Long-Lived Particles	80
6.1 Analysis Strategy	80
6.1.1 Signal Modeling	82
6.1.2 Background Modeling	83
6.1.3 Datasets	83
6.1.4 ECAL Time	86
6.2 Event Selection	96
6.2.1 Trigger Selection	96
6.2.2 Offline Selection	98
6.3 Background Estimation	100
6.3.1 Collision Background	101
6.3.2 Non-Collision Background	102
6.3.3 Event Cleaning, Veto Performance and Fake Rates	109
6.3.4 Background Estimation with ABDC Method	111
6.3.5 Background Estimation Cross Check	114
6.4 Systematic Studies	120
6.5 Results	121
7 Statistical Analysis	123
7.1 Limit Computation	123
7.1.1 CLs Technique	124
7.1.2 Statistical Test Formalism	125
7.1.3 Test Statistics and p -values	127
8 Limit Interpretation	131
8.1 Signal Efficiency and Acceptance	131
9 Conclusion	136
Bibliography	137
Appendix A. Glossary and Acronyms	142
A.1 Glossary	142
A.2 Acronyms	142

List of Tables

2.1	SM particles and their gauge multiplets(representation) with quantum numbers. the numbers for example (3 , 2 , $\frac{1}{6}$) means (<i>triplet, doublet, Y = 1/6</i>) representations.	13
2.2	Supermultiplets and particle spin in SM and Supersymmetry.	19
2.3	Chiral supermultiplets and representation in Minimal Supersymmetric SM (MSSM). Super symmetric particles (sparticles) have a \sim on them. Spin -0 fields are complex scalars while spin-1/2 fields are left-handed two component Weyl fermions.	20
2.4	Gauge supermultiplets and representations in Minimal Supersymmetric SM (MSSM). Super symmetric particles (sparticles) have a \sim on them.	20
3.1	LHC operation parameter conditions during RUN 1, 2010-2013	39
3.2	CMS detector material, [22], and resolution(Time resolution: $N \approx 35$ ns, $\bar{C} \approx 0.070$ ns [39])	42
4.1	ECAL timing resolution absolute time and single precision for 2011 and 2012 of LHC Run 1	67
5.1	Simple cut-based selection criteria for electron and photon identification.	74
6.1	Data samples and the corresponding integrated luminosity totaling 19.1 fb^{-1} used in the our delayed photons search analysis	84
6.2	The signal GMSB SPS8 MC samples for difference Δ and Branching Ratios used in this analysis	85
6.3	The $\gamma +$ jets samples used in this analysis	85
6.4	The photon identification and selection criteria used in this analysis	99
6.5	The Jet ID and MET selection used in this analysis	99
6.6	Fake rates for different non-collision cleaning.	110

List of Figures

2.1	Higgs boson ‘‘Mexican hat’’ potential, $V(\phi^*\phi) = \mu^2(\phi^*\phi) + \lambda(\phi^*\phi)^2$, which leads to spontaneous symmetry breaking with choice of parameters $\mu^2 < 0$, $\lambda > 0$	15
2.2	SM particles and their interactions with vector bosons as mediators.	15
2.3	Higgs mass contributions from its coupling to fermions (a) and scalar (b) fields.	17
2.4	Supersymmetry particle mass spectra in the SPS8 or minimal GMSB (mGMSB) model.	22
2.5	Feynman diagrams of gravitino/golstino, \tilde{G} , gaugino and scalar interactions with superpartner pairs (ψ, ϕ) scalar (a) and (λ, A) gaugino (b) decay to gravitino.	24
2.6	Supersymmetry production cross-section against sparticle mass for different modes of supersymmetry production at a proton-proton collider. $pp \rightarrow \tilde{g}\tilde{g}$ processes have the dominant production cross section.	26
2.7	Feynmann diagrams for neutralino production from the cascade decay of a produced gluino (<i>top</i>) and squark (<i>bottom</i>). The final event has a single (<i>left diagrams</i>) or double photons (<i>right diagrams</i>) neutralino decay at LHC.	28
2.8	Neutralino lifetime and mass upper limit from ATLAS(left) and CMS(right) 7 TeV analysis with non-pointing photons and MET.	32
3.1	Schematic diagram showing the full Large hadron Collider.	34
3.2	Cumulative luminosity versus day delivered to (blue), and recorded by CMS (orange) during stable beams and for p-p collisions at 8 TeV center-of-mass energy in 2012.	36

3.3	Longitudinal Profile taken with Longitudinal Density Monitor (LDM) detector showing definition of Ghost/Satellite bunches with respect to main bunches.	37
3.4	(left)Arrival time distribution(red) of ATLAS MBTS for LHC fill 1533 during 2010 Pb-Pb run and LDM profile(black) for Beam2(same for Beam1). (Right) Timing of Clusters in the CMS endcap calorimeters for fill 1089:Left: EEP detector(left side of IP $z > 0$) Right: EEM detector(right side of IP, $z < 0$). Plots from ATLAS [30] and CMS, [31]	38
3.5	CMS Detector showing the different subdetectors and their material. . .	41
3.6	CMS detector schematic view with definition of $x - y - z$ coordinates. .	41
3.7	Schematic diagram of CMS calorimetry system with HCAL enclosing ECAL in the Barrel and Endcap regions.	43
3.8	Layout of the CMS electromagnetic calorimeter showing the arrangement of crystal modules, supermodules in the barrel with the preshower in front of endcap with supercrystals.	48
3.9	Cross section view showing the coverage range of CMS sub-detectors and their longitudinal distance from the IP.	48
4.1	Schematic diagram of the CMS ECAL electronics readout for a single channel(Left) and the entire Trigger Tower or Front End (FE) Card(Right).	52
4.2	(a) A measured ECAL pulse shape for a single channel. (b) $\mathbf{T} - \mathbf{T}_{\max}$ Vs $R(T)$ relationship whose inverse is $T(R)$. Solid line is pulse shape from test beam while dots are typical 10 discrete samples corresponding to signal from proton-proton collision.	53
4.3	Difference in the time measurements as a function of A_{eff}/σ_n of two crystals sharing an energy and belonging to the same electromagnetic shower obtained during electron testbeam measurements. The single crystal energy scales for barrel (EB) and endcap (EE) is overlaid. The fitted results give $N = (35.1 \pm 0.2)$ ns and $\bar{C} = (20 \pm 4)$ ns.	56

4.4	<i>Top 3:</i> Time calibration maps showing the distribution of mean time for each channel/PbWO ₄ crystal in EB (top) and EE (below: EE-(left), EE+(right)) before calibration. <i>Bottom 3:</i> Time calibration maps showing the distribution of mean time after calibration. After calibration most crystals have an average time of zero(GREEN).	60
4.5	Distribution of mean time (μ , <i>top row</i>) and time deviation (σ , <i>bottom row</i>) as a function of crystal energy for EB prior (left) and after (right) time bias corrections depending on energy have been applied.	63
4.6	Distribution of the time standard deviation (σ) against crystal geometrical position, η , in the ECAL barrel. Almost flat distribution of σ with η	64
4.7	Ecal time difference between the two reconstructed electrons in $Z \rightarrow e^-e^+$ decay. The electron time is the seed (crystal with highest energy deposit) time with additional correction due to the time of flight of the electron in EB and EE	65
4.8	Ecal absolute time of a single reconstructed electron in $Z \rightarrow e^-e^+$ decay. The electron time is the seed (crystal with highest energy deposit)time of the electron in EB and EE	66
4.9	Timing resolution from: <i>left:</i> Two most energetic crystals in the same readout unit, <i>right:</i> Two most energetic crystals belonging to different readout units, as a function of effective amplitude($A_{eff} = A_1 A_2 / \sqrt{A_1^2 + A_2^2}$) normalized to noise in EB. Both crystals are from reconstructed electrons in $Z \rightarrow e^-e^+$ events.	67
5.1	Superclustering algorithm direction in the (η, ϕ) plane in EB and fraction of electromagnetic shower energy coverage in a crystal energy matrix.	69
5.2	Z mass distribution from $Z \rightarrow e^+e^-$ decay showing improvement in the measurement of the Z mass after performing energy adjustments to account for intrinsic spread in crystal, photo-detector response and time-dependent corrections to compensate for channel response loss for EB (right) and EE (left)	72

5.3	Z mass reconstructed using electron superclusters shows improvement in Z mass measurement after applying energy adjustment at superclusters for EB (right) and EE (left).	73
5.4	Illustration of muons from proton-proton collision, cosmic rays and beam halo. (a) Muons from collision propagating from the center and moving outwards, (b) Cosmic muons traveling through the detector leaving signals in opposite hemispheres of the muon system, (c) Cosmic muons leaving signals in the tracker and opposite hemispheres, (d) cosmic muons entering and leaving the detector without passing through the muon detector layers, (e) beam halo muons penetrating the detector and leaving signals in the endcaps and (f) Cosmic muons entering the detector through the endcap and leaving through the barrel and which can happen in a <i>vice-versa</i> manner.	75
6.1	Number of photons(top left), E_T^{miss} (top right) and Number of jets(below) in neutralino decay to photon and gravitino events for different SPS8 model parameters.	86
6.2	Measuring the photon time using either seed time (black) or average time (blue). σ of the Gaussian fit from seed time slightly better average time which is computationally intensive.	88
6.3	Pulse shape profile(left) showing a spike (solid line) and a true EM shower (dashed line) from data. The χ^2 against ECAL time distribution(right) shows spikes misidentified as photons with very large χ^2 with earlier arrival time. The region of $\chi^2 > 4$ is mostly dominated by spikes events.	89
6.4	ECAL time distributions of in-time photons from MC $\gamma +$ jets (blue) and data (red) samples before (left) and after (right) we adjusted the photon time from MC.	90
6.5	Neutralino transverse momentum distribution(top left) and proper decay length(top right) with its decayed photon transverse momentum distribution(bottom left) and time of arrival at ECAL(Bottom right) for GMSB SPS8 model.	91

6.6	Schematic diagram showing $\tilde{\chi}_1^0 \rightarrow \gamma + \tilde{G}$ decay topology within the ECAL volume of the CMS detector (Left). Estimated photon arrival time at ECAL from the decay of neutralinos in the SPS8 model with $m_{\tilde{\chi}_1^0} = 256 \text{ GeV}/c^2$ and $c\tau = 6 \text{ m}$ (Right).	93
6.7	ECAL timing distribution of photons in barrel (EB), endcap (EE) and all of ECAL (ALL ECAL) with $p_T > 50 \text{ GeV}$ from data. A 2.5 ns delay timing structure is observed in endcaps.	94
6.8	Trigger efficiency turn-on curves for photon p_T and $E_T^{\text{miss}} > 25 \text{ GeV}$ (left) and for \cancel{E}_T with photon (right).The $\gamma + \text{jets}$ samples require photon $p_T > 170 \text{ GeV}/c$ for selecting events with true \cancel{E}_T	97
6.9	Photon with $p_T > 60 \text{ GeV}$ from data ECAL time distribution of events with different jet multiplicity and a single GMSB sample.	100
6.10	ECAL time against η (left) and ECAL time against ϕ (right) for photons with $p_T > 60 \text{ GeV}$ from data.	101
6.11	Schematic diagram showing production of photons from main pp and possible ghost/satellite bunch collisions in the CMS detector volume. Typical beam halo muon's entry direction into ECAL and GMSB neutralino decay is shown.	103
6.12	(Left) ECAL time $V.s \Delta\phi(\text{CSC Seg}, \gamma)$ for in time(black) and out-of-time(red and blue) photons. (Right)Photon ECAL time $V.s \eta$, expected halo photon time is shown as two red lines.	105
6.13	Using $\Delta\phi(\text{CSC Seg}, \gamma) < 0.05$ to tag photons with $\phi_\gamma = 0, \pm\pi$ in the endcaps. A good portion of endcap photon candidates are tagged.	106
6.14	Scatter plot showing $\Delta\eta(\text{DT Seg}, \gamma)$ against $\Delta\phi(\text{DT Seg}, \gamma)$ for out-of-time ($t_\gamma > 2 \text{ ns}$ and $t_\gamma < -3 \text{ ns}$) photons(Right) compared to in-time($ t_\gamma < 1 \text{ ns}$) photons(Left). Cosmic photon candidates occupy the small $\Delta\eta$ and $\Delta\phi$ region.	107
6.15	Scatter plot of $\Delta\eta(\text{DT Seg}, \gamma)$ against $\Delta\phi(\text{DT Seg}, \gamma)$ for photons from pure cosmic muon data. Small $\Delta\eta$ and $\Delta\phi$ are cosmic photons.	107

6.16	<i>Number of crystals</i> in photon supercluster plot (Left) for real photons candidates(black), spike photon candidates (magenta) and halo photon candidates (red). The spike photon candidates are selected with an energy swiss-cross variable ($1 - E_4/E_1$) (Right) shown comparing in-time photons ($ t_\gamma < 1.0$) to spike candidate sample.	109
6.17	Residual Background(red) after tagging the different non-collision background sources using the selection variables described in text.	111
6.18	ECAL time, t_γ Vs η_γ (top) and t_γ Vs ϕ (bottom) for photons from SinglePhoton dataset (left) compared to electron candidates from the DoubleElectron dataset (right). All photons or electron candidates are in barrel subdetector. Most of the photons with $\phi = 0, \pm\pi$ are halo photons which are not observed in the Z boson candidate sample.	116
6.19	Di-electron candidate mass distribution and the time of both electrons for the signal $76 < m_Z < 100$ GeV/ c^2 Z boson sample(left) and similar distributions from the Control ($50 < m_Z < 76$ GeV/ c^2 and $100 < m_Z < 130$ GeV/ c^2) sample (right). Candidates events from the DoubleElectron dataset.	117
6.20	<i>Top:</i> Control sample (left) and signal sample (right) of di-electron candidate mass distribution. <i>Bottom:</i> Figure showing definition of scale factor use in estimating the contributions from control sample in signal sample.	119
6.21	Timing distribution of genuine Z bosons after background contribution has been subtracted.	120
7.1	Sampling distributions for $f(t_\mu \mu)$ showing how one extracts the p -vlaues. left: is the using a analytic of the Asymptotic method and right: is from the HybridNew method.	128
7.2	Distribution of p -vlaues showing how upper limit on μ is extracted for a given threshold probability.	130
8.1	The reconstruction and selection efficiency (left) \times Acceptance ($t > 3$ ns) (right) against transverse decay length in laboratory frame for different $c\tau$ points.	132

8.2 Neutralino production cross section against proper delay length upper limit interpretation in SPS8 model. (Left) $\Lambda = 100$ TeV, (Right)(left) $\Lambda = 180$ TeV	133
8.3 Neutralino production cross section against neutralino mass upper limit at 95% confidence levels interpretation in SPS8 model.(Left) $C\tau = 11000$ mm, (Right) $C\tau = 6000$ mm	134
8.4 Neutralino two dimensional exclusion limit of neutralino mass (Λ) against proper delay length upper limit interpretation in SPS8 model in the decay $\tilde{\chi}_1^0 \rightarrow \gamma + \tilde{G}$ with limits from previous experiments shown.	135

Chapter 1

Introduction

Indirect observations of our universe, on very large distances or astronomical and cosmological length scales, indicate the presence of a new form of matter in the universe which only interacts significantly with visible matter through gravity [1]. This illusive matter in the universe, also known as *Dark Matter* (DM), does not emit or scatter off electromagnetic radiation. The supposed existence of this DM is one of the strongest indications for a new kind of physics beyond the standard model of particle physics, as no known particles of the standard model can be attributed to dark matter.

Visible matter, which does emit and can scatter off electromagnetic radiation, make up only 4.5% of the total matter in the universe and its properties like its particle content and their interactions, are best understood through simple symmetries of nature known as *gauge symmetries*. These gauge symmetries, expressed mathematically as gauge groups, are the building blocks in the formulation of a theoretical model known as the *Standard Model* (SM) which is used for understanding the contents and interaction properties of visible matter. The SM describes with unmatched precision, the possible types of interactions and their strengths, the fundamental particle contents and their properties which make up the entire visible matter. Despite this unprecedented success of the SM compared to most scientific models, the SM fails to describe DM which make up the largest portion of the matter in our universe.

There have been numerous experimental reports on the discovery of all the particles predicted by the SM. While, on the contrary, there have been no reports on the direct detection of particles which could make up dark matter. On the nature of DM, results

from theoretical models and numerical N-body simulations [2], support speculation that dark matter could be made up of particles which are neutral and stable i.e. particles which can remain stable enough for a long period of time comparable to the age of our universe, before they disintegrate. Such particles generally referred to as *dark matter candidate* particles could themselves be produced from the disintegration (decay) of not entirely stable or meta-stable particles with sufficiently long lifetimes on the length scale of a particle detector particles[3]. These meta-stable particles with sufficiently long lifetimes are called *Long-Lived* (LL) particles. LL particles can either be charged or neutral (i.e. in the context of the SM, carry no net charge). There is significant interest towards neutral DM particles, since DM does not interact with light. A good amount of effort is directed towards the search for dark matter particles produced from the decay of *neutral long-lived* particles[4]. Experimental techniques for detecting neutral particles are very limited and so previous methods for searching for DM particles are often being updated with few new methods entirely developed.

The search for dark matter particles covers a wide range of experiments, from deep space search experiments like the Hubble and James Webb Space Telescope experiments, the Alpha Magnetic Spectrometer detector on board the International Space Station of NASA, ground based particle detector experiments like the Super Cryogenic Dark Matter Search experiment which try to detect dark matter particles produced in cosmic rays, to collider experiments like the Large Hadron Collider (LHC) of the European National Laboratory for Nuclear Research in Geneva, Switzerland, where dark matter particles can be produced during particle collisions. The interest in collider experiments is base on theoretical model predictions that dark matter particles or particles which decay into dark matter particles can be produced in a collider like the LHC, provided there is sufficient center-of-mass energy. These models are extensions of the standard model to allow for the existence of new fundamental particles. The models are called *Beyond Standard Models* (BSM) and there are several of them. *Supersymmetry* is a BSM which extends the gauge symmetries to a much larger family of symmetries and allows for the doubling of the particles in the SM to include a wide variety of new fundamental particles which can be dark matter particles[3, 4]. A particular branch of supersymmetry models called Gauge Mediating Supersymmetry Breaking (GMSB) models, predict the production of new, massive, meta-stable, neutral, weakly interacting and long-lived

particles which can decay into a candidate dark matter particle and isolated energetic photons. The candidate dark matter particle is stable and also neutral and weakly interacting. It has a lifetime comparable to the age of the universe. Detecting photons from the decay of a supersymmetry neutral and weakly interacting long-lived particle will be an indication of new particles, as there are no neutral, weakly interacting and long-lived particles which decay into photons in the SM. Numerous previous experiments have searched for these photons. Often, the results from these experiments have been negative. Nevertheless, new experiments with new detection techniques and clever search methods depending on the manner of production and decay of these new particles are continuously being developed. We will refer to such new, massive, weakly interacting and neutral long-lived particles which decay into isolated photons and candidate dark matter particles as *Neutral Massive Long-Lived Particles* (NMLLP).

Our search analysis is motivated by the classic signature of a delayed photon from the decay of a NMLLP in GMSB models, produced in the LHC proton collider. The decay products of the NMLLP are detected using the multi-purpose Compact Muon Solenoid (CMS) particle detector. We consider the NMLLP to be the Next-To-Lightest Supersymmetric Particle (NLSP) called the *lightest neutralino* ($\tilde{\chi}_1^0$). This lightest neutralino decays into a photon and the Lightest Supersymmetric Particle (LSP) called the gravitino (\tilde{G}). The gravitino is neutral and weakly interacting with visible matter, and being the LSP makes it stable. These properties make the gravitino a good dark matter particle.. The neutralino decay can in general be instantaneous (prompt) or *delayed* depending on the choice of parameters in the neutralino decay model. In a subset of models called *R-Parity Conserving* (RPC) GMSB models, supersymmetry particles are pair produced either, directly during particle collisions, or from the cascade decay of higher massive supersymmetry particles produced also in particle collisions. As a result, in these models, the LSP is very stable and automatically a dark matter candidate particle while the NLSP (neutralino) is often long-lived and the photons are energetic, isolated and often delayed in their arrival time at a detector. These often delayed photons can be detected using the electromagnetic calorimeter (ECAL) of the CMS detector. The ECAL has an excellent timing resolution better than a *nanosecond* (ns). In cases where the neutralino is produced from the cascade decay of higher

massive particles, large transverse momentum (p_T) spray of hadronic particles collectively called jets are also part of the neutralino production and decay event. Since the gravitino is weakly interacting with the detector material, it is undetected. The gravitino presence is inferred using *missing transverse momentum* which in combination with the transverse momenta of the jets and photons should conserve the total momentum of the event in the transverse plane of the detector. In the decay scenario of the neutralino where its lifetime is large, say above, 3 ns, the photon is delayed and its measured arrival time is large (many nanoseconds (ns)). This is because of the inherently long neutralino lifetime and the extra distance it has to travel inside the detector before it decays. Finding an event, with the combination of jets, missing transverse momentum and at least a delayed photon is a clear signal for new particles not known in the standard model (SM). The CMS detector is located in the LHC tunnel at one of the proton bunch crossing points also known as *Interaction Point* (IP). We measure the arrival time of the photon from the IP to the surface of the ECAL. Relying on the excellent timing and energy resolution of the ECAL, we can distinguish between high energy photons from the decay of a NMLLP from those produced by the SM which are often prompt and not delayed. To ensure this excellent timing resolution, the ECAL detector is continuously time calibrated throughout the entire LHC proton-proton collision year. We will describe in future chapters how the ECAL timing alignment is done to realize this excellent timing resolution. Observation of a delayed photon event at the LHC using ECAL timing measurements, will confirm the existence of NMLLPs and will help answer important questions in particle physics like: What is the source and nature of dark matter?, Is there any reason why known SM particles are classified into 3 generations and have very different masses as known? Why do we observe so much matter compared to anti-matter in our universe? Is there a single universe or multiverses? Answers to these questions will provide a clear understanding and direction for future research in physics beyond the SM.

In this thesis, we have described our search for a NMLLP decaying to a photon using arrival time information of the photon to the ECAL and use this information to distinguish between the signal from new long-lived particles and background from SM interactions. Our search analysis uses data recorded using the CMS detector produced

from proton-proton (pp) collisions at the Large Hadron Collider (LHC) with a center-of-mass energy $\sqrt{S} = 8\text{ TeV}$. The contents of this thesis is arranged beginning with this introduction as chapter 1, followed by chapter 2, which gives a brief description of the SM, highlighting its strengths and weaknesses which motivates why we need to go beyond the SM in our efforts to understanding the universe. The study *supersymmetry* as our BSM physics model, paying particular attention to GMSB models which allows for the existence of NMILLP which can decay into a photon and a gravitino with jets in the associate event. In Chapter 3, we describe the LHC and CMS particle detector, dueling only on the sub-detectors which have been used in our search analysis. How timing measurements of a particle are made by the ECAL sub-detector is described in chapter 4. The reconstruction of a full event with its constituent particles is described in chapter 5 with the definition of quantities like jets and missing transverse energy (E_T^{miss}) according the CMS standards is described. Anomalous signals called *spikes* observed in the ECAL is mentioned. Our search strategy is described in chapter 6 with details of which datasets and triggers we have used, what is trigger efficiency, our choice of search observable, event selection and background estimation techniques used. We describe the various systematic sources considered and their contribution to our search result is presented in this chapter. Chapter 7 presents the statistical and analysis methods used with clear meaning of p -values as used in our analysis. The cross section times branching ratio limits depending on the lifetime and mass of the production and decay of a NMILLP using the minimal *Gauge Mediating Supersymmetric Model*, with *Snowmass Signal Point 8* (SPS8) as our benchmark model is presented in chapter 8. The interpretation of our results in terms of exclusion regions reached by our analysis is also presented in this chapter. Chapter 9 covers the conclusion.

Chapter 2

Phenomenology of Long-Lived Particles

2.1 The Standard Model of Particle Physics

The Standard Model (SM) of particle physics provides a thorough and experimentally verified mathematical model description of the fundamental constituents of visible matter and its interactions (except gravity) in the universe. Predictions of particle properties and interactions by the SM agree with most of the available experimental data with unmatched precision.

Despite the numerous success of the SM, there are some theoretical and experimental inconsistencies with the SM such as the observation of Dark Matter (DM) in the universe which is indescribable by the SM, the observation of neutrino oscillation and neutrino masses unexplained by the SM and the absence of gravitational interactions in the SM. These shortcomings of the SM, promotes the believe that the SM is part of a more general model. A candidate mathematical model beyond the SM which provides possible explanations for the above observations is *supersymmetry*.

In the next sections, we briefly describe the major components of the SM, its strengths and limitations and also introduce supersymmetry as a leading candidate for models beyond the SM.

2.1.1 Main Components of the SM

Mass, charge, spin and lifetime can be used to identify and categorize fundamental particles of nature. Particles with the same charge, mass and spin but opposite charge are called *Anti-particles* while particles with equal amounts for positive and negative charge are said to be neutral. A interesting classification of particles and anti-particles is using their *spin* (s). A particle's spin is an *internal quantum number* expressed as $n\hbar$, where n can be *integer* or *half-integer*. Half-integer spin ($\frac{1}{2}, \frac{3}{2}, \dots \times \hbar$) particles obey a *Fermi-Dirac* distribution or statistics and are called *fermions*. Integer spin particles ($0, 1, 2, \dots \times \hbar$) obey *Bose-Einstein* statistics and are called *Bosons*. No two identical fermions can occupy the same quantum state but any number of bosons can occupy a given quantum state.

Fermions are the fundamental building blocks of matter while bosons mediate interactions between fermions. No particle with spin, $s = 0\hbar$, had ever been experimentally observed until the 4th of July 2012 when the *Higgs* boson with spin, $s = 0\hbar$, was observed[7]. The Higgs boson is responsible for providing mass to both fermions and bosons. Its discovery completes the SM.

The particle spin set, S , shown in Equation 2.1.1, shows the spins of particles discovered and yet-to-be-discovered in the universe.

$$S = \left\{ s = \left(\dots 0, \frac{1}{2}, 1, \frac{3}{2}, 2 \dots \right) \cdot \hbar \right\}$$

Looking at the set S , our present and possibly future understanding of particles in the universe can be summarize as follows:

- $\mathbf{S = \frac{1}{2}\hbar}$ Particles which make up visible matter in the universe.
- $\mathbf{S = 1\hbar}$ Particles mediating gauge interactions.
- $\mathbf{S = 0\hbar}$ Particle responsible for giving mass to other particles.
- $\mathbf{S = 2\hbar}$ Yet-to-be-discovered particle mediating gravitational interactions.
- $\mathbf{S = \frac{3}{2}\hbar}$ Yet-to-be-discovered particle likely to make up **Dark Matter?**

It is interesting to note that the set particles with spins, $s = \{0, \frac{1}{2}, 1\} \hbar$, describes precisely only 4.6% of the entire matter in the universe through the SM. The SM is

a *relativistic quantum field theory* in which particles are represented as *quantum fields* and their dynamics and interaction with other particles is expressed using a mathematical functions called *Lagrangian density*, \mathcal{L} . The Lagrangian density is invariant under certain transformations or symmetries and carries the description of the dynamics of fermions, bosons and their interactions with the Higgs boson. Fermions and bosons obtain their mass by interacting with the Higgs boson through a process crucial to the SM called *Higgs Mechanism*. Our brief description of the SM, will be divided into the following sections:

- **Fermions:** All of visible matter is described using fermion fields.
- **Interactions:** Fermions interact either through electromagnetic, weak and strong interactions with vector bosons mediating the interactions. An interaction is the realization of some generic symmetry and associated with this symmetry is a conserved quantity.
- **Spontaneous Symmetry Breaking or Higgs Mechanism:** Fermions originally have no mass. They get their mass by interacting with the Higgs field through the *Higgs mechanism*. New states of matter or fermions can be formed through mixing with other states of matter or fermions.

Fermions

The *Dirac* equation given by Equation 2.1 is part of the SM Lagrangian describing

$$\mathcal{L}(\bar{\psi}, \psi, G^\mu) = \bar{\psi} (i\gamma^\mu \mathcal{D}_\mu - m) \psi. \quad (2.1)$$

fermion dynamics with its electromagnetic interaction through the \mathcal{D}_μ term. In the full SM Lagrangian, including the description of electromagnetic, weak and strong interactions, fermions participate in these interactions as pairs or *doublets* called a representation. According to the SM, fermions exists as either leptons (ℓ) or quarks (q) and come in 3 *generations*. The SM provides no explanation for the existence of only 3 generations. Leptons can participate in electromagnetic and weak interactions but not in strong interactions while quarks can participate in both interactions and strong interactions. Leptons have integer charge while quarks have fractional charge. The 3

generations of quarks and leptons also known as *flavors* are arranged in a mass hierarchy with the third generation being the heaviest. The second and third generations are meta stable can disintegrate or *decay* into the first generation through weak interactions. A lepton pair consists of a particular lepton flavor and its corresponding neutral neutrino type. There is a corresponding neutrino for each lepton generation. For example, an **electron** (e) and its corresponding electron **neutrino** (ν_e) make the first generation pair, (e, ν_e). Other lepton flavors include **muon** (μ) and **muon neutrino** (ν_μ) pair (μ, ν_μ) and **tau** (τ) and **tau neutrino** (ν_τ) pair (τ, ν_τ). In the SM, neutrinos are described as having no mass, however, numerous experiments have confirmed that neutrinos have a very tiny mass (order of electronvolts (eV)) and can oscillate from one generation into another over sufficiently large distances.

For quarks, a first generation pair of quarks consists of an “*up-type*” and a “*down-type*” quark. In addition to the electric charge, quarks also carry a *color* charge and as a result can equally participate in strong interactions. *Up-type* quarks like **up** (u), **charm** (c), **top** (t) have charge of $+\frac{2}{3}$ and *down-type* quarks such as **down** (d), **strange** (s), **bottom** (b) have a charge of $-\frac{1}{3}$. Charges are expressed in units of elementary charge e . The quark include (u, d) is the first generation and (c, s) and (t, b) are respectively, the second and third generations. Quarks do not exist as free particles in nature but are found bound forming composite particles like *pions* and *protons* collectively called *hadrons*. Hadrons consisting of a quark and antiquark (same mass and spin as a quark but different charge) bound together are called *mesons*, e.g. pions (π^0, π^\pm), while those with at least 3 quarks bound together are called *baryons*, e.g. protons. The distributions of these quarks inside hadrons can be modeled using *parton distribution functions* (PDF) which depends on the fraction of momentum of the given hadron carried by each quark.

One can distinguish between “Left” from the “Right” handed quarks and leptons from the nature of their interaction with electroweak bosons.

Since most particles in the second and third generation are meta-stable, and do decay into the first generation particles, it is possible to describe all visible matter in our universe using only one generation of leptons, **electron** and the **electron neutrino** (e, ν) and one generation of quarks, **up-quark** and **down quark** (u, d).

Interactions

Interaction between fermions is mediated by vector *bosons* with spin, $s = 1\hbar$. The SM describes the electromagnetic, weak and strong force and their force mediators. The *electromagnetic force* whose force carrier is a massless vector boson; the *photon* (γ), is described using the mathematical formulation called *Quantum Electrodynamics* (QED). It is responsible for the interaction of light with matter. The *weak force* has 3 massive vector bosons; W^\mp , Z^0 , as its force mediators and it is responsible for the decay of the second and third generation quarks into the first generation. The weak force was independently developed by Sidney Glashow, Abdus Salam and Steven Weinberg [8] in the 1960s unifying it with the electromagnetic force in a mathematical formulation called the *Electro-Weak Field Theory*. The 3 massive vector bosons were predicted in the late 1960s and were eventually discovered at CERN in 1983. Finally, the *strong force* described using the mathematical formulation of *Quantum Chromodynamics* (QCD) has a massless *gluons* (g) as its force mediators. The strong force like the weak force is a nuclear force, however, the same unification of the weak and electromagnetic forces is not observed with the strong force. It remains an open question whether at much higher energies, all 3 forces become unified behaving as a single force.

It is speculated that the gravity interaction not described by the SM, is mediated by a spin-2 particle called the *graviton* which is yet to be discovered.

The formulation of the SM, relies on the concept of *symmetry* and *conserved quantum numbers*. A symmetry is a transformation which leaves invariant the dynamics (Lagrangian density, \mathcal{L}) describing a particle interaction. Every particle interaction is associated with a symmetry and a conserved quantity. The conserved quantity is called *conserved quantum number*. Belonging to the SM, are *gauge symmetries*, meaning the SM Lagrangian remains invariant under space-time dependent gauge transformations. The gauge symmetry of the SM is a combination of 3 different gauge symmetries; $SU(3)_C$, $SU(2)_L$ and $U(1)_Y$, each describing a particular particle interaction type. This combination is expressed as given in equation 2.2.

$$SU(3)_C \otimes SU(2)_L \otimes U(1)_Y \quad (2.2)$$

$SU(3)_C$ is the gauge symmetry associated with strong interactions and the conserved quantum number is the *color* (C) charge allowing the gluon to interact with itself and with quarks. There are 8 (in the *octet* representation of the $SU(3)$ gauge symmetry) colorless and massless gluons and three different color type quarks for each quark flavor. Anti-quarks carry anti-color charges. Leptons, like electrons, do not carry the color charge and as a result cannot participate in strong interactions.

$SU(2)_L \otimes U(1)_Y$ is the gauge transformation group with conserved quantum number, *isospin* (T_3), necessary for the electroweak interaction. Corresponding to the $SU(2) \otimes U(1)$ gauge group, there are 4 massless gauge bosons, $W_\mu^{1,2,3}, B_\mu$, which combine to form the physical electroweak bosons of charged W^\mp and neutral Z^0 and γ . The W^\mp and Z^0 , through the spontaneous breaking of the electro-weak symmetry, obtain their masses. These physical mass states is responsible for quarks to be able to transform from one generation to the other. These bosons couple using the “charge” of the weak interaction called *isospin*, T_3 , and the *hypercharge*, Y , to matter fields. The W^\mp only interacts with **left-handed** fermions and **right-handed** anti-fermions. This leads to a phenomenon called *parity* violation. The electromagnetic charge, Q , is the result of a combination of the third component of the weak isospin, T_3 and the hyper charge, Y , through the following relation:

$$Q = T_3 + \frac{Y}{2} \quad (2.3)$$

Left handed fermions have $T_3 = \pm \frac{1}{2}$ and form representations known as isospin *doublets*, while, right-handed fermions have $T_3 = 0$ and form isospin *singlets* in the SM . The particles in the SM together in their representations given by the gauge symmetry as *multiplets*(*doublets*, *triplets*, etc) and the corresponding conserved quantum numbers is presented in Table 2.1. The $SU(2)_L \otimes U(1)_Y$ guage group is a combination of two symmetry groups with coupling strengths g and g' connected to the electric charge of each fermion as $e = g \sin \theta_w = g' \cos \theta_w$.

The angle, θ_w , is the *Weinberg angle*, $\sin^2 \theta_w \approx 0.231$ is not predicted by the SM but measured from experiments. Gauge bosons can rotate from their *weak* eigen states

to physically observed states using this angle.

$$W^\mp_\mu = \frac{W_\mu^1 \mp i W_\mu^2}{\sqrt{2}}, \quad \begin{pmatrix} A_\mu \\ Z_\mu \end{pmatrix} = \begin{pmatrix} \cos \theta_w & \sin \theta_w \\ -\sin \theta_w & \cos \theta_w \end{pmatrix} \begin{pmatrix} B_\mu \\ W_\mu^3 \end{pmatrix} \quad (2.4)$$

This angle, θ_w , also allows for the transformation of a quark from one flavor into another through the W^\mp bosons. In the lepton sector, according to formulation of the SM, such flavor transformation could in principle be possible but does not lead to any possible observable effects as neutrinos are considered to be massless in the SM. On the other hand, recent neutrino experiments have proven otherwise, as mixing between different neutrino types have been observed, indicating that neutrinos are not massless as thought but rather do have mass. The transformation of quarks into different flavors is a typical interaction happening inside the core of our sun in the decay of neutrons to protons and similarly in a nuclear reactor. The complete transformation of all quark flavors is described by the *Cabibbo-Kobayashi-Maskawa* (CKM) 3 by 3 matrix whose elements are parameters only measured from experiments and not predicted by the SM.

Particle and Their Gauge Symmetry Representation

Particle Name(Symbol)	Spin	Multiplet	$SU(3)_C \otimes SU(2)_L \otimes U(1)_Y$
Quarks (Q)	$1/2$	$(\mathbf{u}_L, \mathbf{d}_L)$	$(\mathbf{3}, \mathbf{2}, \frac{1}{6})$
$\bar{\mathbf{u}}$	$1/2$	\mathbf{u}_R^\dagger	$(\bar{\mathbf{3}}, \mathbf{1}, -\frac{2}{3})$
$\bar{\mathbf{d}}$	$1/2$	\mathbf{d}_R^\dagger	$(\bar{\mathbf{3}}, \mathbf{1}, \frac{1}{3})$
($\times 3$ families)			
Leptons(L)	$1/2$	(ν, \mathbf{e}_L)	$(\mathbf{1}, \mathbf{2}, -\frac{1}{2})$
$\bar{\mathbf{e}}$	$1/2$	\mathbf{e}_R^\dagger	$(\bar{\mathbf{1}}, \mathbf{1}, 1)$
($\times 3$ families)	$1/2$	ν_R^\dagger	$(\bar{\mathbf{1}}, \mathbf{1}, 1)$
Higgs (\mathbf{H}_u)	0	$(\tilde{\mathbf{H}}^+_u, \tilde{\mathbf{H}}^0_u)$	$(\mathbf{1}, \mathbf{2}, +\frac{1}{2})$
Higgs(\mathbf{H}_d)	0	$(\tilde{\mathbf{H}}^+_d, \tilde{\mathbf{H}}^-_d)$	$(\mathbf{1}, \mathbf{2}, -\frac{1}{2})$
Force Carriers			
Gluons	1	\mathbf{g}	$(\mathbf{8}, \mathbf{1}, 0)$
(Strong Force)			
W bosons	1	\mathbf{W}	$(\mathbf{1}, \mathbf{3}, 0)$
B boson	1	\mathbf{B}^0	$(\mathbf{1}, \mathbf{1}, 0)$
(Electro-Weak Force)			

Table 2.1: SM particles and their gauge multiplets(representation) with quantum numbers. the numbers for example $(\mathbf{3}, \mathbf{2}, \frac{1}{6})$ means (*triplet, doublet, $Y = 1/6$*) representations.

2.1.2 Spontaneous Symmetry Breaking

Spontaneous symmetry breaking is the spontaneous breaking of the gauge symmetry from a parent symmetry into an entirely, new sub-symmetry. In the SM, spontaneous symmetry is realized as represented by the expression in equation 2.5.

$$SU(3)_C \otimes SU(2)_L \otimes U(1)_Y \xrightarrow{SSB \text{ into}} SU(3)_C \otimes U(1)_{QED} \quad (2.5)$$

Early attempts prior to the 1960s to construct a gauge theory of weak interactions failed because the gauge bosons were massless while experimental evidence proved otherwise.

The Higgs (or Higgs-Brout-Englert) mechanism [10], is achieved by introducing a complex weak isospin *scalar doublet*, ϕ , i.e spin $s = 0\hbar$. During this process, the $SU(2)_L \otimes U(1)_Y$ symmetry is spontaneously broken into a $U(1)$ symmetry which describes electromagnetic interaction. Figure 2.1 shows a picture of the potential of the spin-0 complex Higgs field. The minimum value of the potential, $|\phi_0| = \sqrt{\frac{-\mu^2}{\lambda}} = \nu$, based on the choice of the parameters $\mu^2 < 0$ and $\lambda > 0$, is to spontaneously break the $SU(2)_L \otimes U(1)_Y$ symmetry into $U(1)$ symmetry. During spontaneous symmetry breaking, both matter and gauge bosons, except the photon γ), obtain masses. The process is referred to as *Higgs-Brout-Englert mechanism* or *Higgs mechanism*.

Quarks and leptons obtain their masses through their interaction with the Higgs field. A fermion's mass, m_f , is proportional to the strength of its interaction (Yukawa coupling λ_f) with the Higgs field. Electro-weak interaction mediating gauge bosons, Z^0 and W^\pm obtain their mass m_Z and m_{W^\pm} , respectively, by engulfing or “*eating*” the available massless components (*Nambu-Goldstone bosons*) of the complex Higgs doublet. From the four scalar fields(complex Higgs doublet), only a physically massive *Higgs boson* remains.

$$m_f = \lambda_f \frac{\nu}{\sqrt{2}}, \quad \frac{m_{W^\pm}}{m_Z} = \frac{\frac{1}{2}\nu g}{\frac{1}{2}\nu \sqrt{g^2 + g'^2}} = \cos \theta_w \quad (2.6)$$

The search for the Higgs boson was one of the purpose for building the large hadron collider at CERN. The discovery of the Higgs candidate scalar boson through its decay into two photons, $H \rightarrow \gamma\gamma$, and a pair of Z bosons, $H \rightarrow ZZ$, was presented to the public on July 04, 2012. Its measured mass was $m_H = 125 \pm 0.21 \text{ GeV}/c^2$.

It is important to note that there is no fundamental reason given by the SM why there should be only one type of the Higgs field to which all fermions couple to obtain their masses nor any prediction from the SM for the choice of parameters. There are other models such as supersymmetry, which allows for the possibility of more than one Higgs field. In Figure 2.2, we show a complete summary of particles and their interactions as described by the SM.

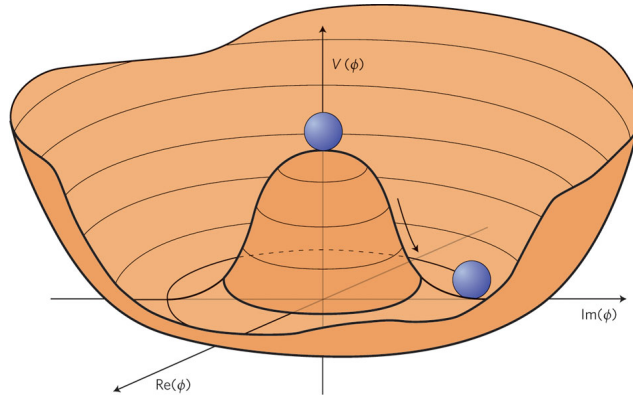


Figure 2.1: Higgs boson “Mexican hat” potential, $V(\phi^*\phi) = \mu^2(\phi^*\phi) + \lambda(\phi^*\phi)^2$, which leads to spontaneous symmetry breaking with choice of parameters $\mu^2 < 0$, $\lambda > 0$.

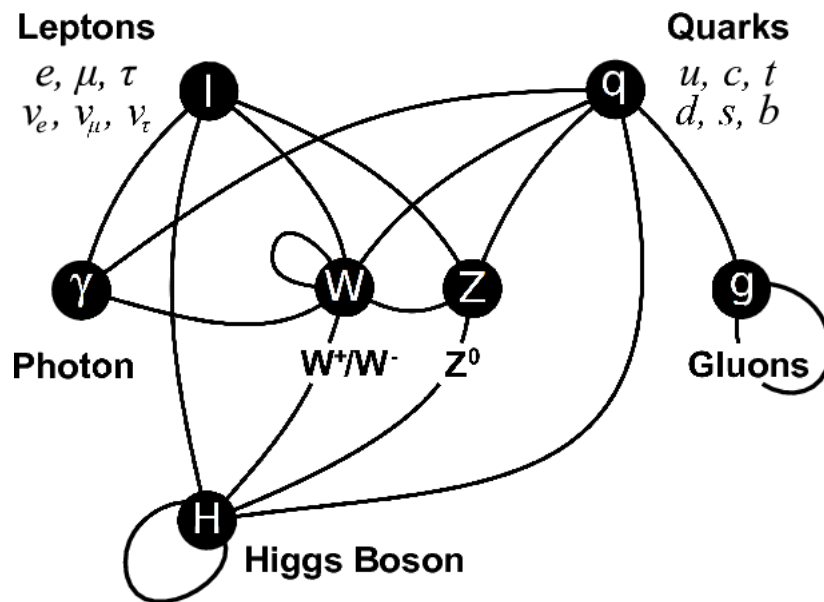


Figure 2.2: SM particles and their interactions with vector bosons as mediators.

2.1.3 Limitations of the Standard Model

Although numerous experiments support the SM in its description of particle properties with unmatched precision, there are many unanswered questions by the SM. We provide a summary below of those of our interest.

- **General Formalism**

Many important parameters like particle masses, Weinberg angle, the CKM matrix elements, for example, cannot not be derived from the SM. These are measured from experiments. Why only 3 generations of particles? Why the specific doublet representation of fields in the SM? These are questions to which the SM provides no answer.

- **Cosmological**

Why is there so much matter than anti-matter in the universe? *Cosmic Microwave Background* (CMB) and the *Wilkinson Microwave Anisotropy Probe* (WMAP) experimental results indicate the presence of excess matter which does not interact with light called *Dark Matter* (DM) and *Dark Energy* (DE). DE is responsible for the increase energy density causing rapid accelerating expansion of the universe. The nature of DM and DE and such observations cannot be explained using the current SM.

- **Theory**

SM description of nature does not include gravitational interactions. Observation of SM coupling constants varying with energy begs the question of whether at some higher energy scale, all the weak, strong and electromagnetic coupling constants behave as one i.e unified as a single coupling constant. If possible, at what energy scale does this force unification occur?

- **Mass Hierarchy or Naturalness**

Particle masses ranges from neutrino masses, a few eV to the top particle's mass of $173 \text{ GeV}/c^2$. The SM does not explain this mass hierarchy. To some physicist, the energy gap between the electro-weak symmetry breaking energy scale ($\approx 246 \text{ GeV}$) and the Planck energy scale (reduced Planck mass, $M_p = 10^{18} \text{ GeV}$) seems unnatural.

2.2 Beyond Standard Model Physics

The Higgs boson mass from SM predictions include additional corrections, δm^2 , to the higgs mass through its couplings with fermions such as the diagram shown in Figure 2.3(a). These additional corrections are given as shown in equation 2.7.

$$\delta m_f^2 = \frac{1}{16\pi^2} |\lambda_f|^2 \left(-2\Lambda^2 + 6m_f^2 \ln \left(\frac{\Lambda}{m_f} \right) + \dots \right) \quad (2.7)$$

Where λ_f is the Higgs to fermion coupling, $\lambda_f H \bar{f} f$ and Λ is an arbitrarily large energy scale (can be of order 10^{18} GeV) called the *cut-off* energy scale. As a result of this cut-off scale being very large, these corrections can also be very large. However, large corrections to the Higgs boson's mass are not observed in experimental measurements of the Higgs boson's mass which is 125 GeV/ c^2 . The SM provides no explanation for why these corrections are not observed.

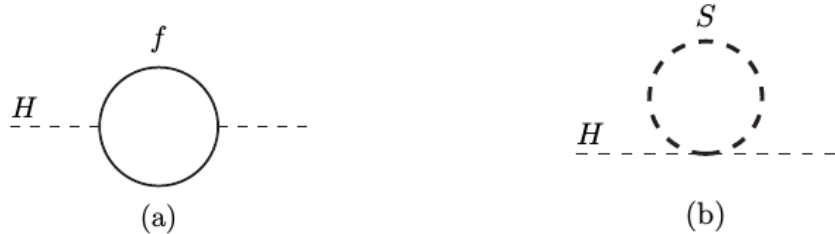


Figure 2.3: Higgs mass contributions from its coupling to fermions (a) and scalar (b) fields.

Models beyond the SM like *supersymmetry*, provide a plausible explanation as to why these corrections are not observed in experiments. The explanations is that, there are in addition to the higgs boson being the only scalar particle in the SM, new scalar particles, yet to be observed, which can also couple to the higgs field as shown in the diagram in figure 2.3(b). These scalar coupling contribution, given in equation 2.8 is of the opposite sign and as a result cancel the fermion contributions to the Higgs boson's mass. This is the explanation why the corrections to the Higg Boson's mass cannot be observed experimentally.

$$\delta m_S^2 = \frac{1}{16\pi^2} |\lambda_S|^2 \left(\Lambda^2 - 2m_S^2 \ln \left(\frac{\Lambda}{m_S} \right) + \dots \right) \quad (2.8)$$

This problem is known as the *Hierarchy problem* and is explained using supersymmetry. This cancellation is provided at all levels of the Higgs boson interaction and for whatever energy scale the cut-off value may be. Supersymmetry does not only provide an explanation to the Hierarchy problem, but also provide a good framework for the unification of fundamental forces. In addition, supersymmetry also predicts the existence of additional particles to the SM which are non interacting with ordinary matter and having very long lifetime making these particles exceptional candidates as dark matter particles. These properties motivates the study of supersymmetry as an interesting extension of the SM for understanding physics beyond the SM (BSM).

2.2.1 Supersymmetry

Supersymmetry is a relativistic Quantum Field Theory (QFT), relating space-time symmetries (rotation and translation) and gauge symmetries ($SU(3)_C \otimes SU(2)_L \otimes U(1)_Y$). During the early period, very little was understood about supersymmetry. Progress in understanding began with the *Haag-Lopuszanski-Sohnius* theorem [11] in 1975. This led to the introduction of supersymmetry generators called *Lie-superalgebra* generators, Q_i , $i = 1, \dots, N$, where N is the number of supersymmetry generators, which anti-commute with the group and space-time generators. The consequence is that fermions can be transformed into bosons and vice-versa. This boson-to-fermion and fermion-to-boson transformation is expressing using Equations 2.9.

$$Q|\text{Fermion}\rangle = |\text{Boson}\rangle, \quad Q|\text{Boson}\rangle = |\text{Fermion}\rangle \quad (2.9)$$

Thus, in supersymmetry, particles in a given state have the *same* mass but differ in their spin by half \hbar and in every irreducible representation of supersymmetry, like the chiral representation, there is an equal number of fermionic and bosonic degrees of freedom. Every particle has a supersymmetric partner with the same mass belonging to the same state representation or *supermultiplet*.

These supermultiplets are either *Chiral*, *Vector* or *Gravity* multiplets. The minimal supersymmetric extension of SM uses Chiral and Vector supermultiplets shown in Table 2.2.

Supermultiplets	Spin in SM,	Spin in Supersymmetry
<i>Chiral</i>	0	$\frac{1}{2}$
<i>Chiral</i>	$\frac{1}{2}$	0
<i>Vector</i>	1	$\frac{1}{2}$
<i>Gravity</i>	2	$\frac{3}{2}$

Table 2.2: Supermultiplets and particle spin in SM and Supersymmetry.

Models in supersymmetry are developed using *superfields*, Φ . A given superfield consists of ordinary scalar real or complex fields (ϕ), a Lorentz vector field (A_μ) and Left-handed or Right-Handed Weyl(2 degrees of freedom) spinor fields (ψ). *Chiral* and *Vector* superfields are used in constructing the minimal supersymmetric standard model. The simplest supersymmetric model is an extension of the SM to include supersymmetric particles with the same mass as their standard model partners. It is called the *Minimal Supersymmetric Standard Model* because it only involves the use of a single supersymmetry generator.

2.2.2 Minimal Supersymmetric Standard Model

In the Minimal Supersymmetric Standard Model (MSSM), the number of fundamental particles is increased. The full particle content in MSSM with this extension from SM is shown in Table 2.3 and 2.4.

The nomenclature of supersymmetric particles is derived from their SM counterparts by adding an “*s*” in front of the SM particles names. For example, a *selectron* is the supersymmetric partner of the electron, *squarks* are the supersymmetric partners of SM quarks. There are exceptions to this nomenclature which we will mentioned later. Both supersymmetry particles and their SM partners should have the equal masses, however, there have been no experimental evidence for such supersymmetric particles having the same mass as SM particles. Therefore, Supersymmetry is definitely not an exact symmetry in nature and must be spontaneously broken.

Particle Names	Symbol	spin 0	spin 1/2	$SU(3)_C \otimes SU(2)_L \otimes U(1)_Y$
squarks, quarks ($\times 3$ families)	Q	$(\tilde{u}_L, \tilde{d}_L)$	(u_L, d_L)	$(\mathbf{3}, \mathbf{2}, \frac{1}{6})$
	\bar{u}	\tilde{u}_R^*	u_R^\dagger	$(\bar{\mathbf{3}}, \mathbf{1}, -\frac{2}{3})$
	\bar{d}	\tilde{d}_R^*	d_R^\dagger	$(\bar{\mathbf{3}}, \mathbf{1}, \frac{1}{3})$
sleptons, leptons ($\times 3$ families)	L	$(\tilde{\nu}, \tilde{e}_L)$	(ν, e_L)	$(\mathbf{1}, \mathbf{2}, -\frac{1}{2})$
	\bar{e}	\tilde{e}_R^*	e_R^\dagger	$(\bar{\mathbf{1}}, \mathbf{1}, 1)$
higgsinos, Higgs	H_u	(H_u^+, H_u°)	$(\tilde{H}_u^+, \tilde{H}_u^\circ)$	$(\mathbf{1}, \mathbf{2}, +\frac{1}{2})$
	H_d	(H_d°, H_d^-)	$(\tilde{H}_d^\circ, \tilde{H}_d^-)$	$(\mathbf{1}, \mathbf{2}, -\frac{1}{2})$

Table 2.3: Chiral supermultiplets and representation in Minimal Supersymmetric SM (MSSM). Super symmetric particles (sparticles) have a \sim on them. Spin -0 fields are complex scalars while spin-1/2 fields are left-handed two component Weyl fermions.

Particle Names	spin 1/2	spin 1	$SU(3)_C \otimes SU(2)_L \otimes U(1)_Y$
gluino, gluon	\tilde{g}	g	$(\mathbf{8}, \mathbf{1}, 0)$
winos, W bosons	$\tilde{W}^\pm, \tilde{W}^\circ$	W^\pm, W°	$(\mathbf{1}, \mathbf{3}, 0)$
bino, B boson	\tilde{B}°	B°	$(\mathbf{1}, \mathbf{1}, 0)$

Table 2.4: Gauge supermultiplets and representations in Minimal Supersymmetric SM (MSSM). Super symmetric particles (sparticles) have a \sim on them.

Similar to the Higgs mechanism, supersymmetry breaking is also spontaneous and breaking supersymmetry can happen in many different ways. One of the ways in which supersymmetry is spontaneously broken is by gauge interactions. Supersymmetric models formulated using gauge interactions as the way to spontaneously break supersymmetry is called *Gauge Mediated Supersymmetry Breaking* (GMSB) models. GMSB models are interesting because they allow for only 5 fundamental parameters and still provide candidate dark matter particles. Supersymmetry breaking is realized in each model through a *superpotential* and the breaking defines the phenomenology and particle mass spectrum. In MSSM, particles interact with the Higgs bosons through a superpotential to

obtain their masses . This superpotential can be expressed as given in Equation 2.10.

$$W_{\text{mssm}} = \bar{u} \mathbf{y_u} Q H_u - \bar{d} \mathbf{y_d} Q H_d - \bar{e} \mathbf{y_e} L H_d - \mu H_d H_u \quad (2.10)$$

The objects H_u , H_d , Q , L , \bar{u} , \bar{d} , \bar{e} are chiral superfields of the chiral supermultiplets given in Table 2.3 above. The dimensionless couplings $\mathbf{y_u}, \mathbf{y_d}$, and $\mathbf{y_e}$ are 3×3 matrices of the Yukawa couplings. Rather than a single Higgs *doublet* which is assumed in the SM, supersymmetry breaking requires two Higgs doublets: H_u and H_d . The two Higgs give mass to **up-type** and **down-type** quarks, respectively, and to leptons, The superpartners of these Higgses are fermions and those of the gauge bosons called *gauginos* mix to produce new neutral and charged fermions called *Neutralinos* and *Charginos*, respectively. In order for GMSB models predictions of the proton lifetime to agree with experimental measurements of the proton lifetime being $> 10^{32}$ years, a matter symmetry relating the quarks to leptons through the *baryon* (B) and *lepton* numbers (L), a symmetry called *R-Parity* is introduced. R-parity is defined as, $R_P = (-1)^{3(B-L)+2S}$, where S is the particle's spin. SM particles like quarks have an *even* R-parity, $R_P = 1$, while supersymmetric particles like squarks have odd parity $R_P = -1$. The phenomenological consequence of R-parity is that, first, in the decay of supersymmetric particles, the lightest SUSY particle (LSP) have odd parity $R_P = -1$ and is considered to be absolutely stable. Second, every supersymmetric particle produced and is not the LSP, will eventually decay into the LSP or an odd number of LSPs. Third, supersymmetric particles can only be produced in pairs in a collider experiment. If, in addition to being stable, the LSP is neutral and interacts only very weakly with ordinary matter, then this makes it a good candidate for non-baryonic dark matter as required by cosmology, [3]-[5].

R-parity Conserving (RPC) models with the LSP stable are different from models without the conservation of R-parity. These R-parity non-conserving models are called *R-parity Violating* (RPV) models. In RPV models the LSP is unstable and decays to SM particles. A simplified version of GMSB models studied in this thesis is the *Snowmass Point and Slopes* (SPS8),[6], models whose phenomenological predictions are within the reach of the large hadron collider. It is possible to produce supersymmetric particles with mass of about a few TeV at the large hadron collider (LHC).

Figure 2.4 presents the mass spectrum for supersymmetric particle as predicted by the SPS8 model. The mass difference is determine by the supersymmetry breaking energy scale represented by Λ .

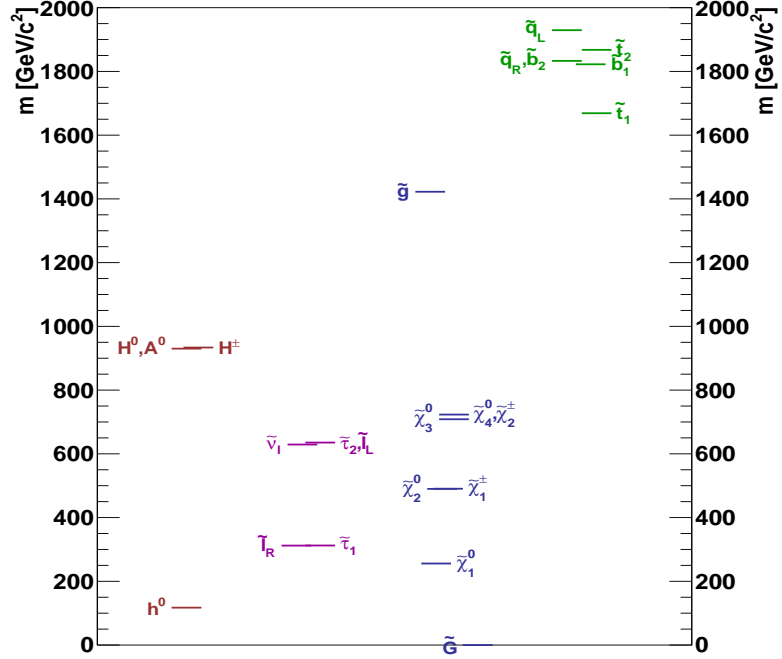


Figure 2.4: Supersymmetry particle mass spectra in the SPS8 or minimal GMSB (mGMSB) model.

In summary, MSSM predicts the existence of new particles whose spin (S) differ from their SM counterparts by half-integer. Bosons (fermions) in the SM have superpartners which are fermions (bosons). The superpartners of SM fermions are scalars called *sfermions* (\tilde{l}), sneutrinos ($\tilde{\nu}$) and squarks (\tilde{q}) while *gluinos* (\tilde{g}) are the superpartners of the massless gauge bosons of strong interaction, gluons. The scalar Higgs (2 needed) bosons and the vector gauge bosons of Electro-Weak interaction have fermionic superpartners called *higgsinos*, *Winos* and *Binos*. These can mix to form a pair of mass eigenstates called *charginos* ($\tilde{\chi}_j^\pm, j = 1, 2$), i.e., $\tilde{\chi}_{1,2}^\pm$ are mixtures of $\tilde{W}^+, \tilde{W}^-, \tilde{H}^+, \tilde{H}^-$ and a quartet of mass eigenstates called *neutralinos* ($\tilde{\chi}_i^0, i = 1, \dots, 4$), i.e., $\tilde{\chi}_{1-4}^0$ are mixtures of $\tilde{B}^\circ, \tilde{W}^\circ, \tilde{h}^\circ, \tilde{H}^\circ$.

2.3 Gauge Mediated Supersymmetry Breaking Models

GMSB models have 5 main parameters:

$$\{\Lambda, M_{\text{mess}}, N_5, \tan(\beta), sgn(\mu), C_{\text{grav}}\} \quad (2.11)$$

where Λ is the effective supersymmetry breaking scale, M_{mess} is the mass of the messenger particle involved in mediating supersymmetry breaking to the MSSM energy scale, N_5 is the number of messenger particles. The other parameters, $\tan \beta$ and $sgn(\mu)$ are related to the two Higgs bosons necessary for supersymmetry breaking with $\tan \beta$ being the ratio of the vacuum expectations values for both Higgs bosons. The sign of the Higgs potential is defined by $sgn(\mu)$. In these models, the gravitino can become very light with its mass bounded only by cosmological observations and as such is identified as the Least Stable supersymmetric particle (LSP). The mass of the gravitino is expressed in terms of the parameter C_{grav} according to equation 2.12.

$$m_{\tilde{G}} = C_{\text{grav}} \cdot \frac{\Lambda M_{\text{mess}}}{\sqrt{3} M_{pl}} \quad (2.12)$$

where $M_{Pl} = 1.3 \times 10^{19}$ GeV/c². C_{grav} is a scaling parameter, which determines the lifetime of the Next-to-Lightest-Supersymmetric Particle (NLSP) since the neutralino decay rate to the gravitino will depend on the mass difference between the neutralino and gravitino.

2.3.1 Phenomenology

Light gravitinos with unique gravitino-scalar-chiral fermion and gravitino-gaugino-gauge boson interactions shown in Figure 2.5 in GMSB models allow for the gravitino mass to be as low as a few eV and up to an upper bounded for them to provide the right amount of dark matter observed in the early universe. In addition to this, being neutral and stable makes them an excellent candidate particle for dark matter.

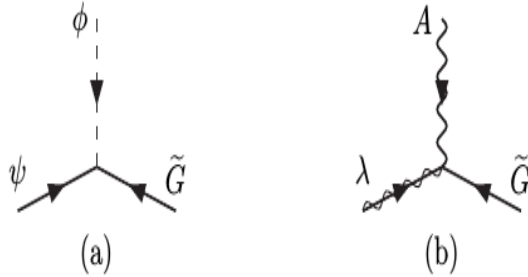


Figure 2.5: Feynman diagrams of gravitino/golstino, \tilde{G} , gaugino and scalar interactions with superpartner pairs (ψ, ϕ) scalar (a) and (λ, A) gaugino (b) decay to gravitino.

The decay of the NLSP to the gravitino is always accompanied by the SM partner of the NLSP, in order to conserve R-parity. If the particle, \tilde{p} , is the NLSP, its decay to gravitino and its SM particle, p , is given as $\tilde{p} \rightarrow p + \tilde{G}$. In the SPS8 benchmark model, the choice of parameters is as follows: $\mathbf{M}_{mess} = 2\Lambda$, $\tan(\beta) = 15$, $\mathbf{N}_5 = 1$. Only Λ and C_{grav} are allowed to vary, [6]. The gravitino (\tilde{G}), is the LSP. The NLSP, \tilde{p} , is the lightest neutralino ($\tilde{\chi}_1^0$). There are four types of neutralinos which are a mixture of the supersymmetric particles Bino (\tilde{B}°), Wino (\tilde{W}°), higgsino ($\tilde{H}_u^\circ, \tilde{H}_d^\circ$), depending on the choice of parameters Λ , $\tan \beta$, and $sgn(\mu)$. The particle p could be a photon (γ), Z boson (Z) (or Z') and a higgs boson (h). This thesis, for experimental convenience, will focus on the parameter space for which the particle p is a photon (γ) and $C_{grav} > 1$. This ensures that the lifetime of the NLSP is long enough but still its decay happens within the detector volume and the resulting photon is delayed or non-prompt on length scales of size of the detector. The decay rate for a NLSP to its SM partner and a gravitino can be approximated using only the mass of the NLSP and the effective supersymmetry breaking scale, $\mathbf{F} = C_{grav} \cdot \Lambda \cdot \mathbf{M}_{mess}$ giving in equation 2.13.

$$\Gamma(NLSP \rightarrow \gamma \tilde{G}) \approx \frac{m_{NLSP}^5}{\mathbf{F}^4} \quad (2.13)$$

This approximation is almost the same for the non-minimal GMSB models except that additional parameters are present showing explicit dependence of the neutralino life time on its states as a mixture of other supersymmetric particles.

2.3.2 Long-Lived Particles in GMSB Models

Measuring a particle's life time or distance traveled before it decays can be a useful method to uncover new fundamental interactions. As the lifetime is related to the decay rate which is determined by the particles interactions and available energy space.

Production of supersymmetric particles at Hadron Colliders

The production of a particle in a particle collider is a probabilistic process. This probability is expressed as a measurable quantity called *cross section*. For example, the cross section of producing a particle in proton-proton collider such as the LHC, is the probability that the proton beams will collide and interact in a certain way to produce that particle. Although this cross section (σ) is measured in units of area as *barns* ($1b = 10^{-24} \text{ cm}^2$), usually it has very little relation to the physical interpretation of area as used in everyday life. It is rather a technical term for counting the number of the particle produced when these proton beams collide. The cross section of producing the particle depends on the available energy of the proton beams compared to the mass of the particle, the type of interaction during collision which in turn depends on the coupling constants, and the flux of the proton beams. The rate or number per unit time of the particle produced at a specific particle collider is given as a product of its cross section times the instantaneous luminosity (\mathcal{L}). The instantaneous luminosity is the number of incident particles per unit area per unit time. The typical cross section of producing a supersymmetry particle at the LHC is of the order of $1 \text{ pb} = 10^{-12} \times 10^{-24} \text{ cm}^2$ or at times $1 \text{ fb} = 10^{-15} \times 10^{-24} \text{ cm}^2$ for extremely rare SUSY processes. While that for a standard model process like the production of the Z or W^\pm bosons is of the order of a few $nb = 10^{-9} \times 10^{-24} \text{ cm}^2$. This means there are more SM processes than supersymmetry process and so the search for supersymmetric particles in the LHC is very challenging.

The rate of production of a supersymmetric particle at the LHC depends on the mass of supersymmetric particle. The masses of supersymmetric particles are much higher than those of SM particles and as a result, the cross section for producing supersymmetry particles at a hadron collider is much smaller compared to that for SM particles. The cross section of a given supersymmetric process happening at the particle collider

can be computed and compared with experimental measurements. Using diagrammatic representations called *Feynmann* diagrams of the process happening, the cross section is derived from the Feynmann diagrams as the computed probability of the process. Supersymmetry processes which leads to the production and decay of neutralino ($\tilde{\chi}_1^0$) at the LHC can involve electro-weak and strong interactions. The production of supersymmetry particles in strong interactions have larger cross sections compared to electro-weak processes because of the strong coupling in strong interaction processes. Many interaction processes in the LHC are strong interactions as the LHC is a proton-proton collider. We show in Figure 2.6 a diagram showing the variation of the supersymmetry production cross section against the mass of the supersymmetric particle. From this figure, it is clear that the production of supersymmetric particle at the LHC through strong interactions like $pp \rightarrow \tilde{g}\tilde{g}$, $\tilde{q}\tilde{q}$ is higher than through electro-weak interactions like $pp \rightarrow \tilde{\chi}^\pm\tilde{\chi}^\mp$, $\tilde{\chi}^0\tilde{\chi}^\pm$.

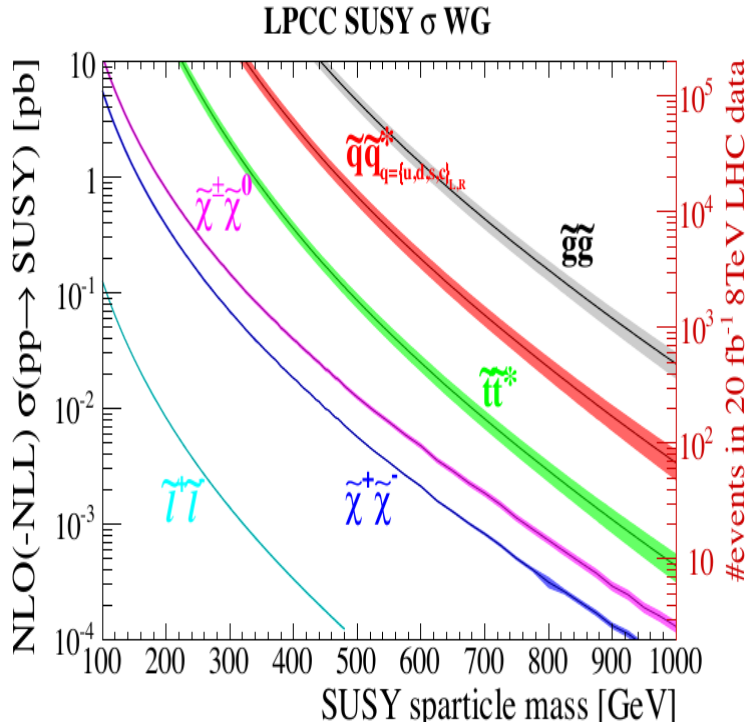


Figure 2.6: Supersymmetry production cross-section against sparticle mass for different modes of supersymmetry production at a proton-proton collider. $pp \rightarrow \tilde{g}\tilde{g}$, $\tilde{q}\tilde{q}$ processes have the dominant production cross section.

We will concentrate on the production of neutralinos from processes like $pp \rightarrow \tilde{g}\tilde{g}$, $\tilde{q}\tilde{q}$, as these processes have a higher production cross section at the LHC. We mentioned earlier that a probable manner in which neutralinos can be produced is from the production and subsequent decay of higher massive supersymmetric particles. Some of these higher massive supersymmetric particles include squarks (\tilde{q}), excited squarks (\tilde{q}^*) and gluinos (\tilde{g}). In this scenario, the neutralino is produced *indirectly* or as we say from the *cascade decay* of higher massive supersymmetric particles. The Feynmann diagram for these production processes, $pp \rightarrow \tilde{g}\tilde{g}$, $\tilde{q}\tilde{q}^*$, are given in figure 2.7. Squarks and gluinos do not directly decay into gravitinos but through neutralinos and eventually to gravitinos because their coupling to the gravitinos is not possible. The reason for this is that, in GMSB models, there are no gravitino-gluino-gauge boson or gravitino-squark-gauge boson couplings but rather gravitino-gaugino-gauge boson or gravitino-scalar-chiral fermion couplings.

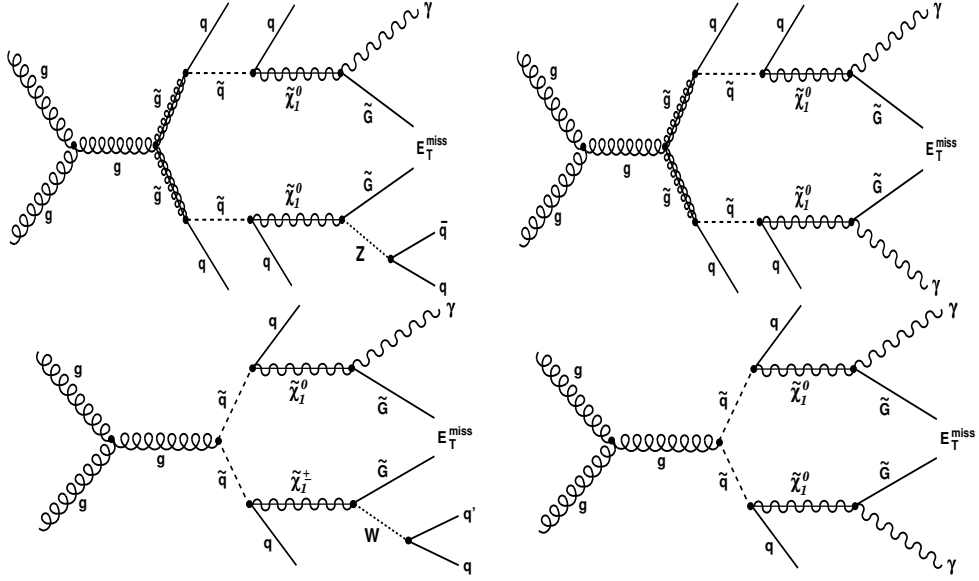


Figure 2.7: Feynmann diagrams for neutralino production from the cascade decay of a produced gluino (*top*) and squark (*bottom*). The final event has a single (*left diagrams*) or double photons (*right diagrams*) neutralino decay at LHC.

Particle Decay Rate

When a particle is produced, say particle **A**, its coupling to other particles, say particles **B₁** … **B_n**, where n is total number of particles particle, allows for it to decay into these other particles. In addition to the coupling, if the mass of particle **A** is greater than the total sum of mass of particles **B₁** … **B_n**, i.e $m_{\mathbf{A}} > m_{\mathbf{B}_1} + \dots + m_{\mathbf{B}_n}$, then we say, particle **A** *decays* to particles **B₁** … **B_n**. Particle for which no such channel for decay is possible are termed *stable*. Our current understanding is that only the electron (e) and the proton (p) are stable(although there are theories which predict the proton to decay after 10^{34} years and also theories where stable heavy or light particles will explain the nature of Dark Matter. This time through which a particle lived before it decays is called its *lifetime*. Particle decays in which the particle decays instantly as soon as they are produced are called *prompt* decays while particle decays with observable lifetime are *non-prompt* decays. Non-prompt decays might range from factors of a seconds i.e. *nanoseconds* ($1 \text{ ns} = 10^{-9} \text{ s}$) to minutes. In particle decay, strong *couplings* and large *mass difference* between the parent and the daughter particle(s) leads to faster

the decay. The process of obtaining the decay rate during experiments is expressed mathematically as; $N(t) = N(0)e^{-t/\tau}$, where both $N(t)$ and $N(0)$ are the number of the particles present at time t and at the beginning, $t = 0$. τ is the particle's *lifetime*. The rate at which a particle decays is its *decay width* (Γ). The decay width relies on the availability of daughter particle(s) the parent particle can couple to and the mass(es) of the daughter particle(s) must be less than the mass of the parent particle. Thus, a given particle, **A** will preferentially decay to particles **C₁** … **C_n** with which it has stronger couplings and its mass is much larger than their masses. This preferential decay into a specific set of particles or channel brings about terms like *Branching Ratio* (BR). The BR is related to the total decay width through $BR = \Gamma/\Gamma_{\text{Total}}$, where, Γ_{Total} is the particle's total decay width and Γ is its decay width to a preferential channel. The decay width is related to lifetime, τ , as the inverse of the lifetime. This relationship is expressed as given in Equation 2.14.

$$\tau = \frac{\hbar}{\Gamma} \quad (2.14)$$

τ is the particle's lifetime in a frame where the particle is not moving. It is convenient to express lifetime in units of lengths rather than time. The lifetime in units of lengths e.g. meters (m), is $c\tau$, where c is the speed of light in vacuum. $c\tau$ is also called the *proper decay length* just as the lifetime, τ , is also called the *proper lifetime*. Since most particles have mass and travel with velocity \vec{v} not equal to c , this distance travel considering $|\vec{v}| \neq c$ is fully expressed using equation 2.15.

$$\vec{L} = \vec{\beta}\gamma c\tau \quad (2.15)$$

where $\vec{\beta} = \frac{\vec{v}}{c}$, \vec{v} is the particle's traveling velocity and $\gamma = \frac{1}{\sqrt{1-\frac{v^2}{c^2}}}$ is a factor relating the motion when it is not moving (rest frame) to a frame where it is moving. Equation 2.15 can also be expressed in as $\vec{L} = \frac{\vec{p}}{m}c\tau$, in terms of the particle's momentum p and mass, m . A particle with a large mass, m , produced with a small momentum, will travel slow covering some distance before it decays. Since decay rate, Γ , depends on the coupling, particle decaying through electromagnetic, weak and strong interactions have very different decay rates. Particles decaying through strong interactions have

the largest decay rate and equally shortest lifetime of about 10^{-17} to 10^{-25} seconds. Electromagnetic particle decays have lifetime which can vary from 10^{-12} seconds to about 10^{-9} seconds and weak interactions have lifetimes that can vary from *nanoseconds* to several minutes. Particle lifetime may also vary from a few femtoseconds ($1 \text{ fs} = 10^{-15} \text{ s}$) to the age of the universe or equivalently its measured distance traveled can vary from a few μm to billions of km [12, 13]. The term *long-lived* particles refers to particles which live long enough to travel a distance comparable to the detector size. This distance traveled might range from a few μm to meters.

Neutralino as Long-Lived Neutral Particle

The neutralino being the next-to-lightest-supersymmetry particle (NLSP), can decay into a photon (γ), Higgsino (\tilde{H}^0), Z boson and gravitino (\tilde{G}) [14, 15]. The probability for a neutralino ($\tilde{\chi}_1^0$), produced with energy $E_{\tilde{\chi}_1^0}$ and mass $m_{\tilde{\chi}_1^0}$ to travel a distance x before decaying to a photon and gravitino in the laboratory frame can be expressed as $\mathcal{P}(x) = 1 - \exp\left(-\frac{x}{L}\right)$, where the distance traveled in a particle detector by the neutralino is given by Equation 2.16.

$$L = \left(c\tau_{\tilde{\chi}_1^0} \right) \cdot (\beta\gamma)_{\tilde{\chi}_1^0} \quad (2.16)$$

From Equation 2.16, it is clear that this distance depends on two main factors. The boost factor, $(\beta\gamma)_{\tilde{\chi}_1^0} = \frac{|\vec{p}_{\tilde{\chi}_1^0}|}{m_{\tilde{\chi}_1^0}} = \sqrt{\left(\frac{E_{\tilde{\chi}_1^0}}{m_{\tilde{\chi}_1^0}}\right)^2 - 1}$, which indicates how fast the neutralino is traveling before it decays. For slow moving neutralino, $(\beta\gamma)_{\tilde{\chi}_1^0} \ll 1$.

This means that the momentum ($p_{\tilde{\chi}_1^0}$) of the neutralino during production from gluino or squarks decays must be much smaller than the its mass, $m_{\tilde{\chi}_1^0}$. Neutralinos, produced, with their mass and momentum satisfying the slow condition, $p_{\tilde{\chi}_1^0}/m_{\tilde{\chi}_1^0} \ll 1$, are definitely good candidates for detectable long-lived neutralinos. The other factor is the inherent long lifetime, $c\tau_{\tilde{\chi}_1^0}$, of the neutralino. Neutralinos with $c\tau_{\tilde{\chi}_1^0} > 1$ are long-lived and would make good candidates for detectable long-lived neutralinos. This inherent neutralino lifetime can be expressed as given in equation 2.17.

$$c\tau_{\tilde{\chi}_1^0} \approx \left(\frac{m_{\tilde{\chi}_1^0}}{\text{GeV}} \right)^{-5} \left(\frac{\sqrt{F}}{\text{TeV}} \right)^4 \quad (2.17)$$

$$c\tau_{\tilde{\chi}_1^0} \approx C_{grav}^2 \left(\frac{m_{\tilde{\chi}_1^0}}{\text{GeV}} \right)^{-5} \left(\frac{\sqrt{\Lambda \cdot M_{\text{mess}}}}{\text{TeV}} \right)^4 \quad (2.18)$$

It is important to note that by changing the supersymmetry breaking scale, \mathbf{F} , the lifetime of the neutralino also changes. In the SPS8 model, the parameter C_{grav} is used to adjust the inherent lifetime of the neutralino. Thus, we re-write the neutralino lifetime as given in equation 2.18. This equation is used to simulate physics events with the production and decay of neutralino in CMS detector using Monte Carlo (MC) simulations. The supersymmetry breaking scale, Λ , determines the mass of gluino (\tilde{g}), squarks (\tilde{q}) which decay to the neutralino. Therefore the neutralino momentum, $p_{\tilde{\chi}_1^0}$ is determined by the masses of gluino and squarks. If the gluino or squark decays to the neutralino in association with a many gluons and quarks seen in the detector as *jets*, then the neutralino momentum is small with the ratio $p_{\tilde{\chi}_1^0}/m_{\tilde{\chi}_1^0} \ll 1$, this means the neutralino is slow and therefore long-lived. However, if the gluino or squark is decays with less number of jets, then the neutralino momentum is not so small and the neutralino is not very long-lived. It is worth noting that kinematic properties of the neutralino like momentum, arrival time at the CMS ECAL and the number of associated jets can be influenced by the gluino or squark decay properties. The gluino or squark is produced during proton-proton (pp) collisions at the LHC and the data recorded by the CMS detector is analyzed to search for events with neutralino decay.

2.4 Previous Search Experiments

The have been previously other search experiments for neutral long-live particles decaying to photons. Obviously, negative findings from these experiments led to possible search exclusion regions in terms of the lifetime, mass and cross section of the existence of supersymmetry particles in different supersymmetry models. Results from experiments(DO, CDF, CMS and ATLAS) [16, 17, 18, 19, 20] of the search for Neutralino NLSP decaying to photon and gravitino interpreted using the SPS8 benchmark model is shown in 2.8. These results show that within the SPS8 model, neutralinos with mass $m_{\tilde{\chi}_1^0} \leq 245$ GeV and proper decay length $c\tau_{\tilde{\chi}_1^0} \leq 6000$ mm have not been found at hadron colliders. The diagram on the left of figure 2.8 are exclusion results in the neutralino mass or supersymmetry breaking scale Λ on the horizontal axis and

the neutralino lifetime, $c\tau_{\tilde{\chi}_1^0}$ on the vertical axis from the 7 TeV search analysis by the ATLAS experiment while the diagram on the right is that for CMS experiment. The colored regions on the plots shows the parameter space where these searches have been performed and the findings were negative.

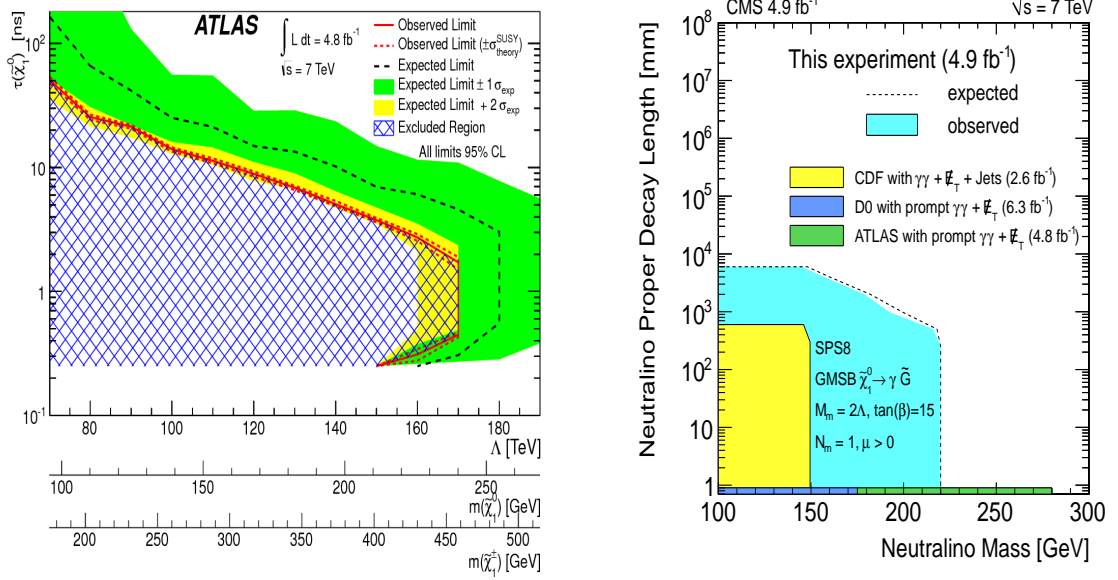


Figure 2.8: Neutralino lifetime and mass upper limit from ATLAS(left) and CMS(right) 7 TeV analysis with non-pointing photons and MET.

Chapter 3

Hadron Collider and Detector

This section describes the particle collider and detector. The first section describes the particle accelerator which is the Large Hadron Collider (LHC) and the next section describes the Compact Muon Solenoid (CMS) detector with emphasis to those sections directly relevant to this analysis. A detailed description of the LHC and CMS detector is found in [21] and [22].

3.1 Large Hadron Collider

3.1.1 Overview

The LHC is a proton-proton and heavy ion collider designed to achieve a center of mass \sqrt{S} energy of 14 TeV. It is hosted by the European Organisation for Nuclear Research (CERN). Unlike linear colliders, the LHC is a circular collider with nearly 27 km in circumference located at the border between France and Switzerland. It is designed to smash protons and ions against each other controlled by powerful magnets at four main points. The Compact Muon Solenoid (CMS) is one of the multi-purpose particle detectors at each collision point. Fig. 3.1 shows the LHC and the different stages before particle collision.

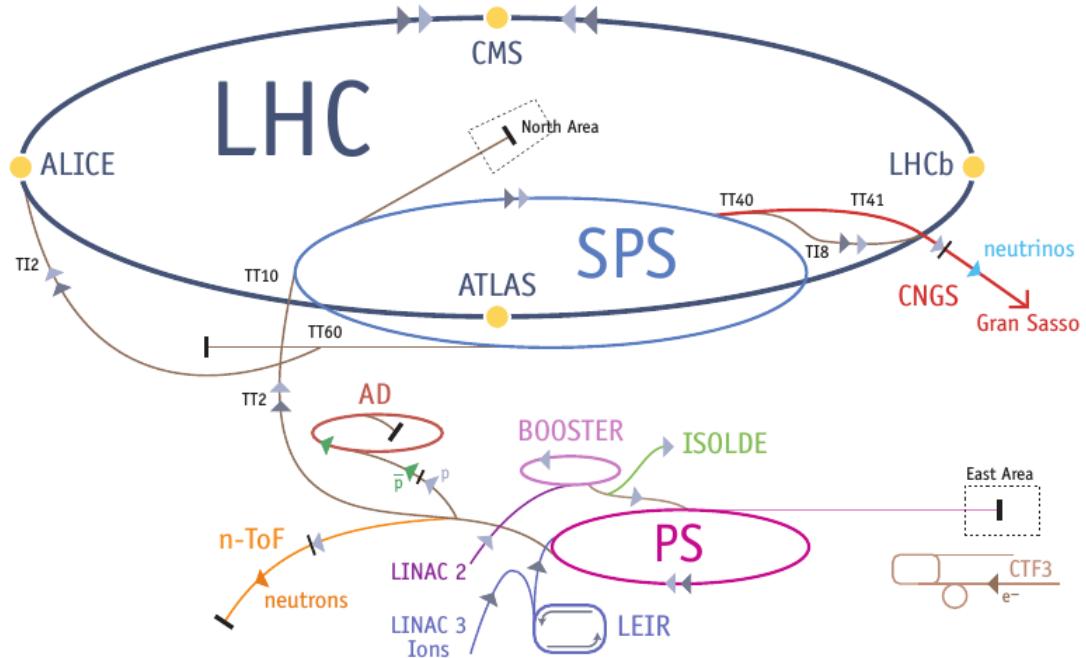


Figure 3.1: Schematic diagram showing the full Large hadron Collider.

3.1.2 Colliding Energy

Hydrogen ions also known as protons from hydrogen gas where the orbiting electron has been stripped away is inserted into a linear accelerator called *Linac 2*. Using electromagnetic fields in Radio Frequency (RF) cavities, these protons are accelerated to an energy of 50 MeV creating a stream of particles called *particle beams* arranged in packets known as *bunches*. Protons from the Linac2 are injected into the circular synchrotron Booster (PSB). The circular synchrotron accelerator ensures that the protons pass many times through a cavity with their energy slowly increasing each time to reach the design energy. The PSB accelerates the protons up to 1.4 GeV and inject them into the Proton Synchrotron (PS) which increases their energy to 25 GeV. These protons traveling at 99.93% the speed of light are sent to the Super Proton Synchrotron (SPS) and accelerated to an energy of 450 GeV. They are finally transferred into the LHC ring (accelerating in a clockwise and anti-clockwise direction) and accelerated for about 20 minutes to their nominal energy of 7 TeV. By now the protons are traveling with the

speed of 99.9999% the speed of light. Powerful bending magnets are used to keep the beams traveling in the circular LHC ring. The advantage of circular particle colliders over fix target is that, the energy available to make new particles called the *center of mass* (COM) energy, denoted as \sqrt{S} is simply the sum of the energy of the two beams i.e. $\sqrt{S} = E_{\text{beam1}} + E_{\text{beam2}}$ compared to $\sqrt{E_{\text{beam}}}$ for fix target experiments. For the LHC, each beam is designed to have energy of 7 TeV making $\sqrt{S} = 14$ TeV. In circular colliders, synchrotron radiation (is inversely proportional to the mass of the charge particle to the fourth power) by an accelerating charge particle contributing to loss its energy. This would require a continuous addition of energy after each turn to maintain the beam energy to a stable value. However, since the proton's mass is about 0.938 GeV, and are to be accelerated to about 7 TeV, this loss of energy is not very significant unlike for electrons whose mass is about 0.000511 GeV and the energy loss is more. Thus protons are preferred to electrons for a circular collider. Then again, the debris of particles produced when electrons collide is much less compared to that of protons making analysis in a hadron collider very challenging.

3.1.3 Luminosity

In colliding beams experiments, the center of mass energy available for the production of new effects is very important. However, the number of useful interactions producing effects (events) is equally important, especially in cases where the probability (also known as cross section, σ) of producing rare events is very small. The quantity which measures the ability of a particle accelerator to produce the events from the required number of interactions is called *luminosity*. The luminosity is also the proportionality factor between the number of events per second and the cross section. Luminosity (\mathcal{L}) is therefore a measure of the number of collisions that can be produced in a collider per squared area per second. The cross section is calculated from theory while the luminosity depends on factors ranging from the flux i.e. number of particles per second of the beams, the beam sizes at collision, and the frequency of collision. For physics experiments, the integrated luminosity which is total luminosity over a given period of time usually a year gives the amount of data that has been recorded by a given detector.

Using the luminosity (\mathcal{L}) and the cross section (σ_p) of a given process, we can calculate event rate (\mathcal{R}) or the number of events per second produced in proton collisions

by the given interaction process. By calculating the event rate, we are measuring a given cross section (σ_p) through $(\sigma_p = \frac{\mathcal{R}}{\mathcal{L}}$ in order to prove or disprove theories which make prediction on σ_p .

$$\mathcal{R} = \mathcal{L} \cdot \sigma_p \quad (3.1)$$

In CMS we have a “recorded” and “delivered” luminosity. Delivered luminosity refers to the luminosity delivered by LHC to CMS and one would expect this to be equal to the amount recorded. However, there are instances where the CMS detector is unable to take data either because the data acquisition chain (DAC) or one of the CMS sub-detectors is temporarily down and also trigger dead time. Figure 3.2 shows the total integrated luminosity delivered by LHC and recorded using the CMS detector during the 8 TeV proton-proton collision by the LHC.

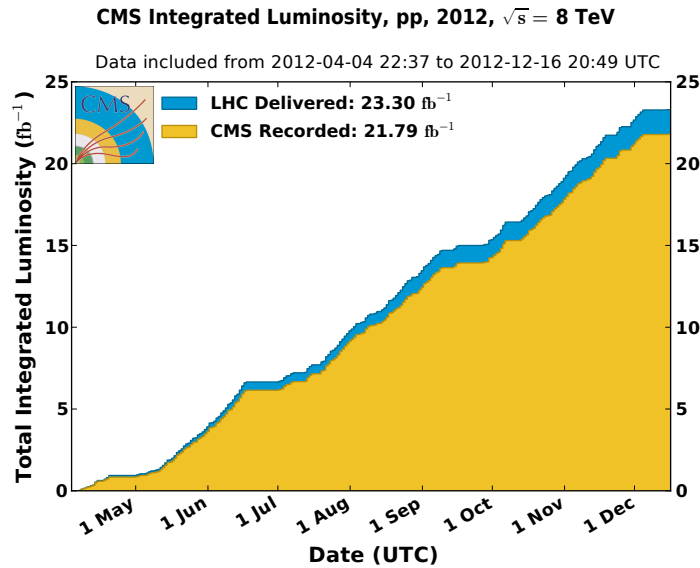


Figure 3.2: Cumulative luminosity versus day delivered to (blue), and recorded by CMS (orange) during stable beams and for p-p collisions at 8 TeV center-of-mass energy in 2012.

3.1.4 LHC Bunch Structure

Each LHC proton bunch is placed inside an RF buckets during beam filling. The filling scheme is such that not all RF buckets have proton bunches. Those empty buckets or beam gaps are necessary to avoid parasitic collision near IP and to make room for beam dump and beam halos known as beam cleaning. The separation in time between two

buckets/bunches filled or unfilled is approximately 2.5 ns. There are about 10^{11} protons per bunch during filling and acceleration. However, during filling and eventual bunch splitting at PS, it is possible that some empty buckets are filled with a much smaller proton population compared to the main bunch. These buckets with few protons can be either trailing the main bunch by $\Delta t = 2.5, 5.0, 7.5, \dots$ ns, or leading the main bunch by $\Delta t = -2.5, -5.0, -7.5, \dots$ ns. If these less populated bunches are 2.5 to 3.0 ns spaced in time from each other, they are referred to as *satellite* bunches and if 5.0 ns, they are referred to as *ghost* bunches. Figure 3.3 shows ghost and satellite bunches and a main proton bunch.

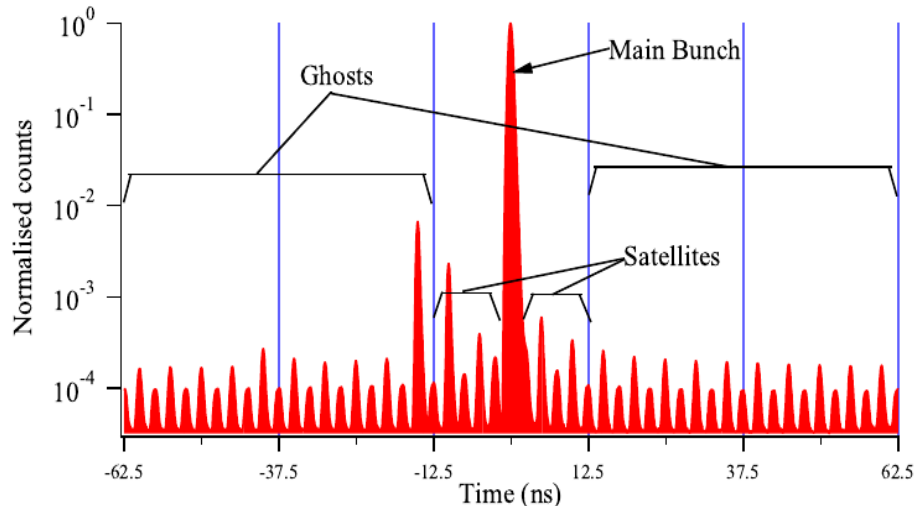


Figure 3.3: Longitudinal Profile taken with Longitudinal Density Monitor (LDM) detector showing definition of Ghost/Satellite bunches with respect to main bunches.

The presence of ghost/satellite bunches increases the uncertainty in LHC luminosity measurements and can also generate proton-proton interactions near but not at the collision region. Effects on ghost/satellite bunches on instantaneous luminosity measurements have been studied using CMS, ATLAS and ALICE detectors. Their results showing clear observation of physics events produced from ghost and satellite bunch collisions is shown in figure 3.4. CMS uses energy deposits in the endcap calorimeters to observe time space which is consistent with the expectation from ghost/satellite bunches while in ATLAS uses the Longitudinal Density Monitor (LDM) detector to study ghost/satellite bunches.

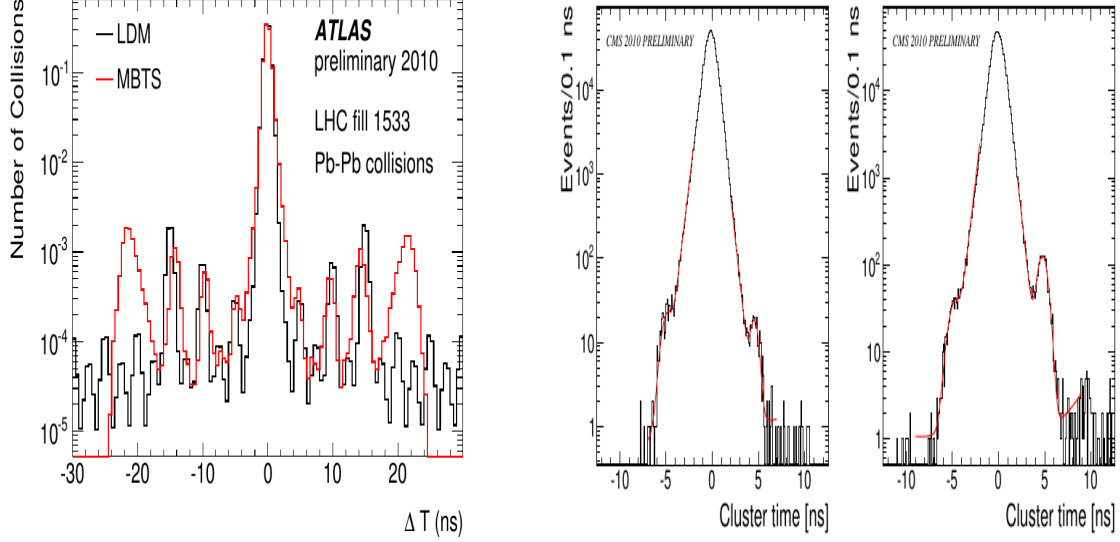


Figure 3.4: (left) Arrival time distribution(red) of ATLAS MBTS for LHC fill 1533 during 2010 Pb-Pb run and LDM profile(black) for Beam2(same for Beam1).
 (Right) Timing of Clusters in the CMS endcap calorimeters for fill 1089:Left: EEP detector(left side of IP $z > 0$) Right: EEM detector(right side of IP, $z < 0$). Plots from ATLAS [30] and CMS, [31]

Table 3.1 gives a summary of the LHC design conditions compared to the conditions used during the LHC RUN 1 operation.

LHC Operation Parameters 2010-2013

Parameter	2010 value	2011 Value	2012/13 Value	Design Value
Beam energy[TeV]	3.5	3.5	4.0	7
β^* in IP 5[m]	3.5	1.0	0.6	0.55
Bunch spacing [ns]	150	75/50	50	25
Number of bunches	368	1380	1380	2808
Protons/bunch	1.2×10^{11}	1.45×10^{11}	1.7×10^{11}	1.15×10^{11}
Normalised emittance[mm.rad]	≈ 2.0	≈ 2.4	≈ 2.5	3.75
Peak luminosity[$cm^{-2}s^{-1}$]	2.1×10^{32}	3.7×10^{33}	3.7×10^{33}	1×10^{34}
Evts/bunch crossing	4	17	37	19
Stored Beam energy(MJ)	≈ 28	≈ 110	≈ 140	≈ 362
Int. Luminosity by CMS[pb^{-1}]				-
Circumference[km]	26.659	26.659	26.659	26.659
Dipole Magnet B[T]	8.33	8.33	8.33	8.33

Table 3.1: LHC operation parameter conditions during RUN 1, 2010-2013

3.2 Compact Muon Solenoid

3.2.1 Overview

The Compact Muon Detector (CMS) is a modern particle detector design for many different particle detection capability. It is one of the general purpose detectors located at one of the proton-proton collision points along the 27 km LHC ring. Its main feature is the presence of a superconducting solenoid of 6 m internal diameter providing a field of 3.8 T for measuring a charge particle's momentum as the particle bends under the influence of this field traveling in the detector. This magnetic field encloses an entirely silicon pixel and strip tracker detector used for vertex finding and for detecting and reconstructing the tracks of charged particles, a lead-tungstate scintillating-crystals electromagnetic calorimeter (ECAL) and a brass-scintillating sampling hadron calorimeter (HCAL). Very long lived particles like muons are measured in gas-ionization detectors embedded in the flux-return iron-yoke located at the outermost section of the detector. It has a simple cylindrical structure consisting of barrel and endcap detectors and an extensive forward calorimetry and detectors to provide a near 4π solid angle coverage assuring good hermetic particle detection. The CMS apparatus has an overall length of 21.6 m, a diameter of 14.6 m, and weighs 12,500 tons. Figure 3.5 shows the CMS detector indicating the different sub-detectors and their material design type. We provide a performance summary and material type of each sub-detector in Table 3.2 of the CMS detector. The CMS uses a coordinate system with the origin coinciding with the center of the detector where proton-proton or nominal collision occurs. This point is commonly referred to as the *interaction point* (IP). The direction of x , y , and z -axes are as shown in figure 3.6. However, for particle identification, CMS uses a more convenient coordinate system based on the polar coordinates. In this polar coordinate system, the azimuthal angle, ϕ , is measured in the $x - y$ plane, where $\phi = 0$, is the x -axis and $\phi = \pi/2$, the y -axis. The radial distance in this plane is denoted R and the polar angle θ measured from the z -axis is related to *pseudo-rapidity*, η , through the relation; $\eta = -\ln \tan(\frac{\theta}{2})$. The coordinate system (η, ϕ) and its radial distance R identifies a point in the cylindrical volume of the CMS detector. In the coming sections, we describe the geometry, material characteristics and functionality of the CMS subdetectors used in our analysis.

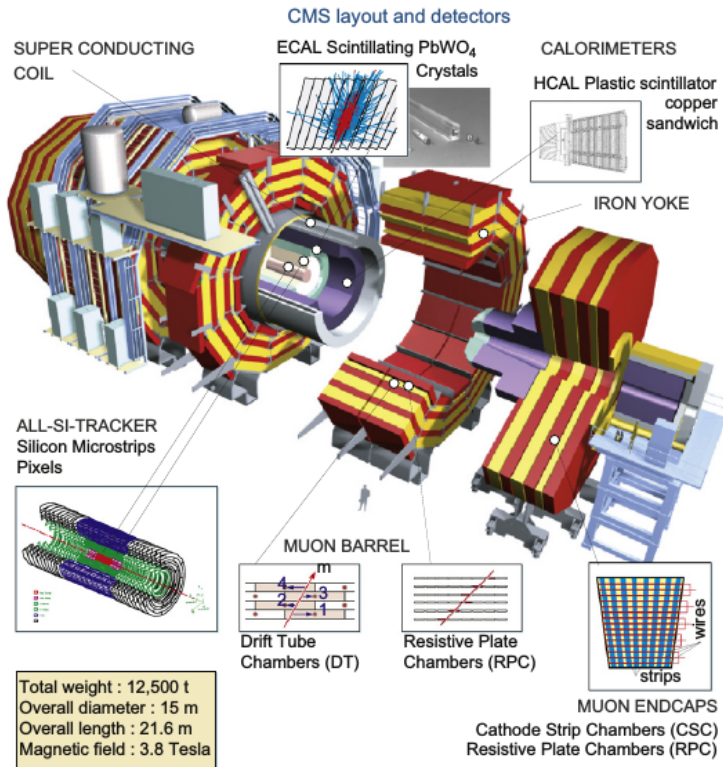


Figure 3.5: CMS Detector showing the different subdetectors and their material.

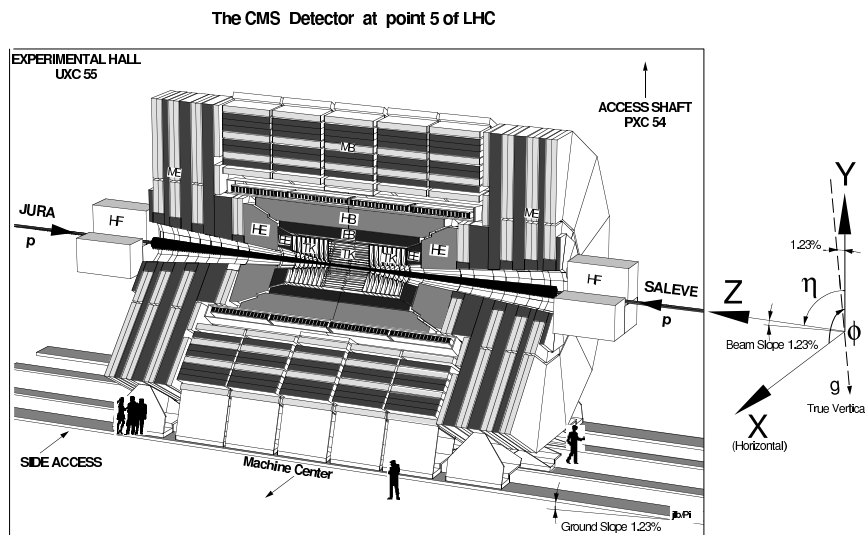


Figure 3.6: CMS detector schematic view with definition of $x - y - z$ coordinates.

CMS Detector and Resolution

Subdetector	Quantity	Resolution	Uses
Tracker	Momentum[GeV/c]	$\sigma_T/p_T \approx 1.5 \times 10^{-4} p_T + 0.005$	Silicon Pixels and Strips
ECAL	Energy[GeV]	$\sigma/E \approx 3\%/E + 0.003$	PbWO ₄ Crystals
ECAL	Time[ns]	$\sigma(\Delta t) = \frac{N}{A_{eff}/\sigma_n} \oplus \sqrt{2}\bar{C}$	PbWO ₄ Crystals
HCAL	Energy[GeV]	$\sigma/E \approx 100\%/E + 0.05$	Brass + Scintillator
Muon Chambers	Momentum[GeV/c]	$\sigma_T/p_T \approx 1\% \quad 50 \text{ GeV to } 10\% \quad 1 \text{ TeV}$	inner tracker + Muon Systems
Magnetic field	B-field strength[T]	3.8 T + 2 T	Solenoid + Return Yoke
Triggers	On/Off-line	Levels	L1(On-line) +HLT(Off-line)(L2+L3)

Table 3.2: CMS detector material, [22], and resolution(Time resolution: $N \approx 35$ ns, $\bar{C} \approx 0.070$ ns [39])

3.2.2 Calorimeter

A CMS calorimeter absorbs a good fraction of energy of an incident particle and produces a signal with an amplitude proportional to the energy absorbed. This absorption is through the cascade production of secondary particles with energy of the incident particle directly proportional to the number of secondary particles produced. There are two types of calorimeters choices used in the CMS detector; the *Electromagnetic calorimeter* (ECAL); for absorbing the energy of electromagnetic particles such as photons and electrons and a *Hadronic calorimeter* (HCAL) made of more than one type of material for stopping and absorbing the energy of hadrons such as kaons and pions through strong interactions. The combined calorimeter detectors of CMS covers a region in $|\eta| < 5$ making it nearly hermetic for good missing energy measurements. The ECAL

and HCAL are arranged in a nested fashion shown in figure 3.7 so that electromagnetic particles can be distinguished from hadronic particles by comparing the depth of the particle shower penetration in both calorimeters.

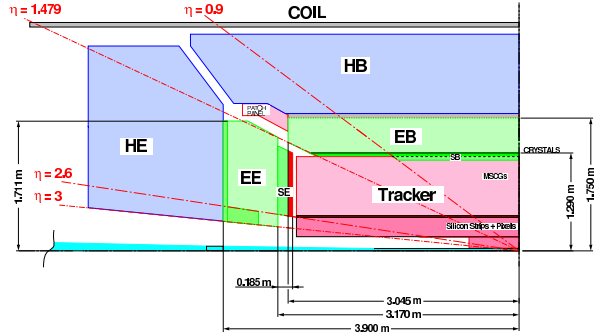


Figure 3.7: Schematic diagram of CMS calorimetry system with HCAL enclosing ECAL in the Barrel and Endcap regions.

Electromagnetic Calorimeter

The electromagnetic calorimeter (ECAL) detects photons and electrons. High energy photons and electrons are detected through their interaction with the lead tungstate (PbWO_4) crystals. During this interaction which happens either through electromagnetic showering or electron-positron pair production (*bremsstrahlung*), the incoming photon or electron deposit practically almost all of its energy. There are 75848 crystals in total mounted in a cylindrical geometry, with a barrel (EB) and an endcap (EE) structure. The choice of PbWO_4 crystals as calorimetry material by CMS for operation in the LHC environment is because of its a high density (8.28 g/cm^3), short radiation length ($X_0=0.89 \text{ cm}$) and a small Molière radius (22 cm). In a high radiation dose and fast timing (25 ns proton bunch spacing) environment like the LHC, PbWO_4 crystals is preferred to other crystal materials for its high radiation resistance and a scintillation decay time which is comparable to the LHC bunch crossing interval of 25 ns and about 80% of the light is emitted in 25 ns. The probability of an electromagnetic object with high energy to interact either through *Bremsstrahlung* or *pair production* with the material in ECAL is proportional to the nuclear charge, Z , of the material. PbWO_4 is a high Z material and this makes it once more the preferred material choice for electromagnetic calorimetry by CMS. The small Molière radius ensures that on average about

95 % of the electromagnetic shower energy is contained within a crystal crystal volume of about 9 crystals. This reduces the transverse spread of the electromagnetic cascade from multiple scattering of electrons and helps improve on the estimation of the transverse position of impact of an incident particle. It also provides a fine granularity for measuring the particle's energy by providing fewer overlap of particle signals. Its dense nature also allows for the electromagnetic shower to develop early and therefore likely to be fully contained within a compact device like CMS.

The EB section of the ECAL covers a pseudo-rapidity of $|\eta| < 1.479$. It has 61,200 crystals providing a granularity of 360 degree fold in ϕ and (2×85) -fold in η . The crystals are mounted in a quasi-projective geometry so that their axes make an angle of 3% with respect to a line vector from the nominal interaction vertex in η and ϕ directions. This avoids cracks aligned with a particle's trajectory. A crystal in EB is approximately 0.0174×0.0174 in $\eta - \phi$ or $22 \times 22 \text{ mm}^2$ at its front face and $26 \times 26 \text{ mm}^2$ at its rear face. Each crystal is 230 mm long corresponding to about $25.8 X_0$ radiation lengths. The crystal's radial distance measuring from the center of the face of the crystal to the beam line is 1.29 m. A number of crystals are placed in a thin-walled alveolar structure made with aluminum forming a *submodule*. Each submodule is arranged into 4 modules of different types according to their η position. There are about 400 to 500 crystals in each module and these 4 combined make one *supermodule* containing 1700 crystals. To reduce crystal reflective lost, the aluminum surface is coated to avoid oxidation leading to coloration. On the rear end of each EB crystal, two *Avalanche Photodiodes* (APD) is glued to collect the scintillating light from the crystals converting light into charge current which is further collected by the read-out electronics.

The endcap sector covers a pseudo-rapidity region of $1.479 < |\eta| < 3.0$ with a Preshower (ES) detector made of silicon strip sensors interleaved with lead placed immediately in front of it. The purpose of the preshower is to identify photons from the decay of neutral pion, $\pi^0 \rightarrow \gamma\gamma$ and also to help separate photons producing electrons through pair production from photons not producing electrons before their arrival at the EE. The endcap located on the $+z$ side of the nominal interaction is denoted EE+ while the other located on the $-z$ side is denoted as EE-. The longitudinal distance between the IP and the center of the surface of the EE crystals is 3.154 cm. Each endcap is divided into two halves called *Dees* with each Dee holding 3662 crystals. Crystals in EE with identical shape

are grouped into 5×5 units called *supercrystals* (SC). The crystals in the SC form an $x - y$ grid. Each crystal is 220 mm ($24.7 X_o$) in length and has a front face and rear cross section of 28.62×28.62 square mm and 30×30 square mm, respectively. Vacuum Phototriodes (VPT) instead of APDs is glued on the rear face of each crystal for scintillating light conversion into electrical signals. The VPT is used in the EE because of its high resistance to radiation and smooth operation in a strong magnetic field environment. These APDs and VPTs are used because of their high gain relative to regular photodiodes with no gain and the fact that they are not affected by the high magnetic field. Although the light yield for PbWO_4 crystals is rather low (≈ 70 photons/ MeV), these photo-detectors have internal gain (50 for APDs and 10 for VPTs) and quantum efficiency of 75 % for APDs and 20 % for VPTs of the emission wavelength. This makes it possible that signals from incident particles with energies of a few to high GeV longer than noise.

The signals from the APDs and VPTs are digitized by voltage-sensitive analogue-to-digital converters and through fibre-optic links transported as light signals to the counting room located adjacent to the experimental cavern.

The energy resolution and geometry structure of the ECAL ensures that the photon or electron's arrival energy, time, position and even the direction through the shape of its electromagnetic shower in the crystals can be identified and measured with good precision.

Hadronic Calorimeter

The CMS Hadron Calorimeter (HCAL) is comprised of four distinct subdetectors: the Barrel (HB), the Endcap (HE), the Outer Barrel (HO), and the Forward (HF). Unlike the ECAL, the HB, HE and HO subdetectors are scintillator-sampling calorimeters with embedded wavelength shifting fibers (WLS). HB, HE and HO uses brass plates as the inactive material and plastic scintillator with WLS as the active material. The brass plate is used for absorbing the hadronic shower which comprise of an *electromagnetic*(particles like π^0 s, η s and other mesons generated in the absorption process and decay to γ s which develop electromagnetic (em) showers) and *non-electromagnetic* components. The plastic scintilator is divided into 16 η sectors resulting in segmentation of $\Delta\eta \times \Delta\phi = 0.087 \times 0.087$. It was chosen for its long-term stability and moderate

radiation hardness. energy. The scintillating light through the WLS brings the light to hybrid photodiodes (HPDs) in the HB and HE. HPDs which have high electrical noise and will be replaced with silicon photon multipliers (SiPM) which have low noise during the current CMS detector upgrade. The HB and HE combine cover a region in pseudo-rapidity of $|\eta| < 3$. The HB covering the region $|\eta| < 1.3$, is divided into two-half barrel (HB+ and HB-) sections each composed of 18 identical 20° wedges in ϕ . Each wedge is made of flat brass alloy and steel(only front and back plates) absorber plate. HE covers $1.3 < \eta < 3.1$ and has plastic scintillation tiles with granularity of $\Delta\eta \times \Delta\phi = 0.087 \times 0.087$ for $|\eta| < 1.6$ and $\Delta\eta \times \Delta\phi = 0.17 \times 0.17$ for $|\eta| > 1.6$. The HO is an extension of HB outside the solenoid and thus utilizes the solenoid coil as an additional absorber. It is used to identify the starting shower and to measure the shower energy deposited after HB. The first active layer of the scintillating tiles is situated directly behind the ECAL in order to actively sample low energy showering particles from the support material between the ECAL and HCAL.

The HF occupies a pseudo-rapidity region of $3 < |\eta| < 5$. Its purpose is to provide a closer to 4π hermetic phase space coverage required for missing transverse energy calculation or MET. MET is the established signal for very weakly interacting particles like neutrino and supersymmetric particles like gravitino which travel through the detector undetected. HF consists of radiation hard quartz fibers embedded in steel absorbers running parallel to the beam axis. The signal from Cherenkov light emitted in the quartz fibers in response to charged particles makes it possible to detect all charge particles in the forward region. The HF calorimeter has long and short fibers for better sampling and to distinguish showers generated by electrons and photons from those generated by hadrons. The choice of quartz fibers is because of its high resistance to the high radiation in the forward detectors and its fast production of light through Cherenkov process.

For $|\eta| < 1.48$, the HCAL cells map on to 5×5 ECAL crystal arrays to form calorimeter towers projecting outwards from near the nominal interaction point. In each tower, the energy in ECAL and HCAL cells is summed to define the calorimeter energy tower. The energy ratio of an HCAL tower to an ECAL in a calorimeter energy tower can be used to improve photons and electron identification.

3.2.3 Muon Chambers

Muons unlike electrons and hadrons do not deposit most of their energy in the calorimeters. They are capable of traveling across the entire CMS detector into the muon chambers. Muons produce tracks which run across the CMS detector starting from the silicon pixel and strip subdetector closest to the IP called the *Tracker* and depositing very little fraction of their energy in the calorimeters unto the muon chambers. The muon chambers use the process of ionization and a 2 T magnetic field from the return iron yokes (bending the tracks of charge particles) to measure the momentum of charged particles. The three different types of muon chambers used by the CMS are: the drift tubes (DT) chambers in the barrel, cathode strip chambers (CSC) in the endcaps and resistive plate chambers (RPC) glued to the DT and CSC chambers. Four layers or stations of DT/RPC and CSC/RPC are embedded in an interleaved style with the iron yoke for track reconstruction and triggering. Figure 3.9 is a longitudinal view of the CMS detector showing the position of the muon stations. The DT and CSC record track segments characterized by the position of the track and the bending angle. This information is used to determine the precise transverse momentum and charge of particles during particle reconstruction. The RPCs(DTs and CSC will also be used after the current detector upgrade) are dedicated L1 trigger chambers used to determine the candidate muon's approximate transverse momentum and proton bunch crossing number. The RPC has a timing resolution of about 3 ns.

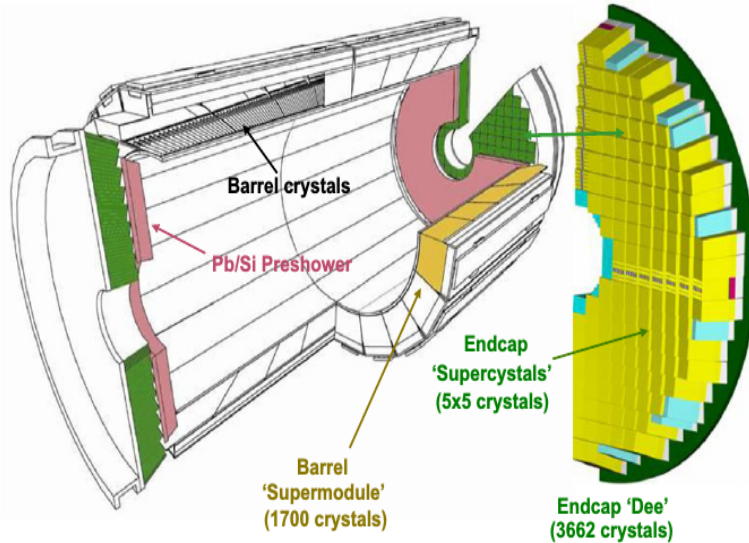


Figure 3.8: Layout of the CMS electromagnetic calorimeter showing the arrangement of crystal modules, supermodules in the barrel with the preshower in front of endcap with supercrystals.

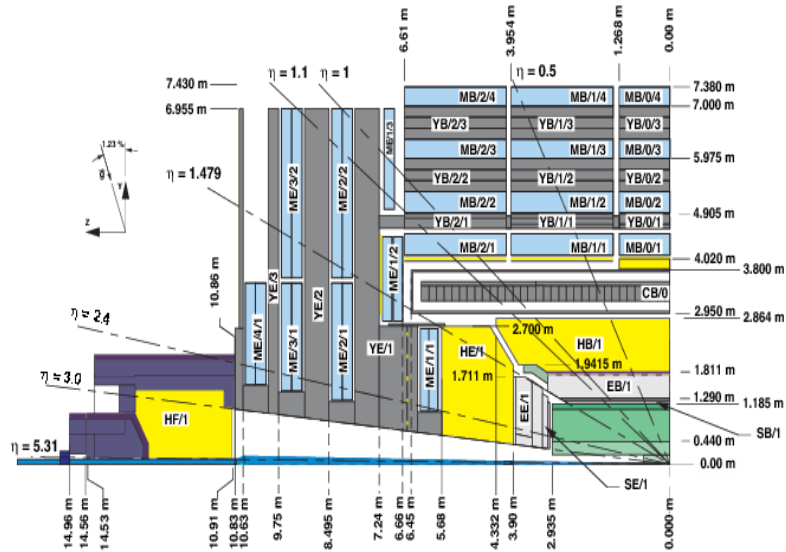


Figure 3.9: Cross section view showing the coverage range of CMS sub-detectors and their longitudinal distance from the IP.

3.2.4 Triggering

In CMS, there are a billion interactions including *pile up* (PU) happening each second. This means data from each 25 ns proton-proton collision has to be processed and stored before the next collision happens. Also, since not all these collisions produce interesting physics events, we have to be capable of selecting only interesting physics events produced from proton-proton collisions with sufficient energy. The process of selecting such interesting events is called *triggering*. CMS uses a two level triggering system for selecting interesting events produced with enough energy from collisions. The comprise of the *Level-1* (L1) and *High Level Triggers* (HLT) triggers.

The L1 triggers is a hardware designed electronics system implemented in FPGA and ASIC technology and uses information from the calorimeter, muon trigger and a global trigger board. The global trigger board makes the final decision based on the calorimeter and muon triggers to reject or keep an event for further processing at the HLT trigger. The L1 trigger is responsible for selecting the best 100,000 events/second from the initial 1 billions events/second produced.

The HLT is a software comprised of implemented selection algorithms running on a farm of more than 1000 standard computers. These complex algorithms include instructions like, match tracks to hits from the muon chambers, select energy deposits above a certain threshold in the calorimeters with no tracks for electromagnetic objects, and begins the first step of event selection. Just like the L1 trigger, the HLT uses assimilated and synchronized information from different parts of the CMS detector to create the entire event. By the time this selection process is complete, there are now only 100 events/second with the remaining 99,900 thrown away. Taking an average event size to be 1 Megabyte, in a stable and effective LHC proton collision period of a year or 10^7 seconds, CMS produces about a Petabyte of data which is stored and used later for offline physics analysis.

Chapter 4

Time Reconstruction and Resolution

ECAL Time Overview

The ECAL was designed to precisely measure the energy of electrons and photons produced in proton-proton collisions, with a target barrel resolution of 0.5% for photons with energies larger than 50 GeV. In addition to energy measurements, the combination of fast scintillation for PbWO₄ crystals, the electronic pulse shaping and sampling rate of 40 MHz allow for excellent time measurements to be made with ECAL. A pulse shape matching of less than 1% non-linearity by the pulse shaping chip in each channel, ensures a linear and uniform pulse height from among all the channels in the ECAL. The time measured by each channel is reconstructed from 10 discrete samples of the digitized analog pulse height of the electronics, using a time reconstruction algorithm.

4.1 Electromagnetic Calorimeter Readout Electronics

The scintillating light from the PbWO₄ crystals is readout and converted into electric current using Avalanche Photo-Diodes (APD) and Vacuum Photo-Triodes (VPT) in the barrel and endcap detector regions, respectively.

The ECAL electronics readout and control system comprise of the Front End (FE) electronics (mainly consisting of radiation hard ASIC chips) installed inside the detector

volume at the back of ECAL and the Off Detector (OD) electronics in the upper counting room. the FE electronics is connected to the OD electronics by 100 m radiation hard Gigabit Optical fiber Links (GOL) for transporting the optical data stream.

The FE has a crystal arrangement in matrixes of 5×5 crystals called *Trigger Towers* in barrel, which is based on the electronics arrangement and a 5×5 mechanical arrangement of crystals called *Super-Crystals* in the endcaps. Each FE board hosts five Very Front End (VFE) boards with each holding five analog channels shown in right schematic diagram of Figure 4.1. Each channel, shown in the left schematic diagram of Figure 4.1, consists of a Multi-Gain Pre-Amplifier (MGPA) and a 12 bit Analog-to-Digital Converted (ADC) used to amplify, shape and digitize the signal coming from the Photo-Diodes.

The MGPA chip uses 3 gain ranges with gain ratios of 1,6 and 12 to span the overall dynamic range of the signal. Equipped with a CR-RC filter with a pulse shaping time of 40 ns and less than 1% of non-linearity, the MGPA ensures a linearity and pulse shape matching across all three ranges which allows for precise pulse shape reconstruction. The readout and precision performance requires a multi range 12-bit ADC chip with a sampling frequency of 40 MHz to digitize the analog pulse signal of the highest unsaturated range into 10 discrete samples, with an electronic noise of about 40 MeV.

The FE board also is also equipped with a Clock and Control Unit (CCU) chip which enables the exchange of control information between the OD and the FE electronics through a Clock and Control link.

The digitized data are stored in pipeline buffers until a Trigger Level 1 (LV1) accept decision is made. At the same time the digitized data are sent to a digital signal processing FERNIX chip which performs Trigger Primitive Generation (TPG) for the LV1 trigger system. The TPs are sent to the Trigger Concentration Card (TCC) on the OD electronics at a rate of 1 word/25 ns. Upon a positive trigger LV1 decision, the data samples corresponding to a single event are transferred to primary event buffers which are eventually merged and sent to the Data Concentration Card (DCC) through Readout links at 800 Mbps. The crystal readout data from the FE board is collected by the OD electronics DCC.

The OD board hosts the DCC, TCC and a Clock and Control System card (CCS). The TCC completes TPG process by combining the TPs generated and transmit them

to the regional Calorimeter Trigger system while the CCS is primarily task with distributing fast timing signals (LHC 40 MHz clock and trigger commands) to the FE and OD electronics and to synchronize their operation. A common clock distribution serving 5×5 readout unit of the FE helps minimize channel-to-channel synchronization.

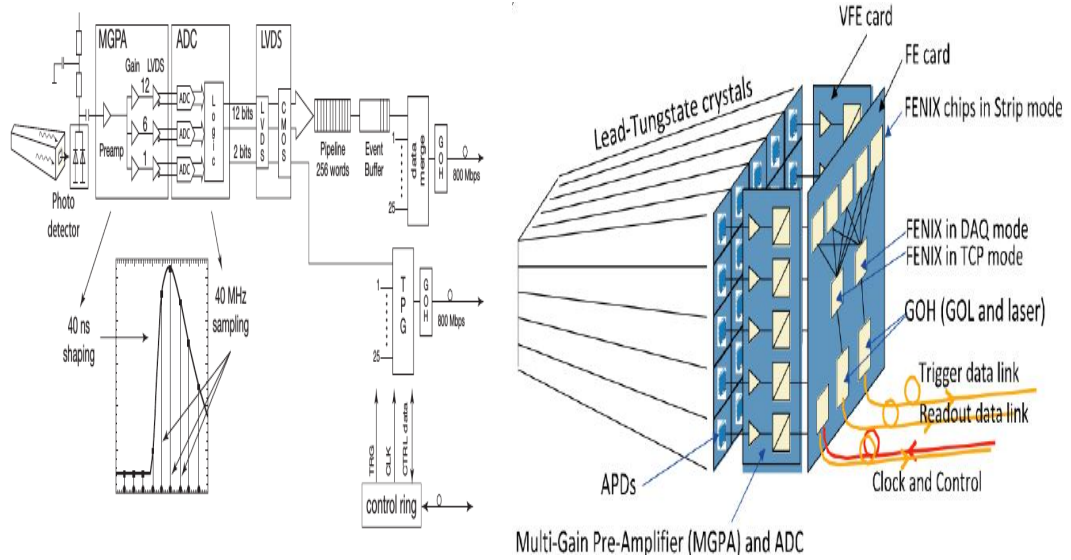


Figure 4.1: Schematic diagram of the CMS ECAL electronics readout for a single channel(Left) and the entire Trigger Tower or Front End (FE) Card(Right).

4.2 Time Reconstruction

An analog pulse shape from a single channel is shown in Figure 4.2(a). Overlaying the pulse shape are typical 10 digitized samples in red. The first three samples are taken in the absence of a signal and correspond to the pedestal. The ADC chip responsible for the digitization, has a sampling frequency of 40 MHz, i.e. one sample is made every 25 ns, which is the same rate as the LHC proton-proton bunch collision frequency of one bunch crossing every 25 ns. In addition, the timing phase between each sample and the next is adjusted so that the maximum of the signal pulse shape corresponds to one of the samplings within 1 ns. A time reconstruction algorithm uses these 10 digitized samples to measure the time of a single channel by finding the precise time corresponding to the maximum of the pulse shape, T_{\max} .

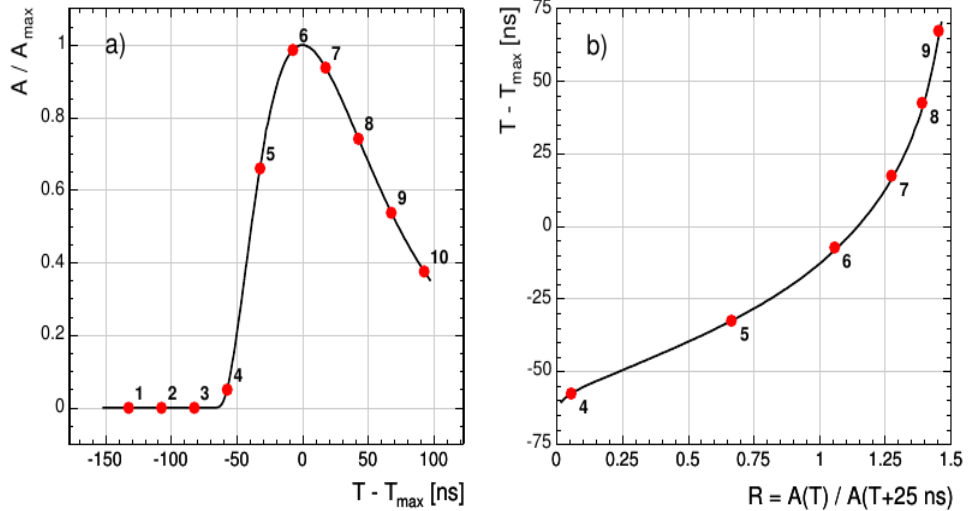


Figure 4.2: (a) A measured ECAL pulse shape for a single channel. (b) $\mathbf{T} - \mathbf{T}_{\max}$ Vs $R(T)$ relationship whose inverse is $T(R)$. Solid line is pulse shape from test beam while dots are typical 10 discrete samples corresponding to signal from proton-proton collision.

Precise measurement of \mathbf{T}_{\max} relies on good knowledge of the pulse shape. To find \mathbf{T}_{\max} using the pulse shape, a ratio algorithm uses the ratio

$$R_i = A(T_i)/A(T_{i+1}), \quad (4.1)$$

where T_i is the time of the time of the beam crossing that the i^{th} pulse height sample is taken. Each pulse height ratio is uniquely determined from the pulse shape as shown in Figure 4.2(b) which shows the the pulse height ratio, R_i , as a function of the time that the pulse height of the first of a pair of samples is taken relative to the time of the maximum height of the pulse, $\mathbf{T}_i - \mathbf{T}_{\max}$. Using the inverse of this function, $T(R)$, we can obtained $\mathbf{T}_{\max} = T_i - T(R_i)$ and the uncertainty, σ_i , for each R_i point.

The uncertainty on each measurement is a product of the derivative of the function $T(R)$ and the uncertainty on the value of R_i which itself depends on three separate uncertainties: the noise fluctuation (σ_n) of each sample, the uncertainty in the estimation of the pedestal value which is always subtracted from the measured value and the truncation during 12-bit digitization. These uncertainties are uncorrelated and can be added in quadrature,[35].

A more precise value of T_{max} is obtained by using the ratios R_4 through R_7 . The other ratios are not used for the estimation of T_{max} because their associated uncertainties are large due to the large slope of the $T(R)$ function. A weighted average of each T_{max} and σ obtained from ratios R_4 through R_7 as expressed in Equation 4.2 gives the best estimate of T_{max} and uncertainty.

$$T_{max} = \frac{\sum \frac{T_{max,i}}{\sigma_i^2}}{\sum \frac{1}{\sigma_i^2}} , \quad \frac{1}{\sigma_T^2} = \sum \frac{1}{\sigma_i^2} \quad (4.2)$$

The sum is from $i = 4, \dots, 7$.

4.3 ECAL Time Performance from Test Beam

4.3.1 ECAL Time Resolution

The intrinsic time resolution of ECAL, $\sigma(t)$, measured during test beam, consist of three main contributions which can be summed in quadrature since they are uncorrelated. These three contributions are the noise, stochastic and constant terms. The *Noise* (N) term arises from the electronic noise, coherent movement of the baseline and effects overlapping hits some of which come from other soft proton-proton collisions called *pile up* (PU) events. The *Stochastic* term (S) is from fluctuations in the number of photons collected during the sample times. Lastly, the *Constant* term (C), whose contribution is independent of the energy deposited and arises from variations in the point of shower initiation within the crystal and variations in the pulse shape for each channel. The full expression for time resolution with all three contributions is given in Equation 4.3,

$$\sigma^2(t) = \left(\frac{N}{A/\sigma_n} \right)^2 + \left(\frac{S}{\sqrt{A}} \right)^2 + C^2, \quad (4.3)$$

where A is the measured amplitude corresponding to the energy deposited and σ_n is the intrinsic noise in the amplitude for individual channel. σ_n has a value of 42 MeV and 140 MeV in the barrel and endcap, respectively. $N = 33$ ns has been estimated from Monte Carlo (MC) simulation studies. Contribution from the stochastic term, (S) is small, with a value of $S < 7.9$ ns·MeV^{1/2}.

To measure the intrinsic time resolution of ECAL and study the pulse shape, H2 and

H4 test beam facilities at CERN were used. Prior to installation at the CMS detector, about 25% of the barrel and endcap crystals were exposed to electron beams with energy between 15 GeV and 250 GeV. The time resolution was obtained from the Gaussian distribution of the difference in time of two crystals sharing energy and belonging to the same electromagnetic shower. Note that the contribution from crystal-to-crystal synchronization does not contribute to the constant term in this study. Neglecting the stochastic term because its contribution is negligible, Equation 4.3 reduces to:

$$\sigma^2(t_1 - t_2) = \left(\frac{N}{A_{eff}/\sigma_n} \right)^2 + 2\bar{C}^2 \quad (4.4)$$

where $A_{eff} = A_1 A_2 / \sqrt{A_1^2 + A_2^2}$, while $t_{1,2}$ and $A_{1,2}$ are the times and amplitudes of the two crystals. \bar{C} is their residual constant term contribution. The time resolution is measured from the standard deviation of a Gaussian fit to the time distribution from each slice of A_{eff}/σ_n of the A_{eff}/σ_n distribution. The resulting distribution of $\sigma(t_1 - t_2)$ of these standard deviations plotted against A_{eff}/σ_n is used to extract the noise and residual constant terms. The result presented in Figure 4.3 gives a noise factor $N = (35.1 \pm 0.2)$ ns and $\bar{C} = (20 \pm 4)$ ns obtained from test beam experiment.

The value of the N in this study agrees with our Monte Carlo estimate to within 6%. Other studies of the timing resolutions using the time difference between two basic clusters of separate electromagnetic shower was used and the results gave similar values of N .

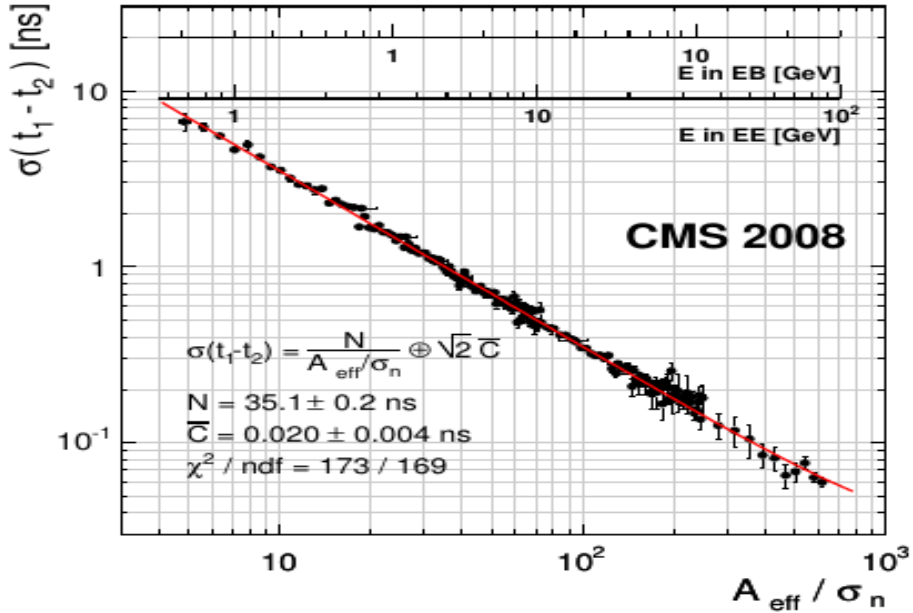


Figure 4.3: Difference in the time measurements as a function of A_{eff}/σ_n of two crystals sharing an energy and belonging to the same electromagnetic shower obtained during electron testbeam measurements. The single crystal energy scales for barrel (EB) and end-cap (EE) is overlaid. The fitted results give $N = (35.1 \pm 0.2)$ ns and $C = (20 \pm 4)$ ns.

An intrinsic time resolution better than 0.1 ns for energy $E > 20$ GeV in EB is realized from test beam. Knowing that it takes on average 4.3 ns for a photon to reach the ECAL surface produced from proton-proton interaction point, this demonstrates an intrinsic time resolution of 2% for photons with energy $E > 20$ GeV in the barrel.

4.4 ECAL Time Performance from Collision

Ofcourse, we do not expect the ECAL time resolution in the LHC proton-proton collision environment to be as precised as test beams studies show. Therefore, it is imperative to determine the ECAL time resolution in an LHC environment as knowing the ECAL time resolution in LHC operation can be used for other purposes like eliminating particles such as cosmic rays, beam halo muons, electronic noise and out-of-time proton-proton interactions with broad time distributions. There are factors like clock time variations

over extended time, timing bias with energy and losses in crystal transparency due to radiation which would lead to different pulse shapes which worsen the ECAL time resolution. Thus, a robust crystal time calibration procedure is required if we are to match the intrinsic time resolution realized in test beam studies that we mentioned above. In addition, precise ECAL time during collision can be used in the search for photons with late arrival time produced from the decay of slow moving particles with $\beta \ll 1$, photons traveling along a path which significantly deviates from the obvious straight path from the proton interaction point.

4.4.1 Time Calibrations

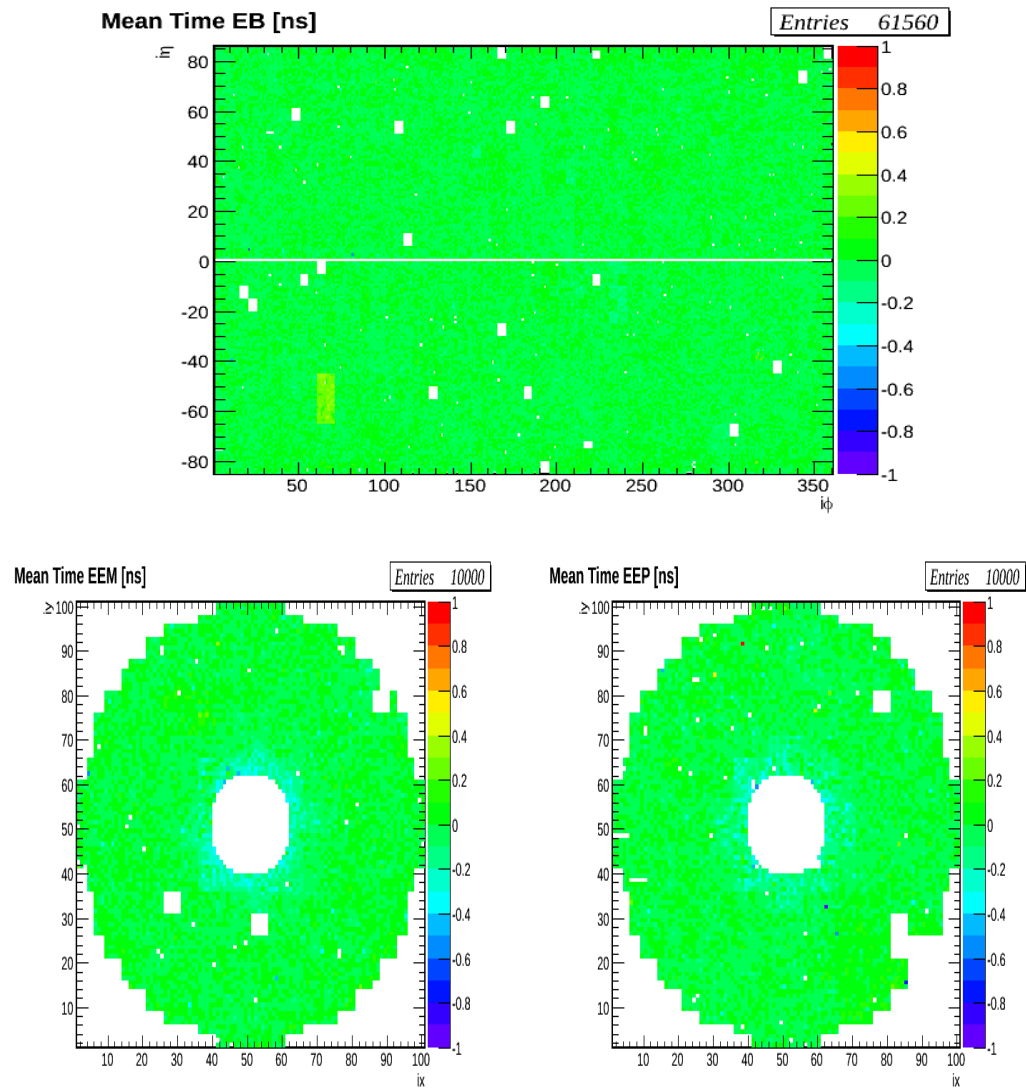
Variations in the crystal time maybe caused by the non-uniform response to electromagnetic showers of each crystal causing difference in pulse shapes or by clock time shifts introduced by interventions during technical shutdowns for machine repairs. These variations can be about 1 to 3 ns on average. To reduce these contributions, we continuously time align all 75,848 PbWO₄ crystals in ECAL by performing crystal *time calibration* once or twice every month. Time calibrating these crystals ensures that there is a uniform response by all the crystals to photons produced from proton-proton collisions, at interaction point, and traveling along a straight path with speeds close to the speed of light to ECAL. It equally guarantees the synchronization of most particles of an event and assigns each event to the correct LHC proton bunch crossing.

The presence of the “ T_{max} Phase”, the difference in pulse shape between each crystal, variation in time of flight by a few nanosecond (ns) and the different intrinsic delays in each channel motivates a time calibration at two separate levels. At the level of the front end electronics (FE) consisting of 5×5 crystals, We perform an initial internal time synchronization by adjusting the time measured by each trigger tower in steps of 1.04 ns among all the trigger towers. Determining the trigger tower time constants needed for time aligning these trigger towers takes place during the process of *Hardware Synchronization*. Offline, we assign time constants to each crystal, during hit reconstruction using the CMS reconstruction software during the transition from uncalibrated hits to calibrated hits.

Offline Time Calibration

The purpose of the offline calibration is to provide time calibration constants for each crystal during event reconstruction. These constants are derived from data recorded during proton-proton collisions and are used to adjust for any clock time shift. A crystal time shift of about 1 ns is caused by the relative time shift between the CMS and the LHC clocks and time shift of about 3 ns to 5 ns is caused by time offsets in the local CMS clock introduced during hardware interventions. The local time offsets is specific only to certain regions of the ECAL detector. The calibration constants for each crystal is the reverse sign of the average time of all the reconstructed energy deposits (rechits) in the crystal. New sets of calibration constants are produced each month throughout the entire LHC run period. Each set of time constants produced has an *interval of validity* (IOV). A total of 17 IOV time constants were produced for the entire LHC run in 2011 and 44 IOV time constants for 2012.

The data sample use for producing the calibration time constants contains mostly electromagnetic particles of mostly loosely triggered photon, electron and hadrons with large electromagnetic shower which travel with nearly the speed of light and largely deposit most of their energy at ECAL. Events of these data samples undergo a rigorous event selection process in order to minimize contamination from events not produced from proton-proton collisions like cosmic muons, beam halos and electronic noise. The produced constants are validated through a full cycle hit reconstruction-time adjustment-hit re-reconstruction procedure of a chosen sub data sample. The validate constants are then used during full event reconstruction. The maps in Figure 4.4, show two dimensional distribution maps of the average time (time calibration constants) for each of the 61,200 crystals in EB and 14648 crystals in EE. The figure shows each crystal average time before (*top 3 plots*) and after (*bottom 3 plots*) calibration. More information about crystal time calibration for the entire LHC Run 1 is found in [36].



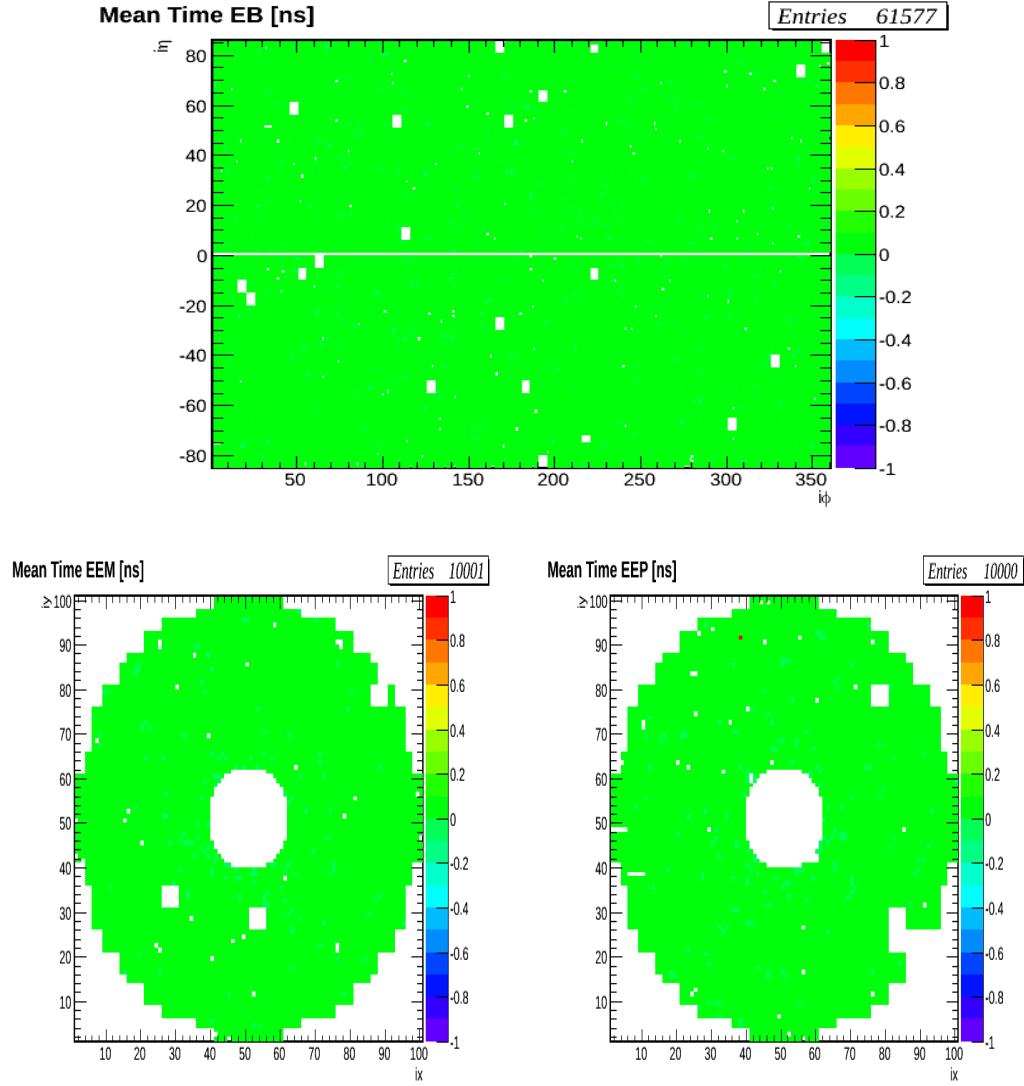


Figure 4.4: *Top 3*: Time calibration maps showing the distribution of mean time for each channel/PbWO₄ crystal in EB (top) and EE (below: EE-(left), EE+(right)) before calibration. *Bottom 3*: Time calibration maps showing the distribution of mean time after calibration. After calibration most crystals have an average time of zero(GREEN).

Hardware Time Calibration

Time offsets introduced during hardware interventions for ECAL front end electronics repairs are calibrated at the level of trigger towers. Most often the adjustment of the

hardware time latency happen during the process of CMS data recording. These time alignments can be done using either data from proton-proton collision or from laser.

Hardware Time Calibration With Collision

The approach for adjusting hardware time offsets during CMS data recording with ECAL for stable proton-proton collision beams involves interfering with the data recording process in order for the hardware time adjustments to be made. This interference during stable proton beams causes frequent data recording downtimes leading to data lost. Frequent down times is one of the causes for the difference between the luminosity recorded by CMS detector compared to luminosity delivered by the LHC. Even though we can argue that this procedure for adjusting the observed trigger tower time shifts using collision data is self efficient, the large CMS data recording downtime and loss of luminosity makes it less dependable especially during frequent machine interventions. To remedy the situation, a laser based time latency adjustment approach can be used.

Hardware Time Calibration With Laser

The ECAL laser system comprise of two lasers, a 440 nm wavelength (close to peak emission for PbWO₄ crystals) laser for monitoring crystal transparency losses and a 796 nm wavelength laser for monitoring readout electronics chain from photodetectors to the electronics (i.e. APDs to ADCs). Both lasers have a jitter of less than 4 ns and as a result, the time from the lasers is averaged over 600 event pulses. The time for each crystal from the laser is expected to be the same as the time from collision data and is represented as $T_{\text{MAX}}^{\text{APD}}$. The laser system is also equipped with a fast acquisition card called MATACQ. The time for each channel recorded using the Matacq is also averaged over 600 event pulse and denoted T_{MATACQ} . The difference, $T_{\text{MAX}}^{\text{APD}} - T_{\text{MATACQ}}$, of the two times, averaged over the 25 crystals of a Clock and Control Unit (CCU) is used as the time for each CCU, $t_{\text{CCU}} = \langle T_{\text{MAX}}^{\text{APD}} - T_{\text{MATACQ}} \rangle$. To obtain the time shift of 25 crystals belonging to the same Front End (FE) electronics, we monitor for change of this time average before (t_{CCU}^B) and after (t_{CCU}^A) hardware intervention during detector maintenance. The time difference, $\Delta t_{\text{CCU}} = t_{\text{CCU}}^A - t_{\text{CCU}}^B$, is averaged over all the 25 crystals, i.e. $\langle t_{\text{CCU}}^A - t_{\text{CCU}}^B \rangle$, is the time shift, and the time calibration constant for the CCU is of opposite sign so that after correcting, the average time

of the CCU is zero. This is done for all the 68 CCUs in a given supermodule (SM) or front end detector (FED). The global time shift of a given FED is caused by the non-homogeneous laser light distribution on all CCU or trigger towers. Each FED has 1,700 PbWO₄ crystals and we produced laser based time calibration constants for all its crystals. Using laser data, we are able to measure the time shift of each CCU to within 0.2 (0.5) ns EB (EE) in precision. Compared to calibration using collision data, there are no downtime in CMS data recording as we can adjust for any hardware time shift prior to stable proton beams. The full procedure including technical details for performing hardware latency adjustments online using collision data or laser data is well described in [37].

4.4.2 Time Bias

An additional source contributing to poor time measurement arise from energy related time bias. This bias originates from the time reconstruction algorithm. It is expected that the ratio approach for time reconstruction performs efficiently for all ADC counts. However, during data recording in LHC Run 1, it was observed that for high ADC counts produced by very energetic particles, an inherent bias in the time is introduced by the multi-gain pre-amplifier electronics for electromagnetic particles with energy above certain gain transition points. The full conversion of the energy of a particle recorded by a crystal in ADC counts to GeV is expressed as; $E_i = G \cdot S_i(t) \cdot C_i \cdot A_i$, where A is the amplitude from the pulse shape in ADC counts, G is the ADC-to-GeV conversion factor equal to 0.039(0.063) in EB(EE), C_i is the inter-calibration coefficients accounting for individual channel response to the electromagnetic shower and $S_i(t)$ is the correction term obtained from laser accounting for radiation-induced channel response. S_i changes over time. The first gain transition point (Gain-1) of the multi-gain pre-amplifier occurs at 4096 ADC counts corresponding to 159.744 GeV in EB and 258.048 GeV in EE. The subsequent Gain 6 and 12 transitions occur at energy values of TeV.

The ratio algorithm introduced time bias at gain transition points which need to be adjusted. These adjustments are made on an energy dependent basis during event reconstruction for a particular CMS event reconstruction software (CMSSW) release. Figure 4.5 shows the comparison between two CMS event reconstruction software releases, CMSSW44X, where these time bias corrections have not been made and CMSSW53X,

where the the corrections have been made. Evidently, the average time displayed in both CMSS44X and CMSS53X show the disappearance of the time bias for all particle energy in CMSSW53X after the time bias corrections were made.

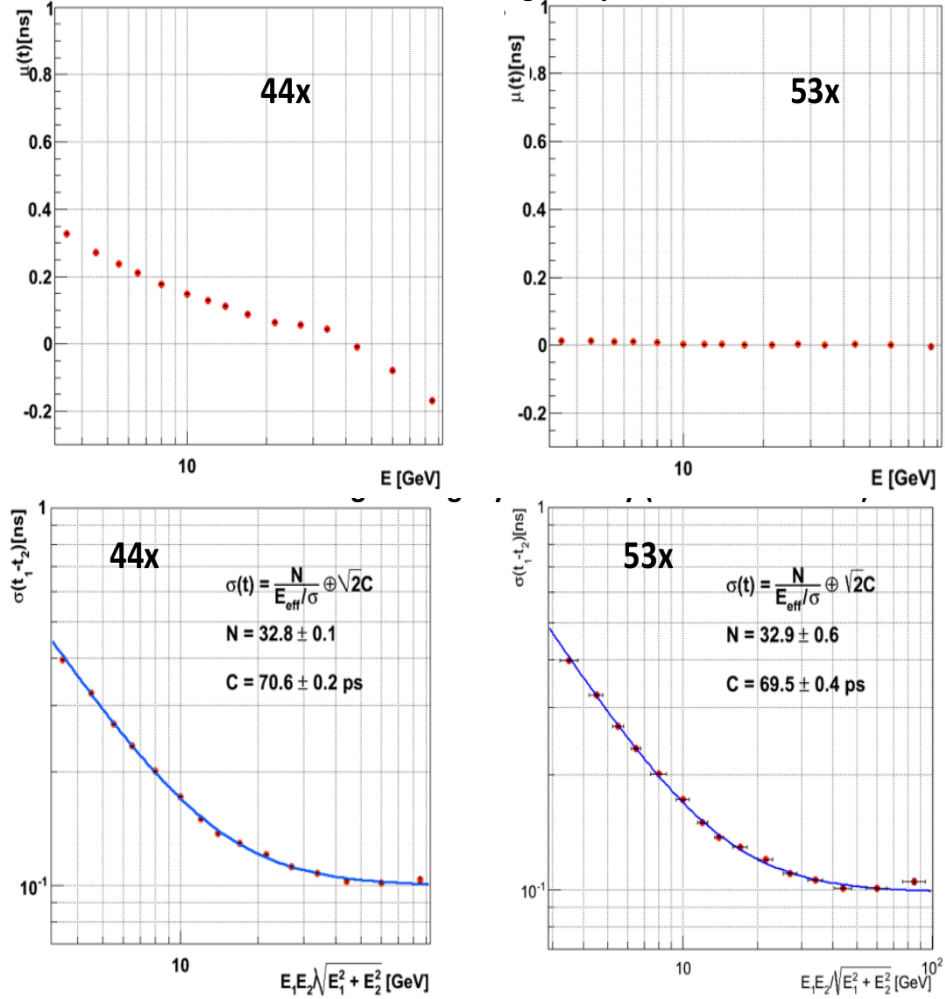


Figure 4.5: Distribution of mean time (μ , top row) and time deviation (σ , bottom row) as a function of crystal energy for EB prior (left) and after (right) time bias corrections depending on energy have been applied.

To investigate further for any additional time bias un related to the particle energy, we study how the crystal geometric position in ECAL covering from $\eta = 0$ to $\eta = 3.142$. The results shown in Figure 4.6 show no crystal position or η dependence. However, time bias of the order of 100 ps have been observed. There are efforts to understand

the source of these time bias with speculations that the time bias might be caused by electronics or loss in PbWO_4 crystal transparency due to radiation.

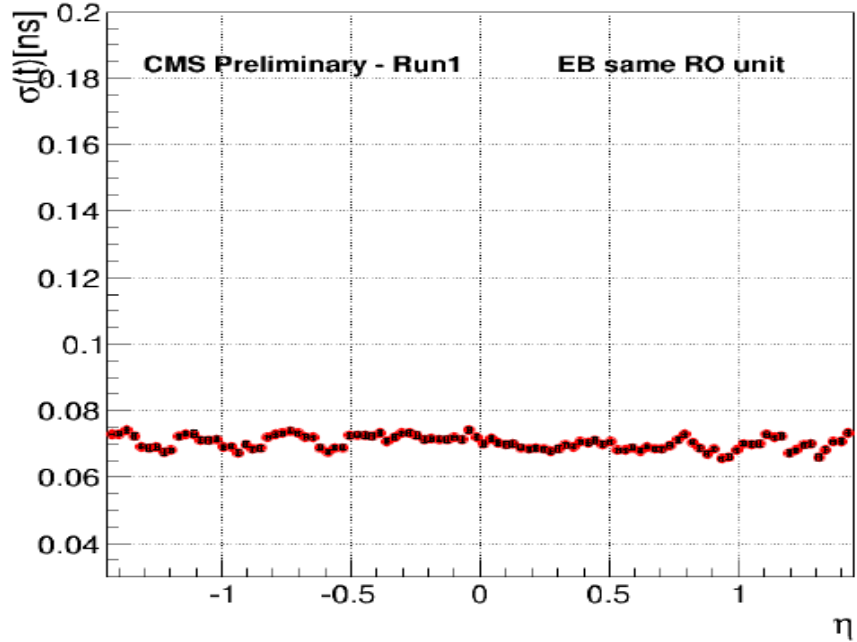


Figure 4.6: Distribution of the time standard deviation (σ) against crystal geometrical position, η , in the ECAL barrel. Almost flat distribution of σ with η .

4.4.3 ECAL Time Performance With Z Events

We evaluate the precision of ECAL time measurements during proton-proton collisions by studying the time measurement of a well understood physics process; the decay of the Z boson to an electron pair, i.e. $Z \rightarrow e^-e^+$. We use the standard deviation (time resolution), σ_{eff} , of the difference in arrival time of the two electrons to evaluate ECAL time performance. The standard deviation is obtained from the difference in the seed time, t_{seed} , of the electron electromagnetic shower of each electron after correcting for contributions from the bending of the electron travel path inside CMS magnetic field of 3.8 T. In Figure 4.7, we present the distribution of the time difference, $t_{\text{electron1}} - t_{\text{electron2}} = t_{\text{seed1}} - t_{\text{seed2}}$, of both electrons adjusted for time of flight corrections and in Figure 4.8, we show the time resolution or $\sigma_{\text{eff}}(t_1 - t_2)$, obtained from the time distribution of the seed crystal time without correcting for the bending of the electron's

flight path contributions. A time resolution of 232 ps in EB and 384 ps in EE is realized. However, if we remove the contributions from the spread in time, $\sigma(t_{\text{collision}})$, due to the finite time it takes for the two proton bunches of length 5.5 cm to collide; which is about $\sigma(t_{\text{collision}}) = \sigma(t_Z) = 183 \text{ ps}$, we obtain an improved time resolution of 142 ps in EB and 337 ps in EE. The selection for Z candidate events required that the electrons have a transverse energy bigger than 10 GeV and the reconstructed Z mass is within, $60 \text{ GeV} < m_{\text{inv}}(e_1, e_2) < 150 \text{ GeV}$ in order to ensure mostly good Z boson candidate events are used.

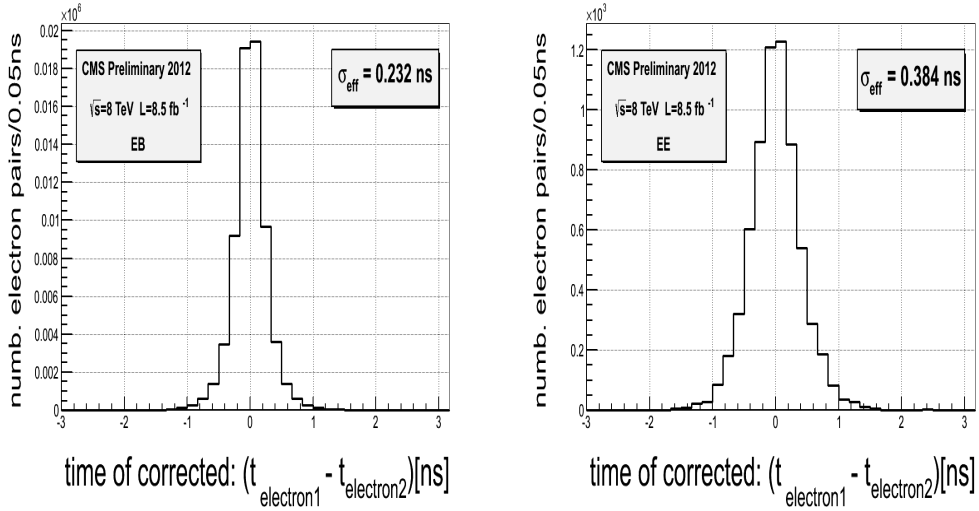


Figure 4.7: Ecal time difference between the two reconstructed electrons in $Z \rightarrow e^-e^+$ decay. The electron time is the seed (crystal with highest energy deposit) time with additional correction due to the time of flight of the electron in EB and EE

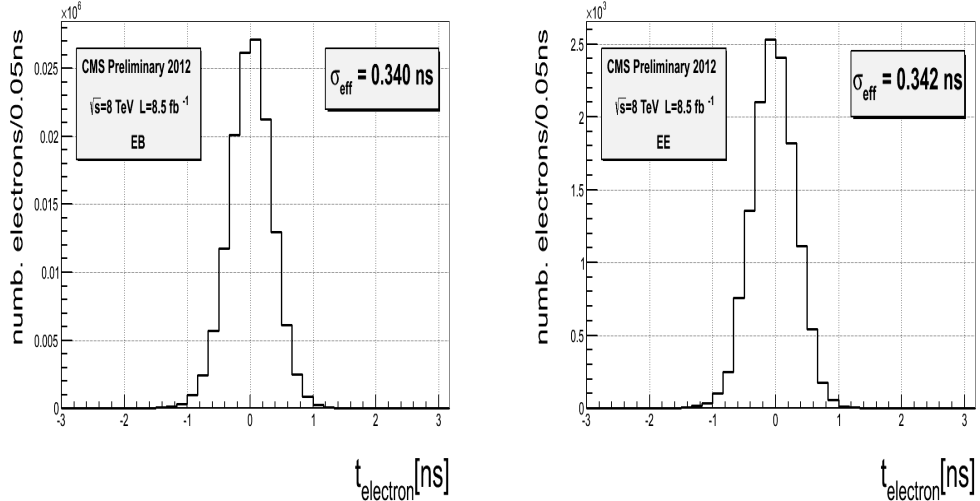


Figure 4.8: Ecal absolute time of a single reconstructed electron in $Z \rightarrow e^-e^+$ decay. The electron time is the seed (crystal with highest energy deposit) time of the electron in EB and EE

We also investigate the contributions attributed to the readout electronics on the time resolution using events with $Z \rightarrow e^-e^+$ decay. Figure 4.9(left), shows the time resolution obtained from measuring the electrons arrival time in the case where the seed crystal time of both electrons is read from the crystals belonging to same ReadOut (RO) electronics and compared to the other case where the seed crystal time is read from crystals belonging to two different readout electronics shown in Figure 4.9(right). The Constant term, C , for the same RO electronics is about 67 ps while that for different RO electronics is 130 ps indicating that electronic readout de-synchronization contributes to the worsening of the time resolution.

Despite, the observed 100 ps bias which seems to be related to readout electronics, we argue that, with a time resolution of $\sigma(t) \leq 400$ ps, the ECAL subdetector is very reliable for time measurements and can be used in the search for delayed electromagnetic particles produced in the decay of long-lived particles.

The ECAL time resolution for the entire LHC Run 1 of 2011 and 2012, comparing the absolute and single precision time measurements is summarized in table 4.1.

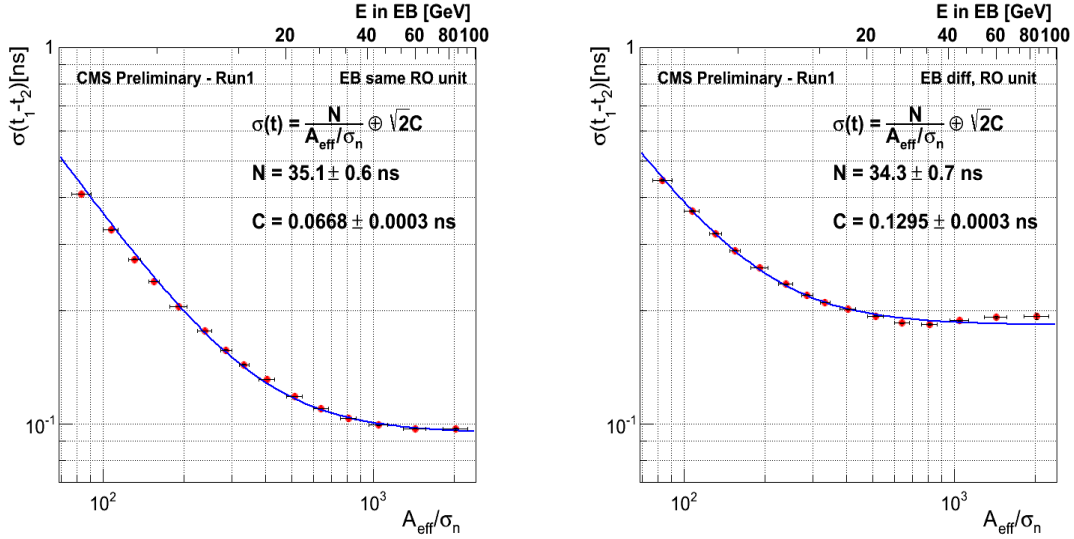


Figure 4.9: Timing resolution from: *left*: Two most energetic crystals in the same readout unit, *right*: Two most energetic crystals belonging to different readout units, as a function of effective amplitude($A_{\text{eff}} = A_1 A_2 / \sqrt{A_1^2 + A_2^2}$) normalized to noise in EB. Both crystals are from reconstructed electrons in $Z \rightarrow e^- e^+$ events.

ECAL Timing Resolution

2011	
Absolute Time	Single Precision
$\sigma_{\text{eff}}(t_{\text{seed}})[\text{ps}]$	$\sigma_{\text{eff}}(t_{e1} - t_{e2})/\sqrt{2}[\text{ps}]$
EB	376
EE	356
2012	
Absolute Time	Single Precision
$\sigma_{\text{eff}}(t_{\text{seed}})[\text{ps}]$	$\sigma_{\text{eff}}(t_{e1} - t_{e2})/\sqrt{2}[\text{ps}]$
EB	340
EE	342

Table 4.1: ECAL timing resolution absolute time and single precision for 2011 and 2012 of LHC Run 1

Chapter 5

Event Reconstruction

5.1 Event Reconstruction Overview

An event is comprise of one or more particles produced in a particular proton-proton collision. Event reconstruction is the process of constructing particles and their four momenta using raw data read from the electronics of the different CMS subdetectors. The process begins in each subdetector using a local reconstruction algorithm and eventually extends to all subdetectors. In the calorimeter subdetectors, an energy clustering algorithm is used to produced energy clusters and in the tracker and muon chambers, a combination of tracking algorithms is used to construct particle tracks. By matching selected tracks to energy clusters, particles like photons, electrons, muons, jets and missing transverse energy (E_T^{miss}) are reconstructed.

5.2 Supercluster Reconstruction

The clustering algorithm produces a cluster of clusters called *supercluster*, of the energy of an electromagnetic shower. A supercluster is either a 3×3 or 5×5 crystal energy matrix. About 94% (97%) of the incident photon or electron energy is deposited in this 3×3 (5×5) matrix of crystals in the (η, ϕ) plane in barrel or (x, y) plane in endcap. The 3.8 T magnetic field and material in front of the calorimeter causes bremsstrahlung electrons and converted photons to deposit their energy in a cluster of crystals spread in ϕ . As a result, clustering algorithms start building superclusters with

a seed crystal(crystal with the maximum energy), continue within a narrow window in η by summing the crystal energies along the ϕ which is the direction of energy spread due to the magnetic field. Figure 5.1 is schematic picture showing the direction of the clustering process in the (η, ϕ) plane in barrel and the fraction of electromagnetic energy coverage in a typical supercluster.

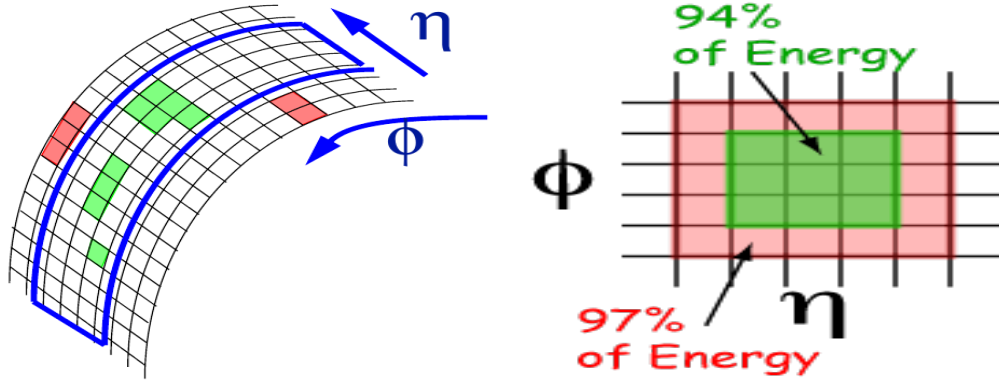


Figure 5.1: Superclustering algorithm direction in the (η, ϕ) plane in EB and fraction of electromagnetic shower energy coverage in a crystal energy matrix.

The two major clustering algorithms used in ECAL are the *hybrid* (EB) and *island* (EE) algorithms.

- **Hybrid Supercluster Algorithm:** This algorithm is used for making super clusters in the barrel (EB). It takes advantage of the $\eta - \phi$ geometry of barrel crystals by taking a fixed 3 or 5 crystals in η and dynamically search and sum separate crystals energy along ϕ . The Hybrid algorithm takes advantage of our knowledge of the lateral shower shape along the η direction. The supercluster consists of basic clusters, usually 3×3 crystals matrix.
- **Island Supercluster Algorithm:** This algorithm is used for making clusters in the endcap (EE). It begins by finding the seed crystal of the electromagnetic shower with maximum energy above a certain energy threshold. Using the seed crystal position, adjacent crystals are examined and added to a cluster until a rise in energy where a crystal belonging to another cluster or crystal that has no readout is reached. For each crystal to be added to the cluster, its energy read must be positive, it must not have been assigned to another cluster and the

previous crystal added in the same direction must have a higher energy. These non-overlapping clusters finally forms a “supercluster”.

5.3 Track and Vertex Reconstruction

Charge particle track reconstruction in CMS uses many algorithms. All these algorithms use the reconstruction positions (*hits*) during the passage of a charged particle in the silicon detectors, to determine the helix trajectories of charged tracks. These helix trajectory is used to measure the particle’s momentum and direction.

The main algorithm used for track reconstruction of proton-proton collisions is the Combinatorial Track Finder (CTF). The CTF proceeds in three stages: seeding, finding and fitting. During seeding, hits that are compatible with the interaction region above a lower p_T limit are used as possible candidates of the charge tracks. Pixel hits are the best track seeds. In the more forward region of the tracker detector, $2 < |\eta| < 2.5$, pixel and inner strips are used for better track finding. The track finding stage uses the Kalman Filter pattern recognition approach where, starting with the seeded parameters, the track trajectory is extrapolated to neighboring tracker layers and compatible hits are assigned to the track. During the fitting stage, the Kalman Filter algorithm is again applied where each candidate track is fitted using least-squares fitting in two stages. The first stage removes possible bias from the seeding stage while the next stage yields the best estimates of the track parameters at the original vertex. Other algorithms like the *iterative tracking algorithm* which is a general purpose tracking algorithms is used in association with customized CTF tracking algorithm to reconstruct the tracks of non-collisions events like cosmics and beam halo.

Similar to track reconstruction, vertex reconstruction involves two stages of vertex finding and fitting. During vertex finding, many tracks are grouped together into vertex candidates. The vertex finding algorithms used depends on whether it is finding primary or secondary vertex or the reconstruction of an exclusive particle decay. In vertex fitting, the best estimates of the vertex parameter like position, covariance matrix and track parameter constraint as well as the fit quality (chi-square, number of degrees of freedom, track weights) is used to distinguish among a given sets of tracks.

5.4 Photon and Electron Reconstruction

Photons are reconstructed from superclusters using the energy contained in a 5×5 crystals matrix surrounding the seed crystal. Since photons are neutral, photons are identified as superclusters in ECAL not associated to any tracks or reconstructed positions in the pixel tracker. To improve photon identification, several criteria are used to distinguish true photons from other particles misidentified as photons. The criteria to identify true photons consists of tracker isolation, ECAL isolation, hadron calorimeter isolation, hadronic to electromagnetic ratio and R_9 , which is the ratio of the electromagnetic energy contained in a 3×3 matrix to the supercluster energy. The R_9 variable is very useful in separating photons from the decay of π^0 with isolated photons since the photons from π^0 decay have a lower value of R_9 compared to isolated photons.

Similar to photons, electron candidates are found when a supercluster is associated to a track reconstructed in the silicon tracker detector and in particular, its inner most layers. In electron reconstruction, the seeding approach is either driven by ECAL or by the tracker. The ECAL driven seeding approach is very efficient for electrons with $p_T > 10 \text{ GeV}/c$. The track driven seeding approach uses a boosted decision tree to perform a pre-selection of the tracker clusters, in order to reduced fake electrons which are light hadrons. Isolated electrons with low p_T and non-isolated electrons (electrons embedded in jets) are reconstructed efficiently using the tracker driven seeded approach. When fitting the electron tracks, we must account for the different energy loss mechanisms of the electron compared to other charged particles. Since electrons energy loss is mainly through the non gaussian nature of its bremsstrahlung, the Gaussian Sum Filter algorithm is used to provide a good estimated the track momentum both at the ECAL surface and at the interaction point.

During proton-proton collisions, in addition to events with true photons and electrons, are events produced from low energy proton-proton collisions called *minimum biased events*, events produced from the radiation of the quarks and gluons called *underlying events*, and events from multiple proton-proton interactions called *Pile Up* (PU) events, contributing to the reconstructed photon or electron energy. Additional contributions to this energy comes from poor detector calibration, poor supercluster or track

reconstruction, faulty electronics and crystal transparency loss due to radiation. The true photon or electron energy must be adjusted for these contributions during reconstruction.

An estimate of the energy deposited by an electromagnetic particle in the ECAL, $E_{e/\gamma}$, can be approximated using Equation 5.1;

$$E_{e/\gamma} = F_{e/\gamma} \cdot [G \cdot \sum_i S_i(t) \cdot C_i \cdot A_i], \quad (5.1)$$

where A_i is the signal amplitude in ADC counts, C_i is the inter-calibration coefficient, $S_i(t)$ is the time-dependent corrections for response variable, usually obtain from laser, G is the global scale calibration allowing to go from energy in ADC counts to GeV and $F_{e/\gamma}$ is the particle energy corrections for geometric, clustering and other effects. The sum is over all the crystals belonging to the photon or electron supercluster. To obtain the true electron or photon energy, energy adjustments which depend on η through $F_{e/\gamma}$ are applied during supercluster reconstruction to account for detector energy mis-measurements caused by cracks between crystals and electronic noise. In Figure 5.2, we show comparisons between cases where no energy adjustments were made to those where energy adjustments (in the form of crystal inter-calibration and laser monitoring corrections for crystal transparency loss) have been made, through measuring the mass of the Z boson. We see improvements on measuring the Z mass, 91 GeV/cc, after the inter-calibration (IC) and laser monitoring (LM) corrections were made. Figure 5.3, shows the case where adjustments are made during supercluster reconstruction. Once again the Z mass is well reconstructed after introducing these corrections.

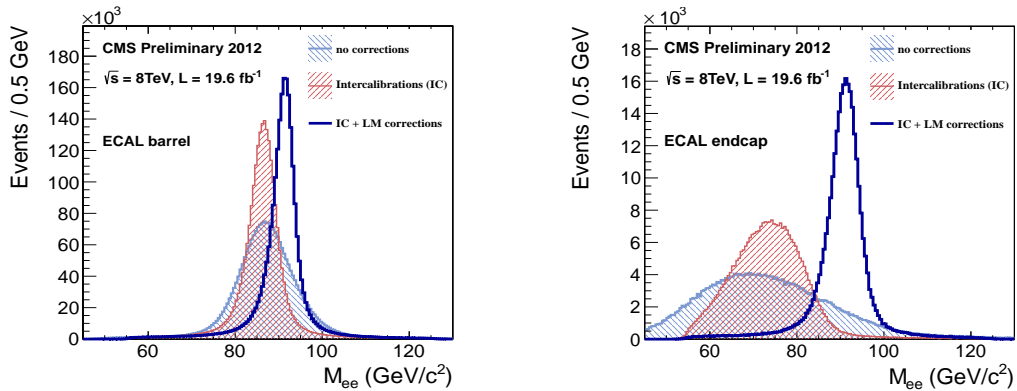


Figure 5.2: Z mass distribution from $Z \rightarrow e^+e^-$ decay showing improvement in the measurement of the Z mass after performing energy adjustments to account for intrinsic spread in crystal, photo-detector response and time-dependent corrections to compensate for channel response loss for EB (right) and EE (left)

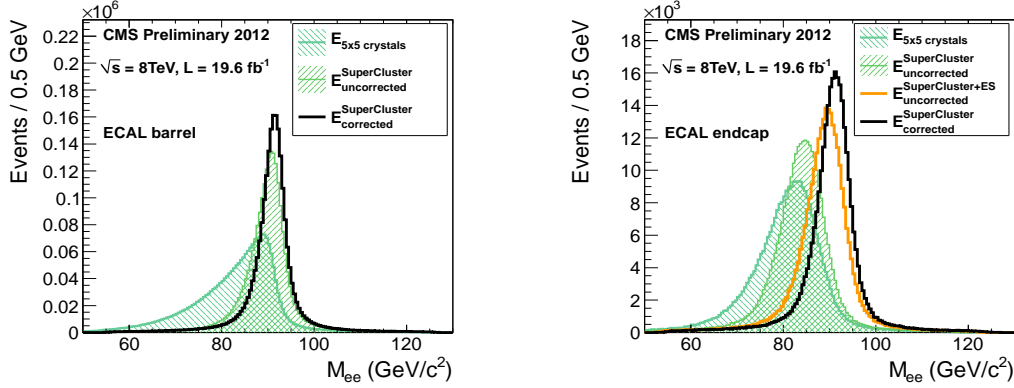


Figure 5.3: Z mass reconstructed using electron superclusters shows improvement in Z mass measurement after applying energy adjustment at superclusters for EB (right) and EE (left).

In Table 5.1, we present a summary of variables constructed using information of the spread of the electromagnetic shower in η and ϕ , the ratio of the energy deposited in HCAL to ECAL, the track p_T and ECAL E_T , isolation in ECAL, HCAL and tracker, the ratio of the energy sums over 3×3 and 5×5 matrices centered on the highest energy crystal of the seed cluster; $R_9 = E_{3 \times 3}/E_{5 \times 5}$ or $R_9 = \sum E_9 / \sum E_{\text{Supercluster}}$ and impact parameter, $d0$, which is the minimum separation of the electron track computed with respect to the reconstruction vertex and track transverse momentum, p_T . Photon and electron selection using these variables, applied during electron and photon identification, have been shown to produce very good quality electron and photon candidates with efficiency above 70%.

Simple Cut Based Electron Photon Identification

ID Variable	Electron	Photon
H/E	0.05(EB), 0.10(EE)	0.05
$ \Delta\eta_{in} $	0.005(EB), 0.007(EE)	0.015(EB)
$ \Delta\phi_{in} $	0.09(EB), 0.09(EE)	N/A
$\sigma_{i\eta i\eta}$	0.01(EB), 0.03(EE)	0.011(EB), 0.03(EE)
Pixel Veto	No	Yes
$ d0 (vertex)$	0.02(EB), 0.02(EE)	Veto
$ dZ (vertex)$	0.1(EB), 0.1(EE)	0.02 (cm)(Veto)
$ 1/E - 1/p $	0.05(EB), 0.05(EE)	N/A
PF isolation / p_T (cone dR=0.3)	0.15(EB), 0.10(EE)	N/A
ECAL Isolation	same	$4.2 + 0.006 * E_T^\gamma +$ $0.183 * \rho(\text{EB})$
HCAL Isolation	same	$2.2 + 0.0025 * E_T^\gamma +$ $0.062 * \rho$
TRACK Isolation	same	$2.0 + 0.001 * E_T^\gamma +$ $0.0167 * \rho$
Rho corrected PF photon isolation	N/A	$1.3 + 0.005 * p_T^\gamma(\text{EB})$

Table 5.1: Simple cut-based selection criteria for electron and photon identification.

5.5 Muon Reconstruction

Muon tracks are reconstructed using the all-silicon inner tracker (tracker tracks) and the muon system (standalone tracks). The standalone tracks are reconstructed using reconstructed positions (hits) in the muon system consisting of the Drift Tubes (DT) in the barrel ($|\eta| < 0.9$), Cathode Strip Chambers (CSC) in the endcaps ($1.2 < |\eta| < 2.4$) and Resistive Plate Chambers (RPC) in the overlap region ($0.9 < |\eta| < 1.2$). There are two independent muon reconstruction approaches: *Global muon reconstruction (Outside-in)* and *Tracker muon reconstruction (Inside-out)*. For Global muon reconstruction, each standalone-muon track is matched to a tracker track by comparing the parameters of

the two tracks propagated to a common surface. The global muon track is fitted combining hits from the tracker track and standalone-muon track using the Kalman-filter algorithm. For the tracker muon reconstruction, all tracks with $p_T > 0.5 \text{ GeV}/c$ and total momentum $p > 2.5 \text{ GeV}/c$ are considered as possible muon candidates and are extrapolated to the muon system taking into consideration the magnetic fields, the average expected energy loss in the calorimeters and multiple Coulomb scattering in the detector material to locally reconstruct segments in the muon system. A combination of different muon algorithms depending on the muon p_T , provides a robust and efficient muon identification.

Using the beam spot as constraint of the muon's vertex, it is possible to distinguish between muons produced from proton-proton collisions from those produced from cosmic *cosmic muons* and proton beams interacting with the gas in beam pipe and proton dump muon splash events produced 150 m upstream the CMS detector during proton beam dump. The proton beam related muons are referred to as *beam Halo muons*. Figure 5.4 show an illustration of trajectories of different muon sources interacting with the CMS detector.

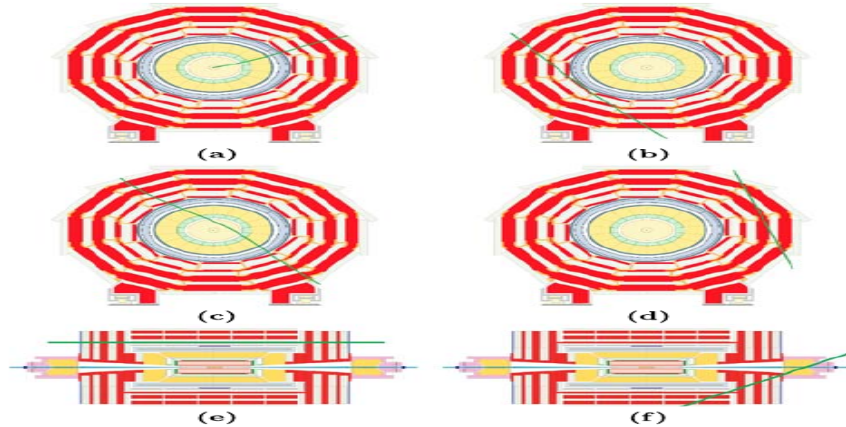


Figure 5.4: Illustration of muons from proton-proton collision, cosmic rays and beam halo. (a) Muons from collision propagating from the center and moving outwards, (b) Cosmic muons traveling through the detector leaving signals in opposite hemispheres of the muon system, (c) Cosmic muons leaving signals in the tracker and opposite hemispheres, (d) cosmic muons entering and leaving the detector without passing through the muon detector layers, (e) beam halo muons penetrating the detector and leaving signals in the endcaps and (f) Cosmic muons entering the detector through the endcap and leaving through the barrel and which can happen in a *vice-versa* manner.

Particle Flow Algorithm

The *Particle Flow* (PF) algorithm is an algorithm for reconstructing particles combining information from the tracker, ECAL, HCAL and muon chambers of the CMS detector. It uses a combination of different algorithms comprising of calorimeter clustering, tracking and extrapolation to calorimeters, muon identification, electron pre-identification and linking of topological elements, for reconstructing a list of particles which include photons, charge hadrons, neutral hadrons, muons and electrons. The same list of particles is subsequently used to reconstruct composite “particles” like jets, E_T^{miss} and taus. The versatility of the PF algorithm is the reason why it was introduced for reconstructing Jets, missing transverse energy (E_T^{miss}) where complete information of the event content from every subdetector is needed. The PF algorithm uses tracks, electron energy seeds, 4-momentum, super cluster energy calibration, bremsstrahlung tracks for electron and photon reconstruction making it extremely efficient at minimizing electron and photon misidentification. For E_T^{miss} reconstruction where full reconstruction of all the particles belonging to an event is necessary, the PF algorithm is very reliable.

5.6 Jet Reconstruction

A jet is a spray of particles arising from the hadronization of colored particles. Because jets are made of many particles like electrons, photons, hadrons, charged and neutral electromagnetic and hadronic showers, they are best reconstructed using the particle flow algorithm. Jets reconstructed using the PF algorithm are called *Particle Flow Jets*. Using calorimeter towers as input, jets can also be reconstructed using the Anti- k_T clustering algorithm which combines four vectors according to their relative transverse momentum within a standard cone size of $R = 0.5$ in the (η, ϕ) plane. The quality of a reconstructed jet depends on the jet identification selection criteria known as the *JetID*. High quality jets are required to have an electromagnetic energy fraction (EMF) > 0.01 , within the ECAL fiducial region of $|\eta| < 2.6$, the number of calorimeter cells containing more than 90% of jet energy (N_{jet}^{90}) must be > 1 , the fraction of jet energy in the hottest Hybrid photodetector (HPD) unit in HCAL readout within a jet (f_{HPD}) must be > 0.98 , the charge hadron fraction (CHF) > 0.0 if within $|\eta| < 2.4$, the neutral hadron fraction (NHF) < 1.0 , the charge electromagnetic fraction (CEF) < 1.0 , and

neutral electromagnetic fraction $z(NEF) < 1.0$. These jetId selection requirements have been shown to remove mis-reconstructed jets arising from spurious energy deposition in subdetectors with good efficiency. The jet energy is often mis-measured due to cracks in the detector, non-linear responses in the calorimeters, electronic noise, poor detector calibration and additional energy from PU. Therefore, adjusting the jet energy through *jet energy corrections* (JEC) is often performed guaranteeing a reliable measurement of the jet energy during reconstruction.

5.7 Missing Transverse Energy Reconstruction

It is very challenging to detect particles which do not interact with the detector. Such particles include very weakly interacting particles like neutrinos (ν), neutralinos ($\tilde{\chi}_1^0$) and gravitino (\tilde{G}). In CMS, the presence of this kind of particles in an event is inferred through a measurable quantity called *missing transverse energy*. Measurable quantities like transverse momentum (p_T) and cone size, $\Delta R = \sqrt{\Delta\eta^2 + \Delta\phi^2}$, are used to identify and distinguish particles traveling in the transverse plane, (x, y) or (η, ϕ) , from the longitudinal plane, along the z direction. Employing the conservation of momentum in the transverse plane, we can use the imbalance in transverse momentum required to ensure conservation of total transverse momentum of an event to infer the presence of an undetectable particle traveling in the transverse plane. The amount or quantity of this transverse momentum imbalance or missing transverse momentum is called missing transverse energy (MET) or E_T^{miss} . The presence of reconstructed E_T^{miss} in an event indicates the presence of very weakly interacting particle(s) which escape the detector undetected.

We define E_T^{miss} as the magnitude of the negative vector sum of the uncorrected transverse energy deposit of all the particles in an event.

$$E_T^{\text{miss}} = \left| - \sum_n (E_n \sin \theta_n \cos \theta_n \hat{\mathbf{i}} + E_n \sin \theta_n \sin \theta_n \hat{\mathbf{j}}) \right| = |\not{E}_T^x \hat{\mathbf{i}} + \not{E}_T^y \hat{\mathbf{j}}| \quad (5.2)$$

Where, n is the sum over all calorimeter energy deposits including energy deposits in towers, reconstructed energies (hits) or generator level particle energies. In order to measure E_T^{miss} accurately, a particle detector should be as near hemispherical as possible to

allow for complete measurement of the transverse momentum of all the particles belonging to an event. The CMS detector, provides a near hemicity with its nearly 4π solid angle coverage. This near 4π solid angle is achieved through the hadronic forward (HF) detector with little space allowing for the passage of the proton beams. Since according to conservation of momentum, the total transverse momentum before and after collision should be the same, by measuring the p_T of every detectable particle belonging to an event after proton-proton collision, the imbalance in p_T required to ensure the conservation of transverse momentum in the event, is ascribed to the momentum carried away by undetected particle(s). This idea is used to infer the presence of neutrinos W boson decay to an electron and an anti-electron neutrino; $W \rightarrow e + \bar{\nu}$, where the missing transverse momentum is used to infer the presence of the undetectable neutrino.

Since particle interactions involving supersymmetry and other beyond the standard model processes involves large E_T^{miss} due to the production of undetectable particle(s) during proton collisions, E_T^{miss} is the desirable quantity to use in many particle searches involving the possible production of new very weakly interacting particles. Standard Model particle interactions produces small E_T^{miss} . In any particle search which involves the production of new weakly interacting particle, it is imperative to accurately measure E_T^{miss} , as some standard model interaction processes like machine induced backgrounds from halo muons, mis-measured energy and mis-reconstructed particles and anomalous signals like spike can lead to large E_T^{miss} mimicking the signal for new particle(s).

5.8 Anomalous Signals

Anomalous signals are signals read from the electronics called *spikes* with abnormally large energy deposits in the avalanche photodiodes without any scintillation in the PbWO₄ crystals. They are produced when neutrons or charged hadrons like protons, strike directly ionizing the silicon of the photodiode producing an electronic signal in the absence of any crystal scintillation.

Because of no scintillation, they appear much earlier (negative) in ECAL measured arrival time and often populate the earlier time of the reconstructed hit (*rechit*) time distribution. Their energy deposit range from a few GeV to ECAL saturation energy of about 1.7 TeV. Since they do not electromagnetically shower in PbWO₄ crystals,

their electromagnetic energy shower shape is very isolated, with only one or two crystals contributing to the energy cluster. Spikes may also have positive time appearing late or delayed in their arrival time at ECAL populating the tails of the rechit time distribution. The late arrival time is due to the slow propagation of neutrons through the CMS detector.

Numerous test beam, collision data and simulation studies,[42], have been carried out towards understanding the properties of events with spikes and how they can be tagged and removed. These studies, reveal that spikes can be identified and removed using a topological energy variable constructed as $1 - \frac{E_4}{E_1}$ known as the “*Swiss-Cross*” (SX). E_1 is the energy deposit of the central (highest energy) crystal and E_4 is the sum total of the energy of the neighboring four crystals in an (η, ϕ) plane. A selection cut in $\text{SX} > 0.95$ rejects more than 99% of isolated spikes with transverse energy greater than 10 GeV with very little impact on the efficiency of selecting electromagnetic EM showers. Other topological variables like $1 - \frac{E_2}{E_6}$ and $1 - \frac{E_2}{E_9}$, where E_2 is the sum of the energy of two crystals sharing the energy deposited and $E_6(E_9)$ is the sum of the neighboring 6(pairs-of)(9) crystals in the (η, ϕ) plane are used. The $1 - \frac{E_2}{E_6}$ variable is used to identify isolated spikes whose energy deposit spread in two adjacent crystals while the $1 - \frac{E_2}{E_9}$ is used to identify non-isolated spikes i.e. spikes which are found embedded in a supercluster. It has also been shown that applying selection cuts on the rechit time of ± 3 ns leads to more than 90% efficiency for rejecting spikes. However, in this thesis, we do not require such selection cuts on the rechit time as these rechits include rechits of possible delayed electromagnetic particles with arrival time beyond 3 ns produced during proton-proton collisions.

Chapter 6

Search Analysis for Long-Lived Particles

6.1 Analysis Strategy

Our analysis approach is counting the number of events with large missing transverse energy (E_T^{miss}) and isolated high transverse momentum (p_T) delayed photon(s) produced in the decay of an electrically neutral long-lived particle and also satisfying some jet multiplicity selection criteria over an expected number of SM events. The arrival time of the photon measured using the electromagnetic calorimeter detector is used as the main search quantity.

A number of models beyond the SM, in particular, supersymmetry (SUSY) with gauge-mediated SUSY breaking (GMSB) predict the existence of a new, heavy neutral particle with a long lifetime which can decay into a photon and an invincible particle. In order to search for such a long-lived particle, we use as a reference signal model, a benchmark GMSB scenario described as “Snowmass Points and Slope 8” (SPS8) in which the lightest neutralino ($\tilde{\chi}_1^0$) is the next-to-lightest supersymmetric particle (NLSP). The neutralino is a long-lived electrically neutral particle produced from the cascade decay of other new heavier supersymmetric particles like gluinos and squarks. The $\tilde{\chi}_1^0$ decays to a photon and a gravitino (\tilde{G}) which is the lightest supersymmetric particle (LSP), $\tilde{\chi}_1^0 \rightarrow \gamma + \tilde{G}$. The gravitino being stable and electrically neutral, is very weakly interacting with detector material and leaves the detector undetected as an invincible particle.

As a result, the gravitino's presence is indirectly inferred through apparent momentum imbalance in the transverse plane or missing transverse momentum (E_T^{miss}). The photon, because of the finite lifetime of the neutralino, arrives late at the electromagnetic calorimeter compared to photons produced in SM physics processes.

Because the neutralino is produced from the decay of a heavy gluino or squark, in addition to the late photon and E_T^{miss} , high transverse momentum jets also belong to the event with $\tilde{\chi}_1^0$ decay. Therefore, the final products of an event with a neutralino decay must include high p_T isolated delayed photon(s), large E_T^{miss} and high p_T jets.

Non-collision events with photons from cosmic, *beam halo* muons and *spikes* can also have large ECAL time measurements. pp collision events with W, Z, multiple jets and $\gamma + \text{jet(s)}$ where the electron or jet is misidentified as a photon and its arrival time mismeasured, can also give rise to large ECAL time photons. And if these events happen to have E_T^{miss} due to finite detector resolution(i.e. instrumental E_T^{miss}), it is possible for them to be misidentified as the decay of a long-lived neutral particle. We refer to these kinds of events as background events.

To estimate the background contamination to signal, we use a data driven approach where we divide our data sample using ECAL time, jet multiplicity and E_T^{miss} into different control regions (CRs). After rejecting events with spikes, cosmic and beam halo muons, we employ an ABCD background estimation method to estimate background events contributing to the signal region.

Signal and Background Events

The final state of signal events of the decay $\tilde{\chi}_1^0 \rightarrow \gamma + \tilde{G}$, produced from pp collisions must have

- at least one high p_T isolated delayed photon,
- a number of large p_T jets,
- large missing transverse momentum or E_T^{miss} ,

Background events with similar final state may arise from any of these categories:

- multi-jets QCD events,

- inclusive $Z+jets$, $W+jets$ events,
- inclusive $t\bar{t}+jets$ events,
- inclusive ZZ , WW , $WZ + jets$ events,
- Spikes and non-collision events like cosmic and beam halo muons.

6.1.1 Signal Modeling

Simulated signal event samples are produced according to the SPS8 model starting with the production of *SUSY Les Houches Accord* (SLHA) files using a SUSY software package called **ISASUSY**, [56]. The SLHA files contain the the masses, interaction couplings, decay widths, all possible decay channels and branching ratio of every supersymmetric particles. It also contains the fundamental GMSB model parameters

$$\{\Lambda, M_{mess}, N_5, \tan(\beta), sgn(\mu), C_{grav}\} \quad (6.1)$$

used for scanning the model phase space. In the SPS8 benchmark model, the choice of parameters is as follows:

$$sgn(\mu) = 1, \tan(\beta) = 15, N_5 = 1, M_{mess} = 2\Lambda. \quad (6.2)$$

C_{grav} and Λ are the free parameters used to vary, respectively, the life time and mass of the neutralino in order for us to exploit different phase space of the long-lived neutralino. A special software package called **HDECAY** is used to handle the decay of all supersymmetric particles including the decay of neutralino to photon and gravitino.

Using the SLHA files as input, we generate using a software package called **PYTHIA** (a Monte-Carlo high-energy-physics event generator),[57], the productions of supersymmetric particles from pp collisions at center of mass energy, $\sqrt{S} = 8$ TeV. The interaction of the supersymmetric particles with the CMS detector is simulated using the **GEANT4** particle detector simulation software package,[58]. Full event reconstruction from hits in the detector is archived using the CMS event reconstruction software (cmssw). For consistency we use the same cmssw software release version, **CMSSW_5_3_29**, which has the same detector conditions used during data reconstruction.

The physics process for producing and decay of neutralino to photon and gravitino which we studied at the LHC pp collisions is

$$p + p \rightarrow \tilde{g}\tilde{g}, \tilde{q}\tilde{q} \rightarrow [1 \text{ or } 2 \text{ cascade decays}] \rightarrow 2\tilde{\chi}_1^0 + \text{jets} \rightarrow 2\gamma + 2\tilde{G} + \text{jets} \quad (6.3)$$

The decay of the neutralino includes decay into γ , Z bosons, *Higgs* and e^+e^- and the gravitino with the decay of the neutralino to photon and gravitino being dominant. About 83 to 94% of the neutralino decay is to a $\gamma + \tilde{G}$ and we checked that 97 to 99% of all the simulated events produced contain at least a single photon.

6.1.2 Background Modeling

We also produce Monte Carlo (MC) samples of $\gamma+\text{jet(s)}$ events with high p_T photons produced from pp interactions. The events are generated and simulated at leading order cross-sections using PYTHIA6 and GEANT4 and reconstructed using the same CMSSW release for signal. The $\gamma+\text{jet(s)}$ MC sample is used to study MC ECAL time and to perform any needed time adjustment needed to align the time from simulated events with Data.

We do not produce any MC samples for background events with W , Z and $t\bar{t}$ decays. Although these events usually have E_T^{miss} and jets with a possible large time photon in the case where a jet misidentified as a photon with a mismeasured ECAL time. The reason is because simulations of photon time in the tails of the photon time distribution is not very reliable and contributions from such background events is small as there are very few cases of these events with large photon time. In addition, our requirement of mostly high p_T isolated photons reduces their contribution to negligible. The same argument is made for events with spikes, cosmic and beam halo muons, hence, we also do not produce any MC event sample for them.

6.1.3 Datasets

The data sample used in our analysis was produced during proton-proton collisions of LHC Run 1 in 2012 with the center of mass energy, $\sqrt{S} = 8$ TeV. The CMS detector recorded data equivalent to total integrated luminosity of 19.1 fb^{-1} .

Data

Mostly single photon triggered events with *good* luminosity section certified data samples have been used. In Table 6.1 we present these data samples with their corresponding integrated luminosity. The *json* file with the list of certified good luminosity sections is **Cert_8TeV_PromptReco_Collisions12_JSON.txt**.

Dataset	Recorded Luminosity [fb ⁻¹]
/Run2012B/SinglePhoton/EXODisplacedPhoton-PromptSkim-v3	5.1
/Run2012C/SinglePhoton/EXODisplacedPhoton-PromptSkim-v3	6.9
/Run2012D/SinglePhoton/EXODisplacedPhoton-PromptSkim-v3	7.1
/SingleElectron/Run2012A-22Jan2013-v1/AOD	5.2
/DoubleElectron/Run2012C-22Jan2013-v1/AOD	4.8

Table 6.1: Data samples and the corresponding integrated luminosity totaling 19.1 fb⁻¹ used in the our delayed photons search analysis

Monte Carlo Samples

The MC samples were produced using the *Summer 2012* prescriptions on the calibration and alignment conditions of the CMS detector and pile up (PU) conditions at 8 TeV. The γ +jets MC samples contain events generated at leading order (LO) cross-section for different p_T ranges normalized to the 19.1 fb⁻¹ integrated luminosity. Table 6.3 show cross-sections, p_T range and the number of events.

The GMSB SPS8 signal samples contain 50,000 events each for the scanned lifetime and mass or SUSY breaking scale of the lightest neutralino. These samples cover lightest neutralino lifetimes, $c\tau_{\tilde{\chi}_1^0}$, from 25 to 1000 cm for each Λ_m or lightest neutralino mass ($m_{\tilde{\chi}_1^0}$) point. The SUSY breaking scale, Λ_m , range from 100 to 300 TeV which is equivalent to the lightest neutralino mass, $m_{\tilde{\chi}_1^0}$, ranging from 139 to 430 GeV/c². These samples are presented in table 6.2. The cross-section and neutralino decay to photon and gravitino branching ratio are also presented.

Λ [TeV]	$c\tau$ (mm)	σ_{LO} (pb)	Number of Events	Branching Ratio
100	250-12,000	0.368	50,000	0.9444
120	250-12,000	0.133	50,000	0.9042
140	250-12,000	0.0574	50,000	0.8711
160	250-12,000	0.0277	50,000	0.8464
180	250-12,000	0.0145	50,000	0.8282
220	250-12,000	0.0044	50,000	0.8282
260	250-12,000	0.0015	50,000	0.8282
300	250-12,000	0.0008	50,000	0.8282

Table 6.2: The signal GMSB SPS8 MC samples for difference Λ and Branching Ratios used in this analysis

\hat{p}_T	σ_{LO} (pb)	Number of Events
50 ~ 80	3322.3	1995062
80 ~ 120	558.3	1992627
120 ~ 170	108.0	2000043
170 ~ 300	30.1	2000069
300 ~ 470	2.1	2000130
470 ~ 800	0.212	1975231

Table 6.3: The $\gamma +$ jets samples used in this analysis

We perform a quick check on the validity of the GMSB signal samples by looking at the number of photons, the E_T^{miss} distribution and number of jets in each event. The plots of these quantities at generation level are shown in Figure 6.5. At least single photon events are observed confirming our expectation that indeed most of the neutralinos decayed to a photon and gravitino.

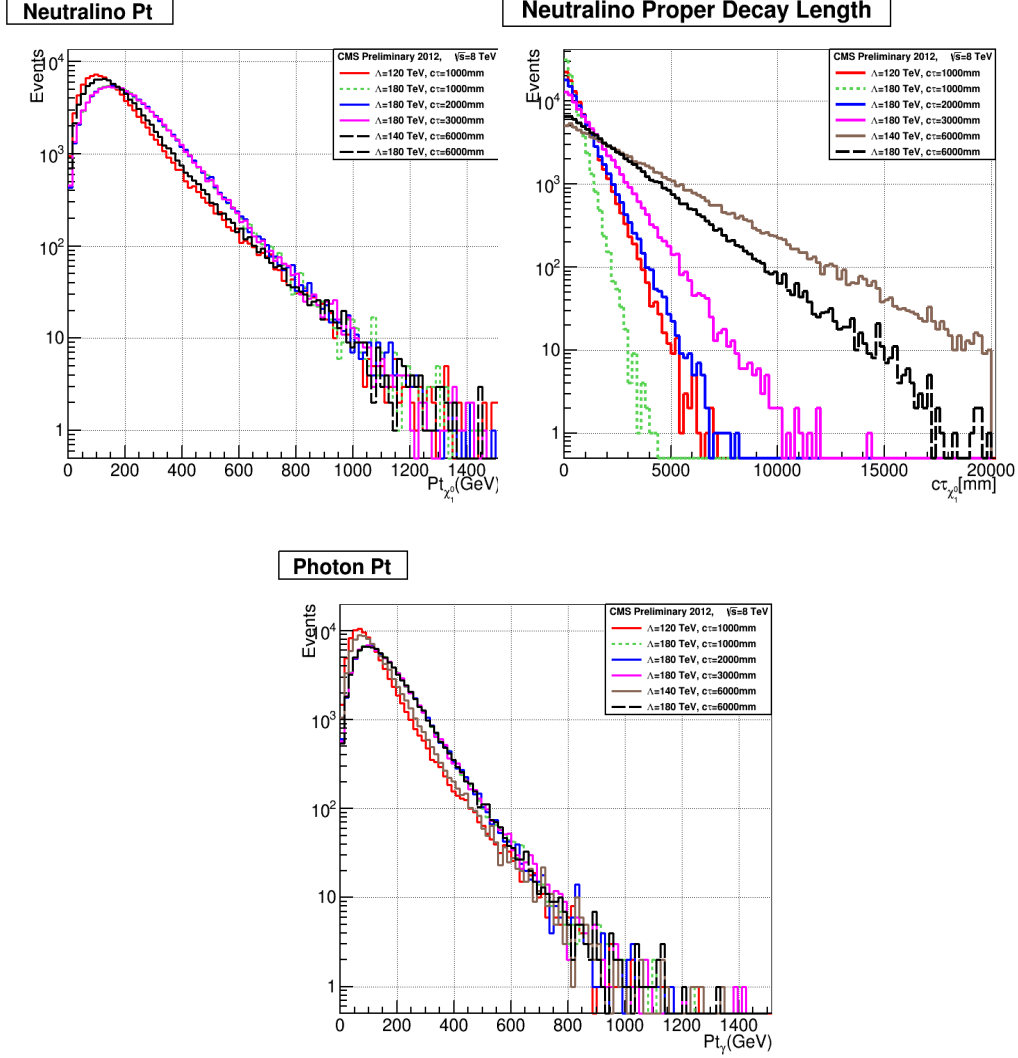


Figure 6.1: Number of photons (top left), E_T^{miss} (top right) and Number of jets (below) in neutralino decay to photon and gravitino events for different SPS8 model parameters.

6.1.4 ECAL Time

The photon arrival time at ECAL is our main observable for distinguishing background from signal. However, the presence of spikes, noisy crystals and pile-up events, require robust time measuring methods in order to minimize time bias from such events. We employ different methods to measure the photon time using ECAL.

Since the electromagnetic shower of the electromagnetic particle normally spreads across several crystals (meaning measurements from several channels are involved), a cluster of about 25 crystals (or *supercluster*) after reconstruction contains all of the particle's energy. As a result the arrival time of an electromagnetic particle is defined either using the reconstructed time (t_{reco}) of a single channel, which is usually the crystal with the highest energy (*seed crystal*), or an error (σ) weighted average of all the individual reconstructed times of each crystal belonging to the supercluster. A supercluster can be made of many smaller clusters called *basic clusters*, and the seed basic cluster (cluster with highest energy) time can equally be used as the particle's measured arrival time. We write t_{seed} for the seed time and t_{Ave} for the average time defined in Equation 6.4.

$$t_{Ave} = \frac{\sum_{i=1}^N \frac{t_{reco,i}}{\sigma_i^2}}{\sum_{i=1}^N \frac{1}{\sigma_i^2}}, \quad (6.4)$$

Where N is the number of crystals of the supercluster, $t_{reco,i}$ and σ_i are the time and uncertainty on the reconstructed time of each channel, respectively. Figure 6.2 shows a comparison of the ECAL time of a photon measured with the seed time, t_{seed} , and the average time, t_{Ave} . Both plots have been normalized to one.

The spread in both time distributions, σ of a Gaussian fit are very similar. A value of $\sigma = 345$ ps is observed for seed time compared to $\sigma = 3360$ ps for the average time distributions. Based on these observations, we decided to use the seed time as the photon ECAL time since there is not much to gain from either methods other than less computation time with the seed time method than with the average time method.

A χ^2 calculated from the time measurement of all the crystals belonging to the photon supercluster is a useful quantity to legitimized a photon time and we use it to distinguish fake photons (jets misidentified as photons) and especially spikes from true isolated photons. Figure 6.3 shows the profile of the pulse shape (left) of an identified spike with that of a true photon event. A distribution of the normalized χ^2 against the ECAL time is shown in the right plot of the same figure. Most of the photons have ECAL time around zero but many of the photons with large ECAL time have large normalized χ^2 values which is expected when the time measurements by non-seeded crystals is inconsistent with the time measurement of the seed crystal. We observed that, with a

cut in $\chi^2 < 4$, we can reduce with 99.2% efficiency, photons arrival time distribution arising from spikes and misidentified photon events.

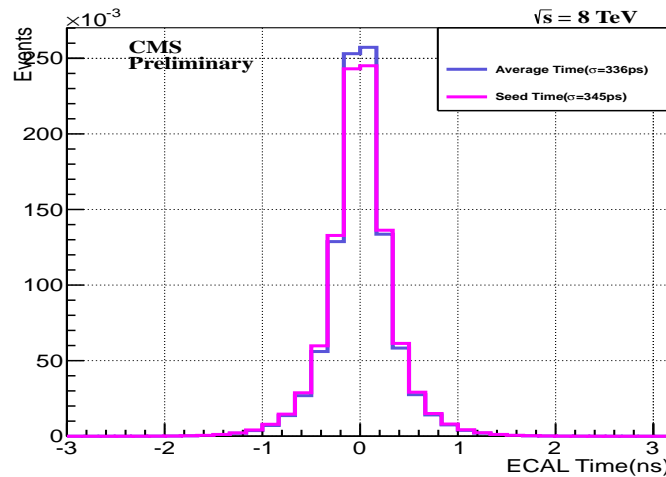


Figure 6.2: Measuring the photon time using either seed time (black) or average time (blue). σ of the Gaussian fit from seed time slightly better average time which is computationally intensive.

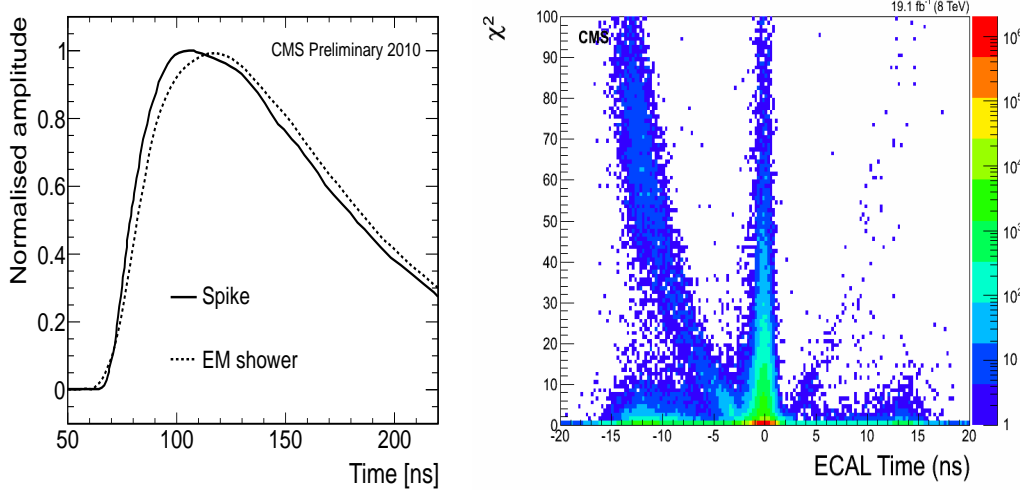


Figure 6.3: Pulse shape profile(left) showing a spike (solid line) and a true EM shower (dashed line) from data. The χ^2 against ECAL time distribution(right) shows spikes misidentified as photons with very large χ^2 with earlier arrival time. The region of $\chi^2 > 4$ is mostly dominated by spikes events.

Simulated ECAL Time

The ECAL time for photons from the decay of long-lived neutral particles anomalous events like spikes and noisy crystal channel present during data taking is not well simulated. Infact, simulating the tails of the ECAL time distribution is very challenging yet most of the events in the tails are populated by spikes, beam halo, cosmics and possible photons from long-lived neutral particle decay. We adjust for any data and MC time measurement differences using $\gamma + jets$ event samples and used mainly in-time events (photon time within a $[-2, 2]$ ns window. By selecting in-time events with only one or two jets in data, we find the difference in the peak of the photon time distribution from data to the reconstructed MC time (t_{reco}^{MC}) of photons from the $\gamma + jets$ samples. The measured time difference of the mean time between the data and MC $\gamma + jet$ sample, is used to smear the reconstructed MC ECAL time. A mean time difference of about 125 ps is observed between the data and MC ECAL time. After the smearing, both data and MC ECAL time show a close agreement for the photon arrival average time. The photon from data and MC ECAL time are shown in Figure 6.4 comparing before(left plot) and after(right plot) the smearing or MC ECAL time adjustment was

made. We performed the same smearing for all MC samples used in our analysis.

It is worth noting that the difference of 125 ps between t_{reco}^{MC} and t_{reco}^{DATA} compared to 500 ps ECAL timing resolution is not enough to influence event selection, however simulating photons ECAL time in the tails of the time distribution still remains.

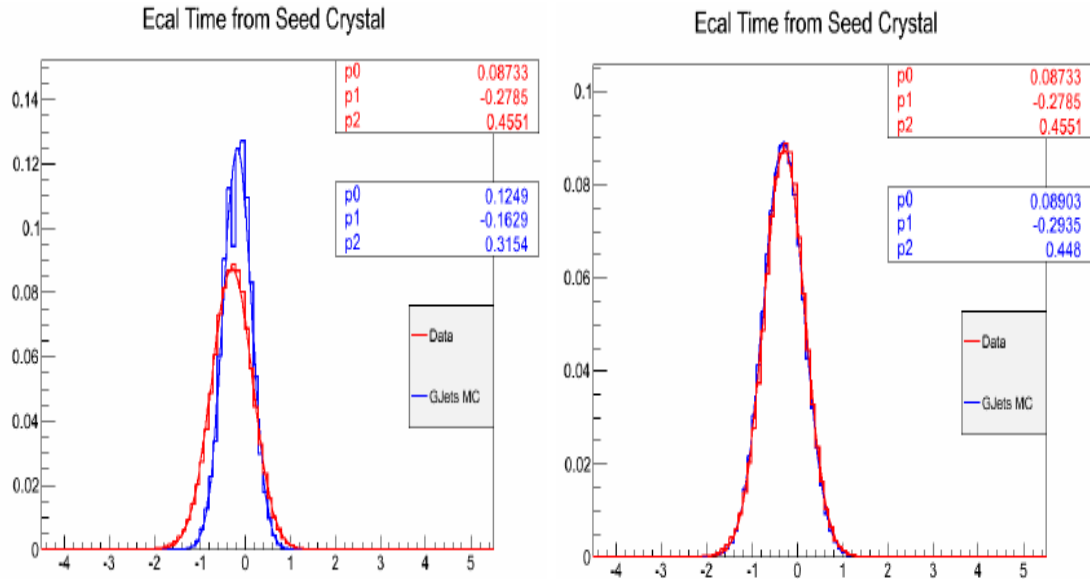


Figure 6.4: ECAL time distributions of in-time photons from MC $\gamma +$ jets (blue) and data (red) samples before (left) and after (right) we adjusted the photon time from MC.

Neutralino Measured Lifetime

The distance traveled in the transverse ($x - y$) plane in the CMS detector by the neutralino before it decays is as previously mentioned in the subsection 2.3.2, is given as

$$L = \left(c\tau_{\tilde{\chi}_1^0} \right) \cdot (\gamma\beta_T) = \left(c\tau_{\tilde{\chi}_1^0} \right) \cdot \left(\frac{p_T}{m_{\tilde{\chi}_1^0}} \right) \quad (6.5)$$

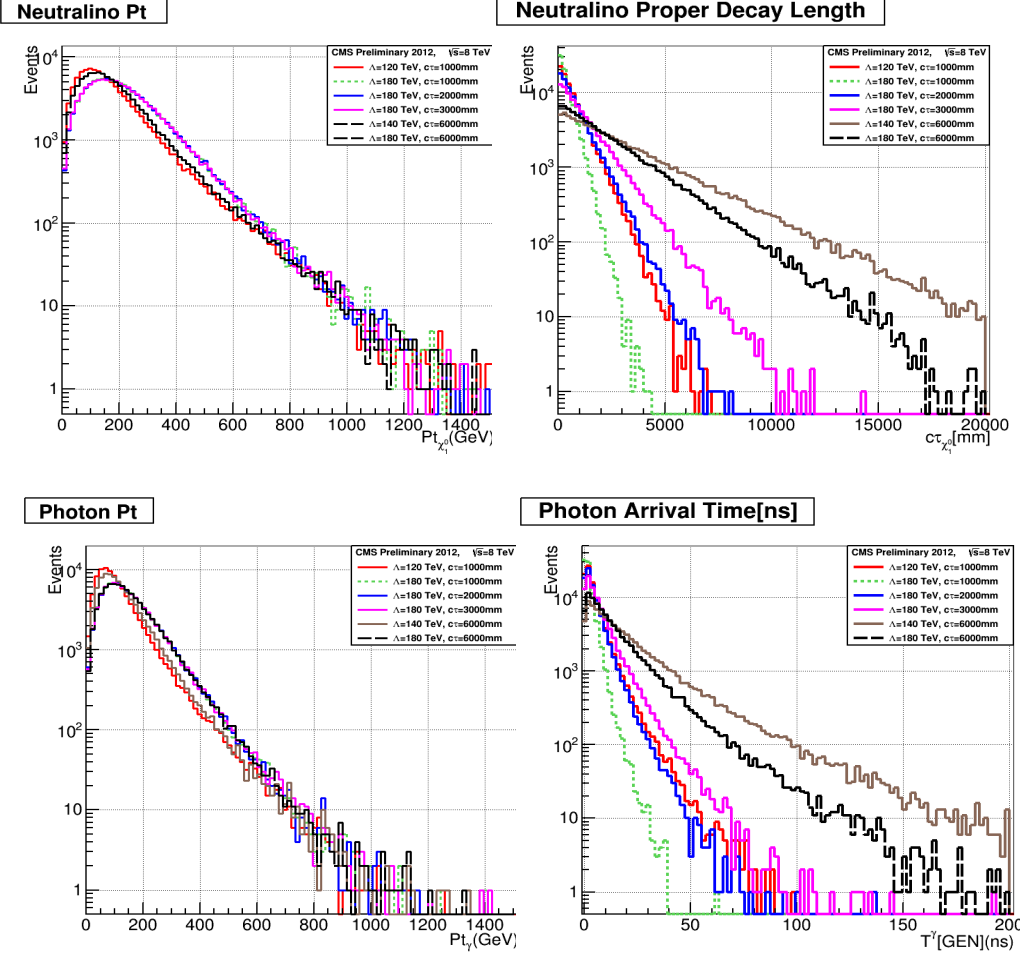


Figure 6.5: Neutralino transverse momentum distribution (top left) and proper decay length (top right) with its decayed photon transverse momentum distribution (bottom left) and time of arrival at ECAL (Bottom right) for GMSB SPS8 model.

The distance traveled by the neutralino is determined by its p_T and mean lifetime ($c\tau_{\chi_1^0}$). In Figure 6.5, we show distributions of the p_T of the neutralino ($p_T^{\tilde{\chi}_1^0}$), its measured lifetime ($c\tau_{\tilde{\chi}_1^0}$), transverse momentum of the photon (p_T^γ) and the measured arrival time of the photon (T_γ) at generation level for different Λ and $c\tau_{\tilde{\chi}_1^0}$ points. As a cross check that the signal samples have been generated with the true neutralino lifetime, we do a fit analysis to the distribution of the transverse distance traveled by neutralino before

decay and extract the value for $c\tau_{\tilde{\chi}_1^0}$. By comparing the measured value of $c\tau_{\tilde{\chi}_1^0}$ to the expected value from theoretical prediction supposedly used in the event generation, we verified that each signal sample has been properly generated with the correct neutralino decay properties.

Source of Delayed Photons

A photon from the decay of neutralino arrives at ECAL with a large time either because the neutralino is traveling slow i.e. $\beta \ll 1$, or because the neutralino was produced with a significant forward boost such that the photon arrived at ECAL through a non-direct travel flight path. To separate these two sources of delayed photons, we estimate the photon arrival time at ECAL using the neutralino and photon kinematics. Figure 6.6(left) is a schematic diagram showing how we estimate the photon arrival time at ECAL for each of the possible different sources. The estimated photon arrival ECAL time is given as follows:

- From slow moving neutralinos: $\Delta t_1 = (L_1/c\beta) - (L_1/c)$
- From non-direct traveled flight path: $\Delta t_2 = (L_1 + L_2 - L_3)/c$
- ECAL measured time = $\Delta t_1 + \Delta t_2$

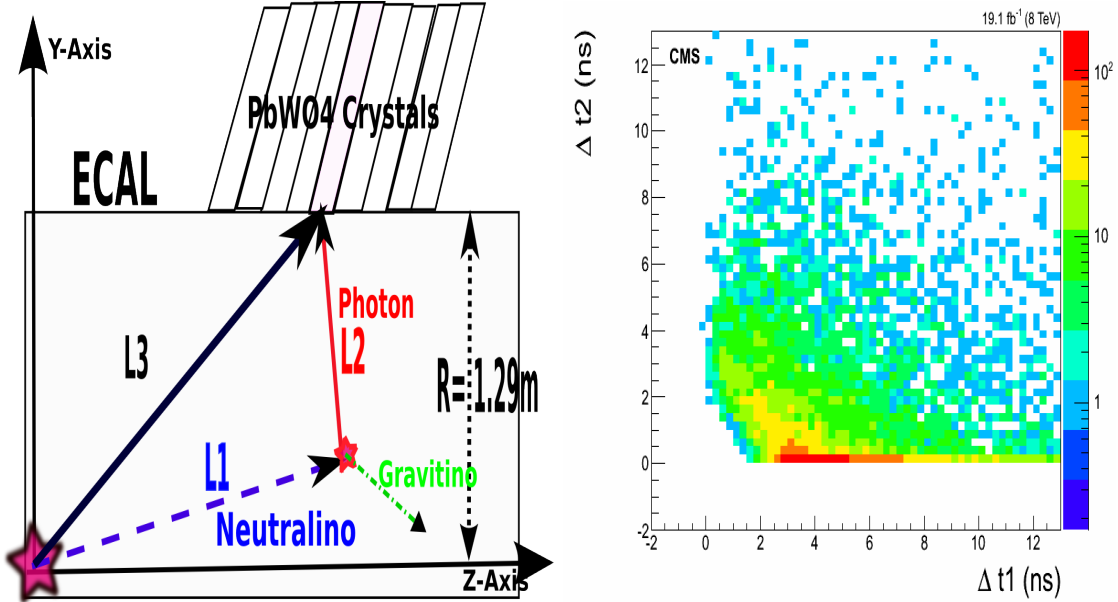


Figure 6.6: Schematic diagram showing $\tilde{\chi}_1^0 \rightarrow \gamma + \tilde{G}$ decay topology within the ECAL volume of the CMS detector (Left). Estimated photon arrival time at ECAL from the decay of neutralinos in the SPS8 model with $m_{\tilde{\chi}_1^0} = 256 \text{ GeV}/c^2$ and $c\tau = 6 \text{ m}$ (Right).

The distribution of the estimated times Δt_1 and Δt_2 plot in Figure 6.6(right) shows that most of the late arrival time photons are from the decay of slow moving neutralinos compared to those arriving late because of their non-direct flight path to ECAL. This proves that a good number of neutralinos produced with low p_T such that the ratio $\frac{p_T}{m_{\tilde{\chi}_1^0}} \ll 1$ are very detectable using ECAL time measurements while those with very long lifetimes produced with high p_T will very likely escape the ECAL undetected since they did not decay inside the ECAL volume.

Satellite Bunch Time

An ECAL time distribution for photons with $p_T > 50 \text{ GeV}/c$ arriving in the barrel and endcap sections,i.e. $|\eta_\gamma| < 3.0$, of ECAL show(see figure 6.7) a 2.5 ns discrete pattern in

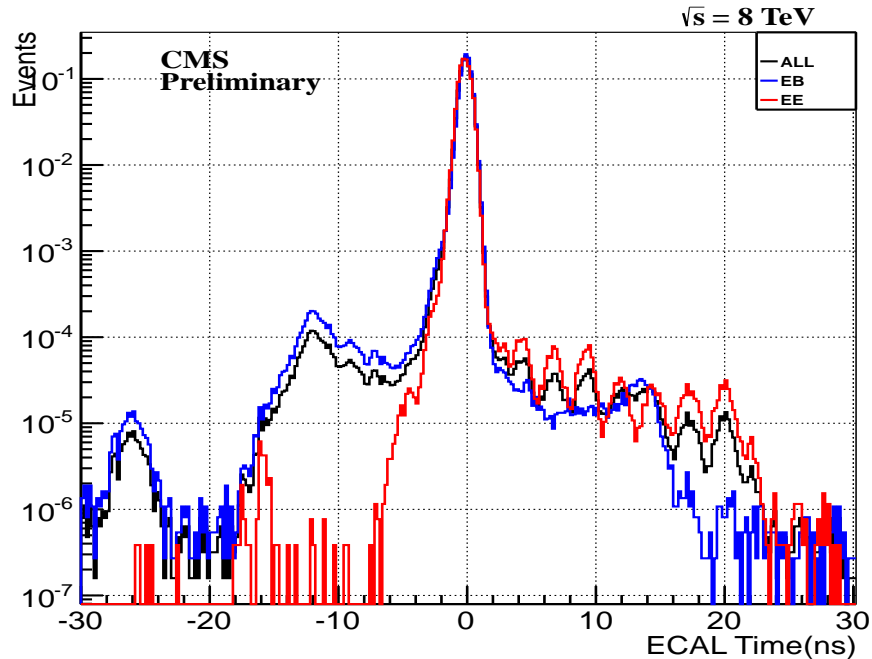


Figure 6.7: ECAL timing distribution of photons in barrel (EB), endcap (EE) and all of ECAL (ALL ECAL) with $p_T > 50$ GeV from data. A 2.5 ns delay timing structure is observed in endcaps.

the photon measured arrival time. Mostly endcap photons with $1.47 < \eta < 3.0$ show this signature compared to barrel photons; $|\eta| < 1.47$. Photons with this signature are those produced from proton collisions between *Ghost/Satellite* bunches with either the main proton collision bunch or other *Ghost/Satellite* bunches. Photons from these collisions contribute an irreducible amount as background to the photon ECAL time distribution making it very challenging to reject or estimate their contribution quantitatively. We estimate this contribution using the ratio of the protons population in the filling profile of ghost to main proton bunches in the LHC RF cavities. We described earlier in section 3.1.4 what are ghost/satellite bunches. This ratio reveals that one in every 10,000 photons from proton bunch collision is produced from ghosts bunches and most of these photons from ghost bunches are in the endcaps, since very few these photons

are produced with high enough p_T to arrive at the barrel. This observation and the fact that ECAL time resolution in the endcap is relatively poor compared to the barrel, gives us enough reason to not use the endcaps in our analysis. To further confirm the 10^{-5} reduction factor of the contribution of photons from ghost collisions in barrel, we use events with $Z \rightarrow e^+e^-$ since these events do not require high p_T . If there are electron candidates produced from ghost/satellite collisions, the electron arrival time in barrel distribution should capture the 2.5 ns time signature pattern. We study electron candidates with time within [-2.0, 2.0] ns window. Full details and the results obtained is discussed in background estimation section of this thesis.

E_T^{miss} Adjustments

The official CMS electromagnetic supercluster reconstruction criteria used in the PF event reconstruction algorithm does not include “out-of-time” energy deposits in ECAL. The purpose is to avoid energy deposits not produced from the main proton-proton bunch collisions like machine induced backgrounds. As a result, the photon E_T contribution from events with out-of-time photons is not included in the calculation of the event missing transverse energy or \cancel{E}_T (from now on, we will be using for convenience, \cancel{E}_T instead of E_T^{miss} as the symbol for missing transverse energy). This non-inclusion of the out-of-time photon E_T , introduces some difference in the calculation of \cancel{E}_T between in-time ($|t_\gamma| < 3.0$ ns) and out-of-time photon events.

In our analysis, energy deposits from events with out-of-time photons belong to possible signal events since we are searching for large arrival time photons. Because the out-of-time photon’s transverse energy (E_T) is not included in the sum total transverse momentum for events with out-of-time photons in calculating the total transverse momentum imbalance, we correct for this by subtracting the out-of-time photon’s E_T vector from the particle flow reconstructed \cancel{E}_T (PF-MET) vector. In order to avoid any bias in our event selection, particularly for events with out-of-time photons, we used an additional missing transverse energy variable defined as $\cancel{E}'_T = \cancel{E}_T - E_T$ in our final event selection.

6.2 Event Selection

Pair produced neutralinos from the decay of gluino or squarks allows for at least a photon, jets and large \cancel{E}_T to make up ours signal events with neutralino decay, $\tilde{\chi}_1^0 \rightarrow \gamma + \tilde{G}$. As a result, we select events with the required photon arrival time, number of jets(jet multiplicity) and \cancel{E}_T . A cut in \cancel{E}_T is particular useful in eliminating $\gamma +$ jets and QCD events with \cancel{E}_T arising from finite missing transverse energy resolution or poor instrumentation also known as *fake \cancel{E}_T* . Event selection in jet multiplicity helps reduces background events not produced from the nominal proton-proton collisions like cosmic muons and machine induced events like beam halo muons and spikes. These events usually produce out-of-time photons.

Another possible background events are events with the decay of $W \rightarrow e + \nu$ and $t\bar{t}$, where the top (t) decays to a b quark and a W 100% of the time. We call these background events ElectroWeak (EWK) events. These events also have fake photons(misidentified electrons as a photon) with real \cancel{E}_T arising from the presence of the neutrinos (ν). A cut in the photon p_T since we require high p_T photons and our multijet requirement of these events easily reduces this background.

To reduce an equally good source of fake photons arising from multijets QCD events, where a jet is misidentified as photons, is reduced by requiring that the jets have very high p_T and are isolated Since jets from multijet QCD events are not always isolated. To reduce events from spikes and equally other fake photon events passing our required event selections, we only accept photons with ECAL time between $3 < t_\gamma < 13$ ns as our signal acceptance region. And to reduce background contributions from ghost/satellite bunch collisions, we only select photons in the barrel ($|\eta_\gamma| < 1.479$) region of ECAL.

6.2.1 Trigger Selection

Our pre-event selection begins at the online where we select only events passing our online higher level trigger (HLT). The HLT trigger used for our $\sqrt{S} = 8$ TeV proton-proton collision analysis is the `HLT_DisplacedPhoton65_CaloIdVL_IsoL_PFMET25` seeded by `HLT_L1SingleEG12` level 1 trigger. This trigger was developed primarily for the study of delayed photons. To avoid bias in event selection towards any particular model, this trigger only requires that an accepted event contains an isolated photon with a p_T threshold

of $65 \text{ GeV}/c$ and \cancel{E}_T above 25 GeV . The minor axis of the photon electromagnetic shower must not be spread across many crystals in ϕ , $0.1 < S_{\text{Minor}} < 0.4$. The trigger efficiency and turn-on curve (efficiency becomes close to 100%) for selecting events with delayed photon candidates is done in photon p_T and \cancel{E}_T selection variables. In order to avoid any correlation between the photon and \cancel{E}_T variables, the efficiency for each variable is studied separately using another trigger `HLT_Photon50_CaloIdVL_IsoL`. The photon candidates used in this photon efficiency study must pass our offline photon selection criteria shown in table 6.4. The HLT photon selection efficiency for p_T is defined as the fraction of offline reconstructed photons to those triggered by `HLT_IsoPhoton50` photon candidates within $\Delta R < 0.5$. Similarly, the \cancel{E}_T HLT efficiency is defined as the fraction of events containing at least a jet and \cancel{E}_T more than the HLT required \cancel{E}_T of 25 GeV . The results of the trigger efficiency measurements are shown in figure 6.8 against photon p_T and \cancel{E}_T . These efficiency studies are made using the `HLT_Photon50_CaloIdVL_IsoL` trigger which has no \cancel{E}_T and jet multiplicity requirement as the denominator and the `HLT_DisplacedPhoton65_CaloIdVL_IsoL_PFMET25` as numerator. A `SinglePhoton` dataset is used to verify these efficiency while and GMSB and $\gamma +$ jets samples is used to derive any correction factors between data and MC events.

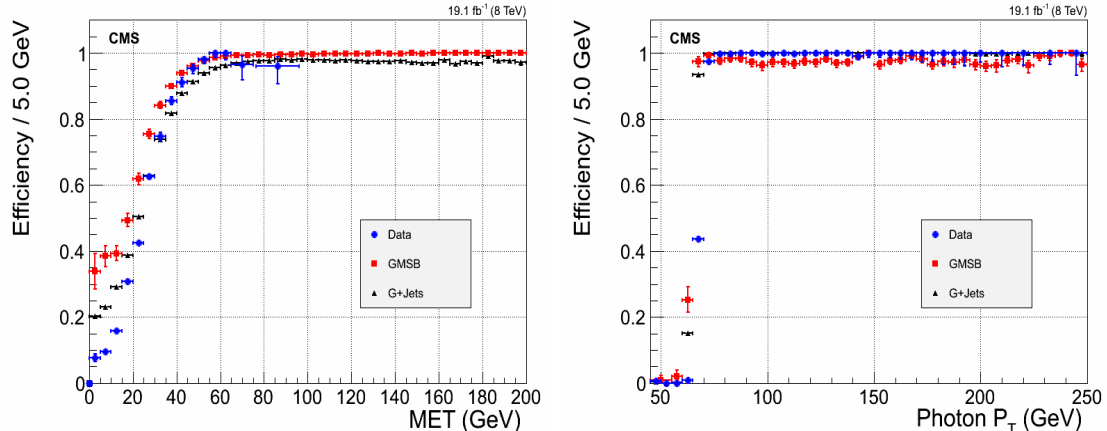


Figure 6.8: Trigger efficiency turn-on curves for photon p_T and $E_T^{\text{miss}} > 25 \text{ GeV}$ (left) and for \cancel{E}_T with photon (right). The $\gamma +$ jets samples require photon $p_T > 170 \text{ GeV}/c$ for selecting events with true \cancel{E}_T .

6.2.2 Offline Selection

In addition to the HLT selection, we apply an offline event selection on the photon, jets and \cancel{E}_T of these events.

The leading photon of an event must have a p_T greater than $80 \text{ GeV}/c$ while other photons candidates of the same event must have $p_T > 45 \text{ GeV}/c$. Because the particle flow (PF) algorithm does not consider out-of-time isolated photon energy deposits, we do not use the PF photon isolation criteria but rather a *simple cut-based* isolation requirement where we request that there should be no tracks near the selected photon within a range in $\Delta R(\gamma, track) < 0.6$, tracker, ECAL and HCAL isolation based on the photon p_T and E_T must be within the accepted range required by the simple cut-based approach. The ration of the photon energy deposited in HCAL to ECAL must be less than 5% and the photon shower shape along the minor axis (S_{Minor}) must be be within 0.12 and 0.38. To prevent double counting with jets with high electromagnetic energy component, the photon must be isolated from any other particle in a cone size of $\Delta R(\gamma, track) < 0.4$. We only selected photons belonging to the barrel (EB) region i.e. $|\eta_\gamma| < 1.479$ since we observed that an overwhelming large number of large ECAL time photon candidates from ghost/satellite bunch collisions belong to the endcap (EE) as seen in Figure 6.7 of a photon ECAL time comparison between photon candidates belonging to EB and EE. Our photon selection requirement is summarized in Table 6.4.

For jets, we select jets reconstructed with the PF algorithm based on the standard jet id selection criteria presented in Table 6.5. We require the leading jet in the event to have a p_T of at least $35 \text{ GeV}/c$. As for missing transverse energy (MET) selection, with inspiration from our trigger event selection efficiency plot in MET in Figure 6.8, we observed that a missing energy of at least 60 GeV for \cancel{E}_T and \cancel{E}_T^γ is enough to suppress $\gamma +$ jets and QCD events with fake missing transverse energy.

In summary, our signal events should have $\geq 1 \gamma + \geq 2 \text{ jets} + \cancel{E}_T > 60 \text{ GeV} + \cancel{E}_T^\gamma > 60 \text{ GeV}$. We use control samples(zero and one jet events since these events dominate our background sample, see Figure 6.2.2) to study the different sources of background.

Photon Identification and Selection Criteria	
Criteria	Requirement
Event leading photon must have $p_T(\gamma^1)$	$> 80 \text{ GeV}$
Other photons in event must have $p_T(\gamma^{>1})$	$> 45 \text{ GeV}$
$ \eta_\gamma , (\text{Barrel Only}),$	$< 3.0 (< 1.5)$
S_{minor}	$0.12 \leq S_{\text{Minor}} \leq 0.38$
\mathbf{H}/\mathbf{E}	< 0.05
$\Delta R(\gamma, \text{track})$	> 0.6
HCAL Iso	< 4.0
ECAL Iso	< 4.5
Track Iso	< 0.2
Photon Isolation cone size $\Delta R(\gamma, \text{otherparticle})$	< 0.4
Topological Spike cuts	$1 - E_6/E_2 < 0.98, 1 - E_4/E_1 < 0.98$

Table 6.4: The photon identification and selection criteria used in this analysis

Jet PF identification selection criteria	
Criteria	Requirement
Jet p_T	$> 35 \text{ GeV}$
Number of Jet constituents	> 1
Charge EM energy fraction (CEF)	> 0.99
Neutral Hadron energy fraction (NHF)	< 0.99
Neutral EM energy fraction (NEF)	< 0.99
If $ \eta $ of jet is > 2.4 , Charge Hadron energy fraction (CHF)	> 0
If $ \eta $ of jet is > 2.4 , Charge multiplicity (NCH)	> 0
$\Delta R(\gamma, \text{jet}) = \sqrt{(\phi_\gamma - \phi_{\text{jet}})^2 + (\eta_\gamma - \eta_{\text{jet}})^2}$	> 0.3
E_T, \not{E}_T	$> 60 \text{ GeV}$

Table 6.5: The Jet ID and MET selection used in this analysis

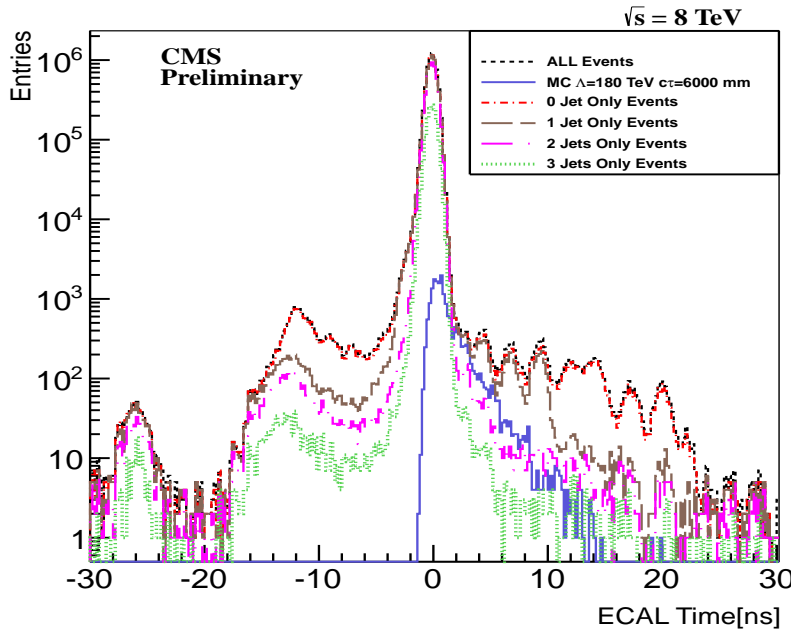


Figure 6.9: Photon with $p_T > 60$ GeV from data ECAL time distribution of events with different jet multiplicity and a single GMSB sample.

6.3 Background Estimation

The main source of background is not from photon candidates produced in normal pp collisions but rather from out-of-time photon candidates arising from non-collisions. To understand these out-of-time background events, we compare in-time ($|t_\gamma| < 1$ ns) photon candidates to out-of-time ($t_\gamma < -3$ ns and $t_\gamma > 2$ ns) photon candidates. We also compare photons candidates from different jet multiplicity events to better understand the different background sources and their contributions. In Figure 6.10, we present scatter plots of the photon's ECAL time against η (left) and against ϕ (right) for photons passing a loose ($p_T < 60$ GeV, barrel and endcap inclusive, $\cancel{E}_T > 25$ GeV) event selection criteria. We observe that, although most of the photons arrive with ECAL time about zero, a good number of photon candidates possibly from very different sources, for example the cross-like feature seen in the plot on the left, have large ECAL time. We

conclude that the possible sources of background photon candidates with large ECAL time measurements are mainly from beam halo muons, cosmic muons and spikes. A small addition also comes from photon candidates arising from ghost/satellite bunch collisions and some QCD events. To avoid, an irreducible contribution from spikes overpopulating a region with photon time, $t_\gamma \approx -12$ ns, we restrict our definition for out-of-time photons to photons with ECAL time $2.0 < t_\gamma < 13.0$ ns and $-10.0 < t_\gamma < -3$ ns. As a result, we only search for signal events with photon(s) having ECAL time between $2.0 < t_\gamma < 13.0$ ns, with at least 2 jets and large \cancel{E}_T .

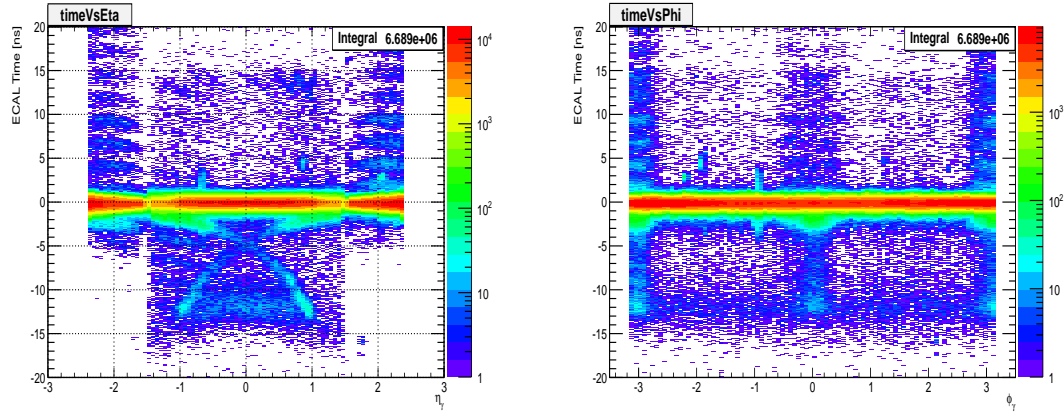


Figure 6.10: ECAL time against η (left) and ECAL time against ϕ (right) for photons with $p_T > 60$ GeV from data.

In our background estimation analysis, we first identify and reject photon candidates from beam halo, cosmic muons and spikes and then estimate the residual non-collision and collision background photon candidates using the **ABCD** background estimation technique.

6.3.1 Collision Background

QCD Photons

Events from satellite/ghost proton bunches spaced in 5.0 ns or 2.5 ns described in section 3.1.4, produce out-of-time photons which can be present in EB. We refer to these photons

as QCD photons. It is challenging to define a strategy for eliminating this background. Our approach, after rejecting non-collision events, was to estimate their contribution to signal using the ABCD background estimation method. Using Z events, we perform an additional background estimation of large ECAL time photon candidates from collision confirming our expectation that contribution from QCD photon events including true pp collisions events is almost negligible. More on this is discussed in future sections.

6.3.2 Non-Collision Background

Non-collision background events mainly cosmic muons, beam halo muons and spikes, have photons with large reconstructed time and large \cancel{E}_T measurements. The high p_T photons from these energetic muons and possible overlapping pile up events from multiple pp collisions, contribute to the total sum of the PF reconstructed p_T imbalance leading to their large \cancel{E}_T and at times jets associated with these events. We select events with at least one good vertex, zero or one jet, photons satisfying ECAL spike cleaning, associated with candidate muons satisfying DT time cosmic muon cleaning and CSC tight halo-muon cleaning requirements to study these non-collision events. A schematic diagram in Figure 6.11 show the production of photons from both non-collision and collisionghost/satellite in a typical LHC pp collision within the CMS detector. Also shown is a typical photon from a neutralino decay in the GMSB model. Still on the diagram is shown the point of entry of beam halo muons into the CMS detector comparing to what is observed in the photon ECAL time against η and ϕ plots of Figure 6.10.

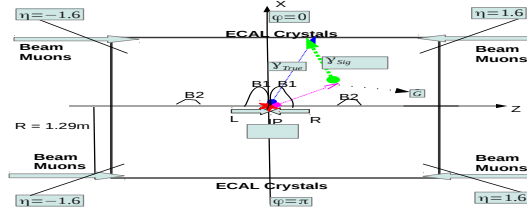


Figure 6.11: Schematic diagram showing production of photons from main pp and possible ghost/satellite bunch collisions in the CMS detector volume. Typical beam halo muon's entry direction into ECAL and GMSB neutralino decay is shown.

Halo Photons

Protons in the main and ghost/satellite bunches can scatter off tertiary collimators (TCT) about $z = 150$ m from CMS interaction point producing pions which later decay into muons traveling with energy of about a few TeV. These energetic muons bremsstrahlung in the calorimeter detectors producing high energy photons called *Halo photons*. Halo photons can also arise from energetic muons produced through inelastic scattering of the protons in the colliding bunches with residual gas molecules of gases like H₂, CO₂ in beam pipe about 550 m up from interaction point (IP). These halo producing protons although traveling parallel with the main proton bunch stir away from the nominal orbit in the transverse direction due to betatron oscillations. Despite beam cleaning, there still remains a good amount of them present and capable of producing energetic photons in ECAL spreading mostly in the horizontal plane as can be seen in the photon ECA time *v.s* ϕ scatter plot presented in the right plot of Figure 6.10. In general, events arising from beam related activities are referred to as *Machine Induced Background* (MIB) or *Beam-Induced Background* (BIB) events. The rate of halo photons in BIB events depends on the beam current and the operational conditions of the LHC, like the machine optics, collimator settings, residual gas densities and filling scheme. The halo muons in BIB events, although having slightly lower energy than the main proton beams, equally travel parallel to the proton beam but are deflected most by the

deflecting magnets. This deflection is mostly in the horizontal plane and the muons before entry into the ECAL, produce hits which can be reconstructed into muon tracks using segments in the Cathode Strip Chambers (CSC) Endcap muon detectors. The reconstructed hits in CSC segments can be associated with the halo photon supercluster in ECAL within some narrow region in ϕ . The geometry of ECAL allows most of the halo muons in the ECAL endcap regions with a few in the barrel. The resulting halo photons are usually out-of-time compared to photons produced directly from nominal pp collisions. Most of the halo photons have earlier arrival time and their arrival time can be estimated from the unique flight path of the halo muons. We estimated the halo muon arrival time in ECAL with respect the arrival time of photons from pp collisions as

$$t_{\text{ECAL}}^{\text{expected}} = -1/c \left(\pm Z_{\text{cluster}} + \sqrt{Z_{\text{cluster}}^2 + R_{\text{cluster}}^2} \right) \quad (6.6)$$

where Z_{cluster} is the point where the halo muon hits ECAL or longitudinal distance along z -axis from nominal interaction point, R is the radial distance of the cluster from the beam line which is 1.29 m and c is the speed of light. Our estimated halo muon ECAL arrival time shown in Figure 6.12, as the two red lines, agree well with the observed halo photon arrival ECAL time especially for earlier arrival time photons. It is much better to see this agreement once the expected halo muon arrival time equation is re-arrange to show its explicit dependence on η , which is the point of entry in ECAL given as

$$t_{\text{ECAL}}^{\text{expected}} = -\frac{R}{2c} \exp(-\eta) \quad (6.7)$$

By matching halo muon hit positions in CSC segments to photon supercluster positions in the ECAL calorimeter in ϕ , since halo muons spread mostly in the horizontal or azimuthal (ϕ) direction by the deflecting magnets, we are able to associate halo muons to their corresponding halo photons. We use the variable, $\Delta\phi(\text{CSC Seg}, \gamma)$, which is the difference in ϕ between CSC segment and the photon supercluster position in ECAL. A distribution of $\Delta\phi(\text{CSC Seg}, \gamma)$ for in-time and out-of-time photons in the left plot of Figure 6.12 show that out-of-time photons have small $\Delta\phi(\text{CSC Seg}, \gamma)$.

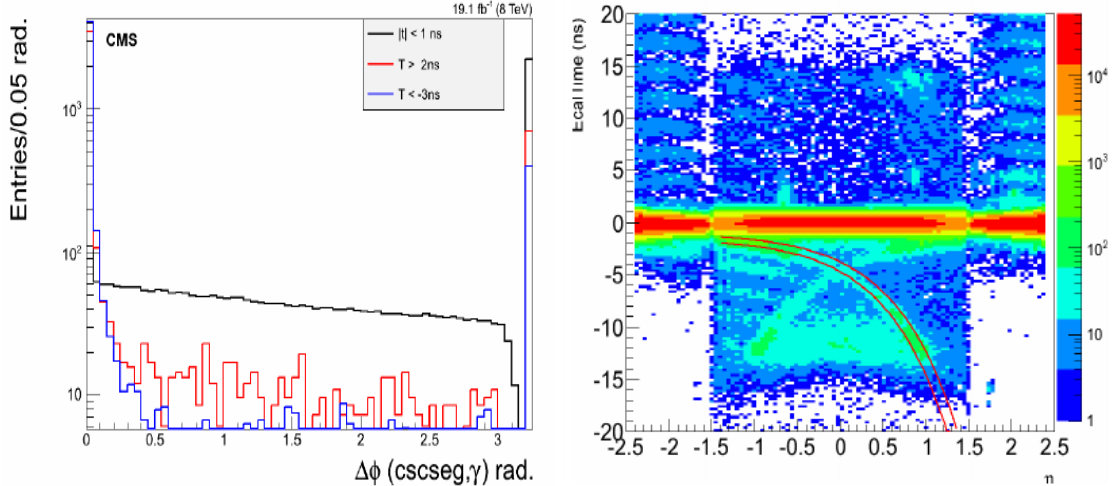


Figure 6.12: (Left) ECAL time $V.s$ $\Delta\phi(\text{CSC Seg}, \gamma)$ for in time(black) and out-of-time(red and blue) photons. (Right)Photon ECAL time $V.s$ η , expected halo photon time is shown as two red lines.

To estimate the performance of using $\Delta\phi(\text{CSC Seg}, \gamma)$ for halo tagging, we use a halo photon candidate sample by selecting photons with ϕ_γ around $\phi = 0, \pm\pi$ and in the endcaps where we expect mostly halo photon candidates. We were able to tag a good number of photon candidates as halo photons in the endcaps shown in the Figure 6.13 comparing halo photons in EE with tagged halo photons in EE with $\Delta\phi(\text{CSC Seg}, \gamma) < 0.05$.

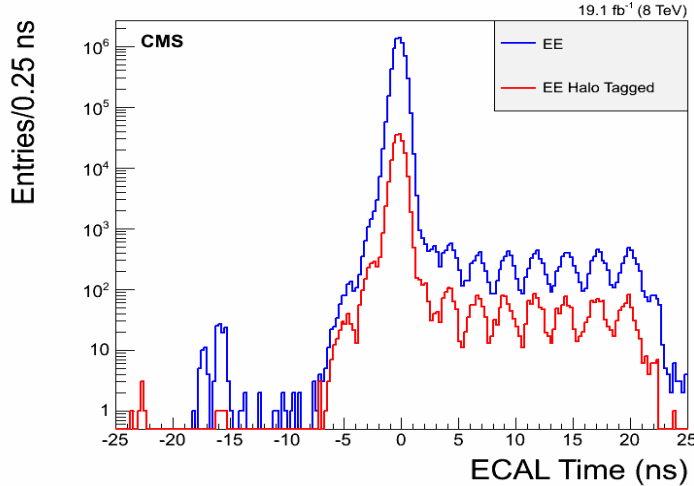


Figure 6.13: Using $\Delta\phi(\text{CSC Seg}, \gamma) < 0.05$ to tag photons with $\phi_\gamma = 0, \pm\pi$ in the endcaps. A good portion of endcap photon candidates are tagged.

Cosmic Photons

Cosmic muons like beam Halo muons with sufficient energy will also radiate (bremsstrahlung) photons in ECAL. We refer to these photons as *cosmic photons*. Unlike halo muons, cosmic muons can arrive at ECAL from any direction. Cosmic photons in the barrel are expected to be produced from cosmic muons with hits in the Drift Tubes (DT) segments. Using DT segments and photon supercluster $\eta - \phi$ position in ECAL, we can match cosmic muon hits in DT segments to ECAL photon superclusters within $\Delta\eta$ and $\Delta\phi$. The DT position used in calculation of $\Delta\eta$ and $\Delta\phi$ is a projection of the muon trajectory using the direction of the DT segment to the outer surface of ECAL due to the large space between the muon barrel and the ECAL. The two dimensional distribution for $\Delta\eta(\text{DT Seg}, \gamma)$ and $\Delta\phi(\text{DT Seg}, \gamma)$ of this matching for events with out-of-time photons; $t_\gamma > 2$ ns and $t_\gamma < -3$ ns is shown in the right plot of Figure 6.14. We compared to $\Delta\eta(\text{DT Seg}, \gamma)$ and $\Delta\phi(\text{DT Seg}, \gamma)$ distribution for in-time ($|t_\gamma| < 1$ ns), shown in the left plot, still in Figure 6.14, we observed that most out-of-time photons have a small $\Delta\eta$ and $\Delta\phi$. Comparing the $\Delta\eta$ and $\Delta\phi$ 2-dimensional distributions of these out-of-time photons to photons from a pure cosmic muons sample (data taken when no proton-proton collisions is happening), we found a similar small $\Delta\eta$ and $\Delta\phi$ occupancy by true cosmic muons sample, shown in Figure 6.15. We conclude that small

$\Delta\eta(\text{DT Seg}, \gamma)$ and $\Delta\phi(\text{DT Seg}, \gamma)$ can be used to tag and reject events with cosmic photons.

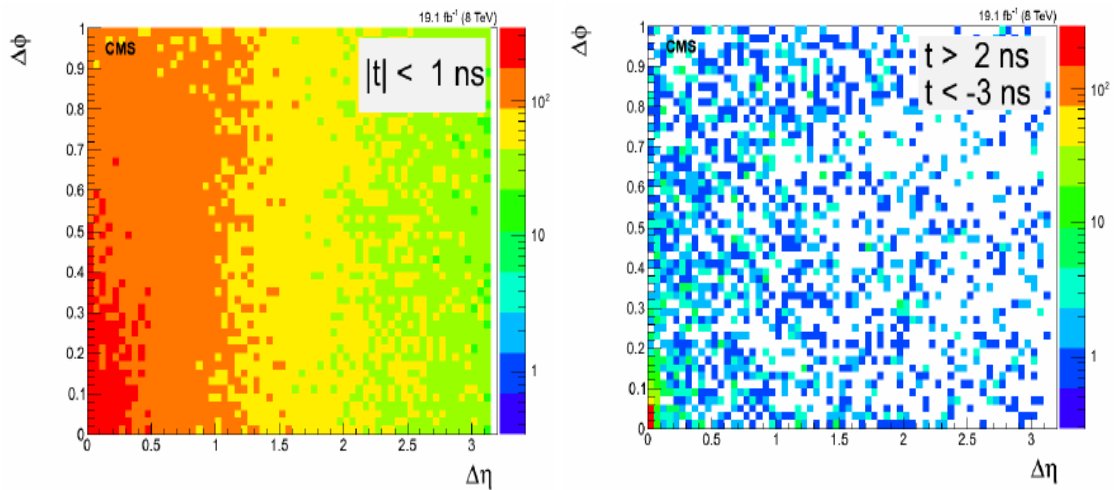


Figure 6.14: Scatter plot showing $\Delta\eta(\text{DT Seg}, \gamma)$ against $\Delta\phi(\text{DT Seg}, \gamma)$ for out-of-time ($t_\gamma > 2$ ns and $t_\gamma < -3$ ns) photons(Right) compared to in-time($|t_\gamma| < 1$ ns) photons(Left). Cosmic photon candidates occupy the small $\Delta\eta$ and $\Delta\phi$ region.

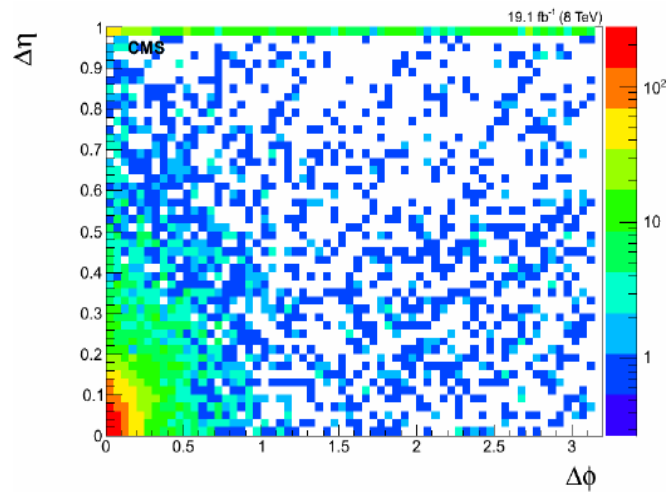


Figure 6.15: Scatter plot of $\Delta\eta(\text{DT Seg}, \gamma)$ against $\Delta\phi(\text{DT Seg}, \gamma)$ for photons from pure cosmic muon data. Small $\Delta\eta$ and $\Delta\phi$ are cosmic photons.

Anomalous Photons: Spikes

Neutrons and charge hadrons can at times deposit their energy directly to the APDs rather than through crystal scintillation. The signals read from the APDs are *anomalous* and referred to as *spikes*. Spikes are produced from pp collisions and can be easily misidentified for real isolated photons passing photon selection criteria. A spike supercluster consists of very few crystals; most often one or two crystals. Spikes can also overlapped with real photons and found embedded in a real photon supercluster or buried inside high electromagnetic fraction jets. Such embedded spikes are difficult to identify. By looking at the signal pulse height, the pulse shape for a spike signal appear different from a real photon signal. As a result, reconstructed ECAL time for spikes usually have a large calculated χ^2 value.

Because of the absence of crystal scintillation, the arrival time of spikes is much earlier (negative), usually about $t \approx -12.0$ ns than true photons produced in nominal pp collisions with crystal scintillation. The few crystals containing the spike cluster energy deposits makes it possible for spikes to be easily identified using a energy topological selection variable, $1 - \frac{E_4}{E_1}$, also known as *swiss-cross* variable. By looking at a distribution of the swiss-cross for in-time and a spike candidate sample(mostly photons with time $t = -12$ ns, shown in right plot of Figure 6.16, we observed than most spikes have about 98% of their energy deposited in a single crystal. Using the number of crystals in photon supercluster and comparing in-time photons to a beam halo photons and spike candidate photons (see left plot in Figure 6.16), we confirmed that most spikes including spikes embedded in electromagnetic candidates have less than 7 crystals in their supercluster. A combination of the swiss-cross, number of crystals in supercluster, calculated χ^2 , S_{major} and S_{minor} (both S_{major} and S_{minor} describe the shape of the electromagnetic shower), are useful in identifying and rejecting events with spikes.

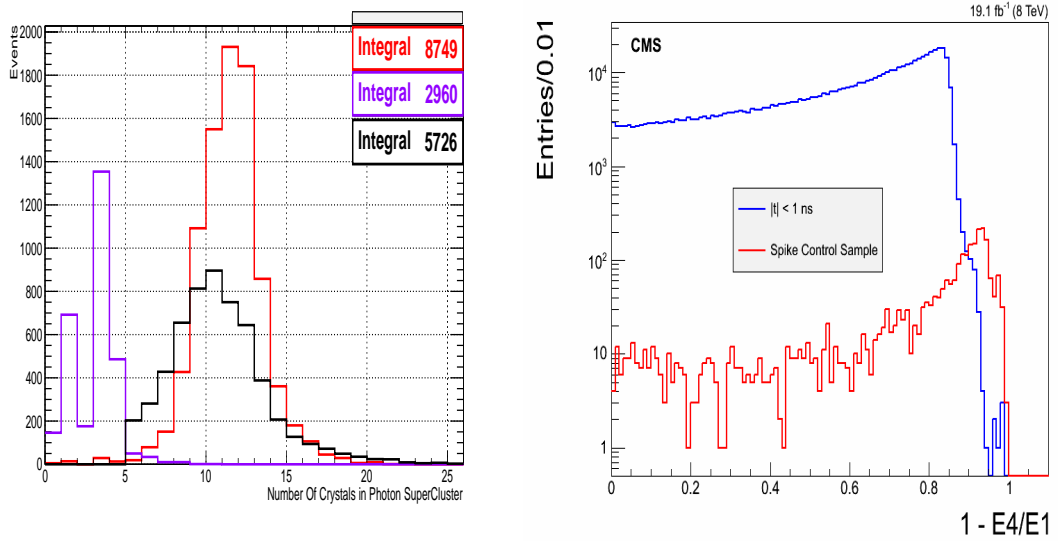


Figure 6.16: *Number of crystals* in photon supercluster plot (Left) for real photons candidates(black), spike photon candidates (magenta) and halo photon candidates (red). The spike photon candidates are selected with an energy swiss-cross variable ($1 - E_4/E_1$) (Right) shown comparing in-time photons ($|t_\gamma| < 1.0$) to spike candidate sample.

6.3.3 Event Cleaning, Veto Performance and Fake Rates

Using the selection variables studied above for halo, cosmic and spike photons, we tag and reject non-collision events as follows:

- Beam halo photons are tagged and rejected if a CSC segment with $|\eta| > 1.6$ is found within 0.05 radian of the azimuthal angle with a photon supercluster, i.e. photons found within $\Delta\phi(\text{CSC Seg}, \gamma) < 0.05$ are rejected. We found that we are able to reject halo photons with 91% efficiency and 3% mis-tag rate using this photon selection requirement.
- Cosmic photons are tagged and rejected with 75.5% efficiency and 1.4% mis-tag rate for photons associated with DT segments within $\Delta\eta(\text{DT Seg}, \gamma) < 0.1$ and $\Delta\phi(\text{DT Seg}, \gamma) < 0.1$.
- Most of spikes are rejected if the photons has $\chi^2 > 4$, Number of Crystals < 7 and $1 - E_4/E_1 > 0.98$, with only 0.4% mis-tag rate.

Our full veto performance in terms of mis-tag rate for the different non-collision background sources studied is summarized in Table 6.9.

Background Source	Fake Rate(%)
<i>Halo Photons</i>	≈ 3
<i>Cosmic Muons</i>	≈ 1.4
<i>Spikes</i>	≈ 0.4

Table 6.6: Fake rates for different non-collision cleaning.

The performance of the tagging and rejection of non-collision background events, shown in Figure 6.17, contains residual out-of-time background(in red) which could not be tagged. In order to estimate this residual out-of-time background, we use a ABCD background estimation technique.

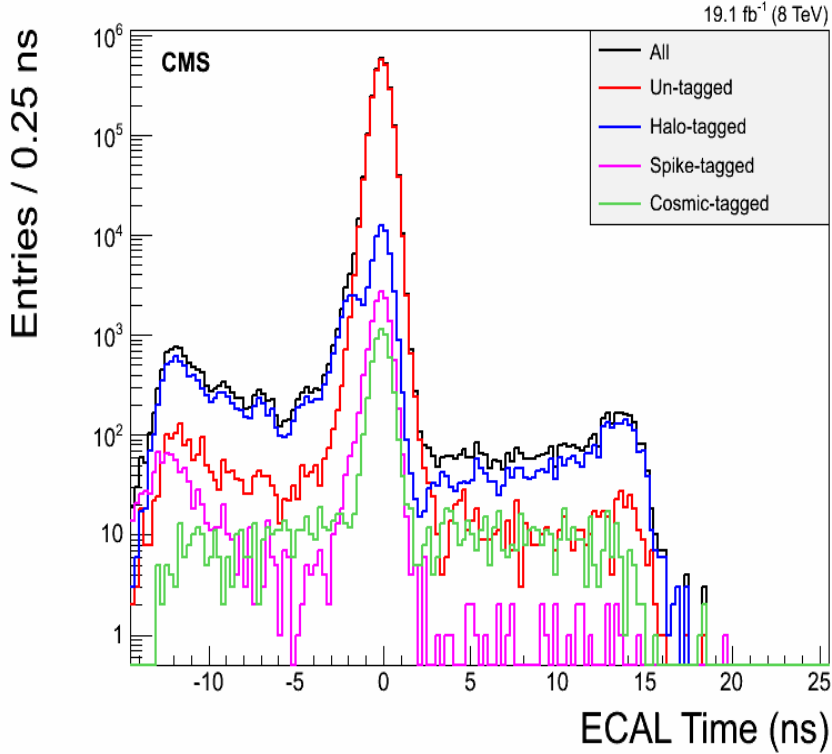


Figure 6.17: Residual Background(red) after tagging the different non-collision background sources using the selection variables described in text.

6.3.4 Background Estimation with ABDC Method

We estimated the residual background from collision and non-collision events using control regions defined with \cancel{E}_T , \cancel{E}_T^γ and photon ECAL time, t_γ . Signal photons must have photon arrival time; $3.0 < t_\gamma < 13.0$ ns, and the event must have large \cancel{E}_T . By large \cancel{E}_T , we mean events with $\cancel{E}_T^\gamma > 60$ GeV, $\cancel{E}_T > 60$ GeV. Non-collision events as already seen can also have large time, since they are mostly out-of-time and by \cancel{E}_T calculation and corrections(see discussion above) should have large \cancel{E}_T^γ and small \cancel{E}_T . Events from collision on the other hand are produced mostly in-time ($-2.0 < t_\gamma < 2.0$ ns) except in cases of timing mis-measurements or ghost/satellite contributions where $t_\gamma > 3.0$ ns. Collision events, mostly produced through SM interactions, cannot be produced with large correctly calculated \cancel{E}_T , e.g. $\gamma +$ jets events are produced with very small \cancel{E}_T , however due to timing mis-measurements, they may appear out-of-time and assigned

large \cancel{E}_T . Thus we conclude that collision events will generally have small \cancel{E}_T but large \cancel{E}_T^γ . We select control samples (CS) defined by \cancel{E}_T , \cancel{E}_T^γ and t_γ according to the ABCD technique to estimate our background contributions while remaining vigilant and taking into account the possible contamination to each background source from possible fluctuations in event rate as a result of our selection cuts in defining these CRs. The overall estimation technique is verified through a closure test procedure and the collision background estimation is validated using an extra control sample of $Z \rightarrow e^+e^-$ events for Z candidates reconstructed from photon candidates extended to include out-of-time events.

1. $\cancel{E}_T^\gamma > 60 \text{ GeV}$: CS in which collision (QCD) background is suppressed while halo, cosmic ray and spike photon is enhanced since most non-collision background photons are produced with high p_T hence large \cancel{E}_T^γ . Using this CS, we define four regions for estimating the non-collision background contribution using the ABCD recipe.

Non-Collision	$E_T < 60 \text{ GeV}$	$E_T > 60 \text{ GeV}$
$3.0 < t_\gamma < 13.0 \text{ ns.}$	C	D
$-10.0 < t_\gamma < -3.0 \text{ ns}$	A	B

Table 6.7: ABCD Control Regions (CRs) for estimating non-collision background.

Thus, the number of events expected in Control Region (CR) D using table 6.7 with the assumption that $\frac{N_D}{N_B} = \frac{N_C}{N_A}$ is given as:

$$N_D = \left(\frac{N_B}{N_A} \right) \cdot N_C \quad (6.8)$$

2. $\cancel{E}_T > 60 \text{ GeV}$: CS where non-collision background (halo, cosmic and spike photons) contribution is suppressed while collision (QCD) background contribution is enhanced. Further dividing this CS and applying $A' B' C' D'$ method to estimated collision contribution is shown in Table 6.8.

Collision	$\not{E}_T < 60 \text{ GeV}$	$\not{E}_T > 60 \text{ GeV}$
$3.0 < t_\gamma < 13.0 \text{ ns.}$	C'	D'
$-2.0 < t_\gamma < 2.0 \text{ ns}$	I'	I
$-10.0 < t_\gamma < -3.0 \text{ ns}$	A'	B'

Table 6.8: $A' B' C' D'$ and $I' I$ CRs for estimating collision background.

Using CRs defined in Table 6.8, we can estimate the contributions of collision background in both CRs B and D of our non-collision background CS as follows:

$$N_B^{col} = N_{B'} = \left(\frac{I}{I'} \right) \cdot N_{A'}, \quad N_D^{col} = N_{D'} = \left(\frac{I}{I'} \right) \cdot N_{C'} \quad (6.9)$$

where we have assumed that $\frac{N_{B'}}{N_{A'}} = \frac{N_L}{N_{I'}}$ and $\frac{N_{D'}}{N_{C'}} = \frac{N_L}{N_{I'}}$.

N_B^{col} and N_D^{col} are collision contributions to CRs B and A . The final combined background estimation is given by Equation 6.10.

$$N_D^{Total} = \left(\frac{N_B - N_B^{col}}{N_A} \right) \cdot N_C + N_D^{col} \quad (6.10)$$

where $N_D^{Total} = N_D^{non-col} + N_D^{col}$ is the total background estimation in our signal region.

Closure Test

Selecting events with 0-jets and 1-jet, we performed closure test of our background estimation method. We also perform a cross-check on the assumptions used in our background estimations for small contributions for collision background using $Z \rightarrow e^+ e^-$ events. Our underlying assumption here is that background contributions to large timing from collision source referred here as QCD is very small and must be of the order of 10^{-5} in comparison to in-time photons. i.e the ratio $N_{|t_\gamma|>3 \text{ ns}} / N_{|t_\gamma|<2.0 \text{ ns}} \approx 10^{-5}$ with N being the number of photons. The closure test compares the number of events observed in CR D to the number expected using our ABCD background estimation method in the same CR D . We observed 10 events while from using Equation 6.10, we expected $16.78^{+2.95}_{-3.45}$. We argue that within our statistical uncertainties, there is quite

an agreement between our expectation and observed events. The complete result from our closure test is shown in Table 6.9. This gives us confidence that our background estimation method is robust and reliable. We apply the same ABCD to estimate the background contribution in our signal sample. Our signal sample consist of events with at least 2-jets, at least a single photon and $\cancel{E}_T > 60 \text{ GeV}$, $\cancel{E}_T > 60 \text{ GeV}$

Non-Collision	$\cancel{E}_T < 60 \text{ GeV}$	$\cancel{E}_T > 60 \text{ GeV}$
$3.0 < t_\gamma < 13.0 \text{ ns}$	C(405)	D(10) 16.78
$-10.0 < t_\gamma < -3.0 \text{ ns}$	A(871)	B(36)
Collision	$\cancel{E}_T < 60 \text{ GeV}$	$\cancel{E}_T > 60 \text{ GeV}$
$3.0 < t_\gamma < 13.0 \text{ ns}$	$D'(4)$	D(10)
$-2.0 < t_\gamma < 2.0 \text{ ns}$	$F'(1353685)$	F(34543)
$-10.0 < t_\gamma < -3.0 \text{ ns}$	$B'(5)$	B(36)

Table 6.9: Result from closure test of background estimation technique using 0 and 1-jet events. Numbers in bracket represent our expected background estimate using ABCD method.

6.3.5 Background Estimation Cross Check

The main assumption in our background estimation technique is that, the contribution from collision background events to out-of-time regions ($3.0 < t_\gamma < 13.0 \text{ ns}$) is negligible. In order to show that this assumption is correct, we select $Z \rightarrow e^+e^-$ events from SingleElectron and DoubleElectron data sets of 2012. Our motivation is to use a control sample where contributions from non-collision events is very small. We select Z candidate events from an extended photon sample including out-of-time photon events according to the following selection criteria:

- The candidate two electrons for the Z bosons must have individual $p_T > 25 \text{ GeV}$,
- The di-mass of these two electrons, $|m_{e^+e^-} - 91| > 61 \text{ GeV}/c^2$,
- Each electron must be in the barrel, $|\eta_{e^-}| < 1.479$ and $|\eta_{e^+}| < 1.479$.

At the electron super cluster level, we used the seed crystal time adjusted to account for the electron time of flight, as the electron time. The seed crystal must satisfy the

recommended crystals or rechit cleaning criteria by the ECAL group which include `kWeird`, `kBad`, `kPoorCalib` used for rejecting crystals showing anomalous behavior like spikes, noisy, bad crystals or poorly calibrated crystals. In this cross-check, we define our signal region as Z -candidate events with a well defined mass from both electrons i.e $76 < |m_{e^+e^-}| < 100 \text{ GeV}/c^2$ while the non Z events control sample are events which do not fall into this signal category. A quick look at photon t_γ vs η_γ and ϕ_γ plots as previously shown for halo photons in figure 6.12, shows that the electron candidates from the `Single/DoubleElectron` dataset when compared to the `SinglePhoton` dataset in figure 6.18 show no or very little contribution from cosmic, halo and anomalous photon events. This confirms our choice of the Z candidate events sample as a reliable sample to study collision events as it is free from non-collision events.

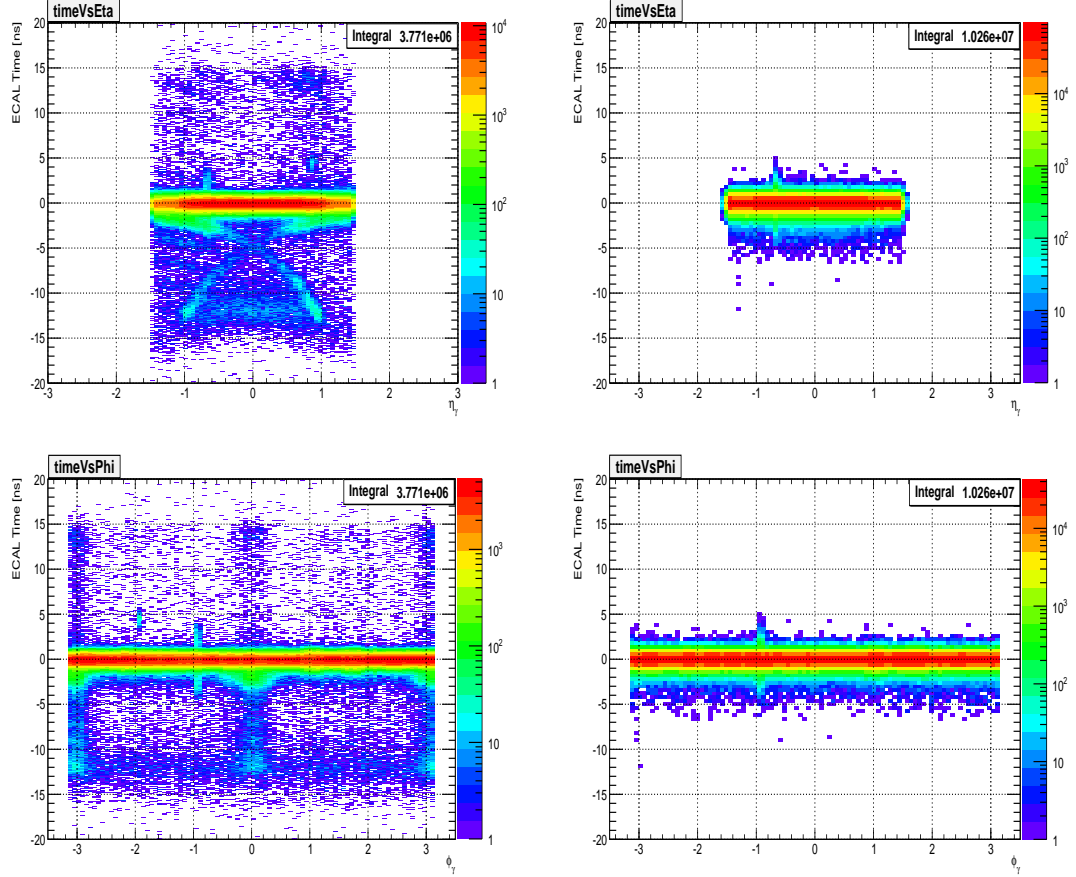


Figure 6.18: ECAL time, t_γ Vs η_γ (top) and t_γ Vs ϕ (bottom) for photons from SinglePhoton dataset (left) compared to electron candidates from the DoubleElectron dataset (right). All photons or electron candidates are in barrel subdetector. Most of the photons with $\phi = 0, \pm\pi$ are halo photons which are not observed in the Z boson candidate sample.

Figure 6.19 shows the Z boson mass reconstructed from the candidate electrons and timing of each electron for Signal (*top and blue*) and for our control sample (*bottom and red*).

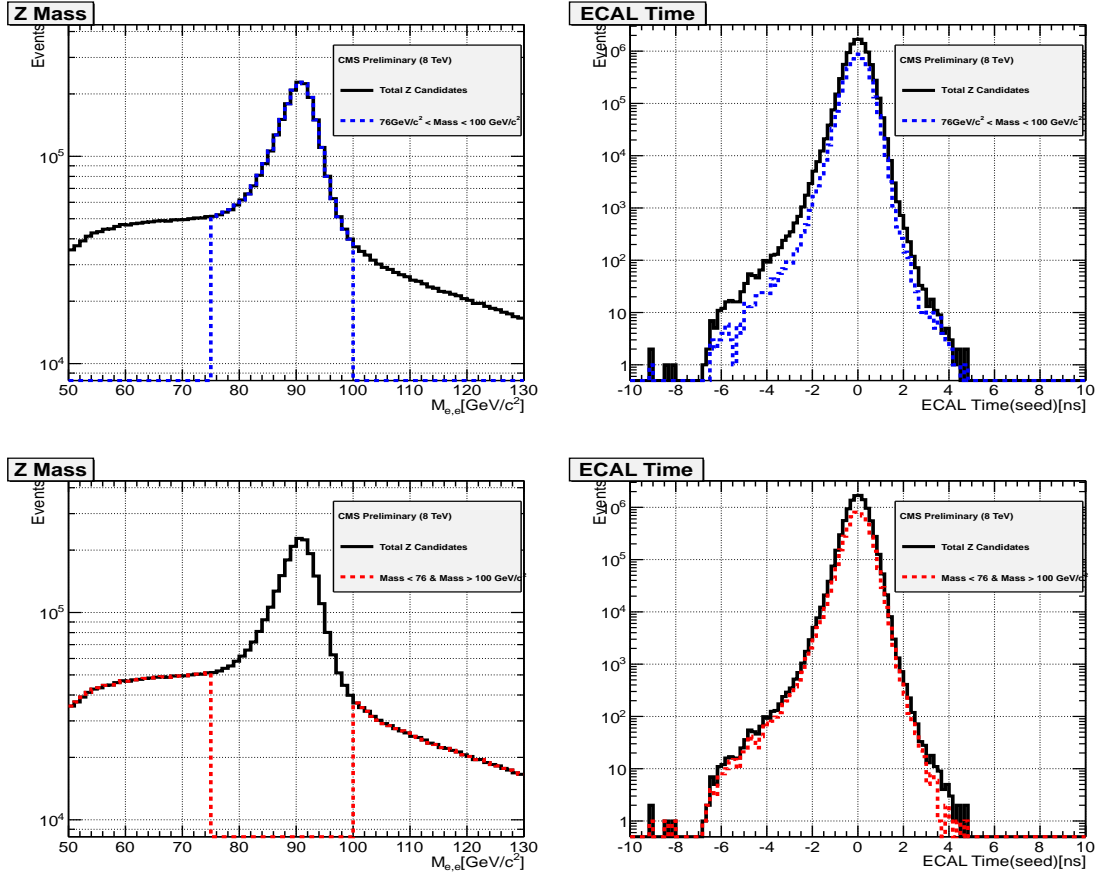


Figure 6.19: Di-electron candidate mass distribution and the time of both electrons for the signal $76 < m_Z < 100$ GeV/c² Z boson sample(left) and similar distributions from the Control ($50 < m_Z < 76$ GeV/c² and $100 < m_Z < 130$ GeV/c²) sample (right). Candidates events from the DoubleElectron dataset.

Using the background Z control sample, we estimate its contribution to out-of-time events using a simple scaling methods which can also be understood as an ABCD method. The method is applied as follows:

- Using a polynomial function, we fit the di-electron candidate mass distribution of the background control sample to extract a set of fit parameters,
- Using these fit parameters to define our polynomial function, we use this function

to extract a scaling factor use to determine the true contribution of the background control region events in the signal region which in this case are Z bosons with possible large ECAL timing, $|t| > 3$ ns.

- We scale the background control sample timing distribution (electrons time) using the extracted scale factor. This scale factor is defined as,

$$\text{Scale Factor} = \frac{N}{M_1 + M_2}$$

- By subtracting the scaled background control sample Z candidates timing distribution from the signal sample Z candidate timing distribution, we are left with the real Z boson events whose electron time can fluctuate into larger timing region.
- Comparing the total number of observe electron candidates with $t > 3$ ns to those in-time, $|t| < 2$ ns, their ratio i.e $N_{t>3\text{ ns}}/N_{|t|<2.0\text{ ns}}$ gives us an estimate of the possible genuine electromagnetic objects from collision with large ECAL timing.

A simple picture showing the above procedure with distributions is shown in figure 6.20.

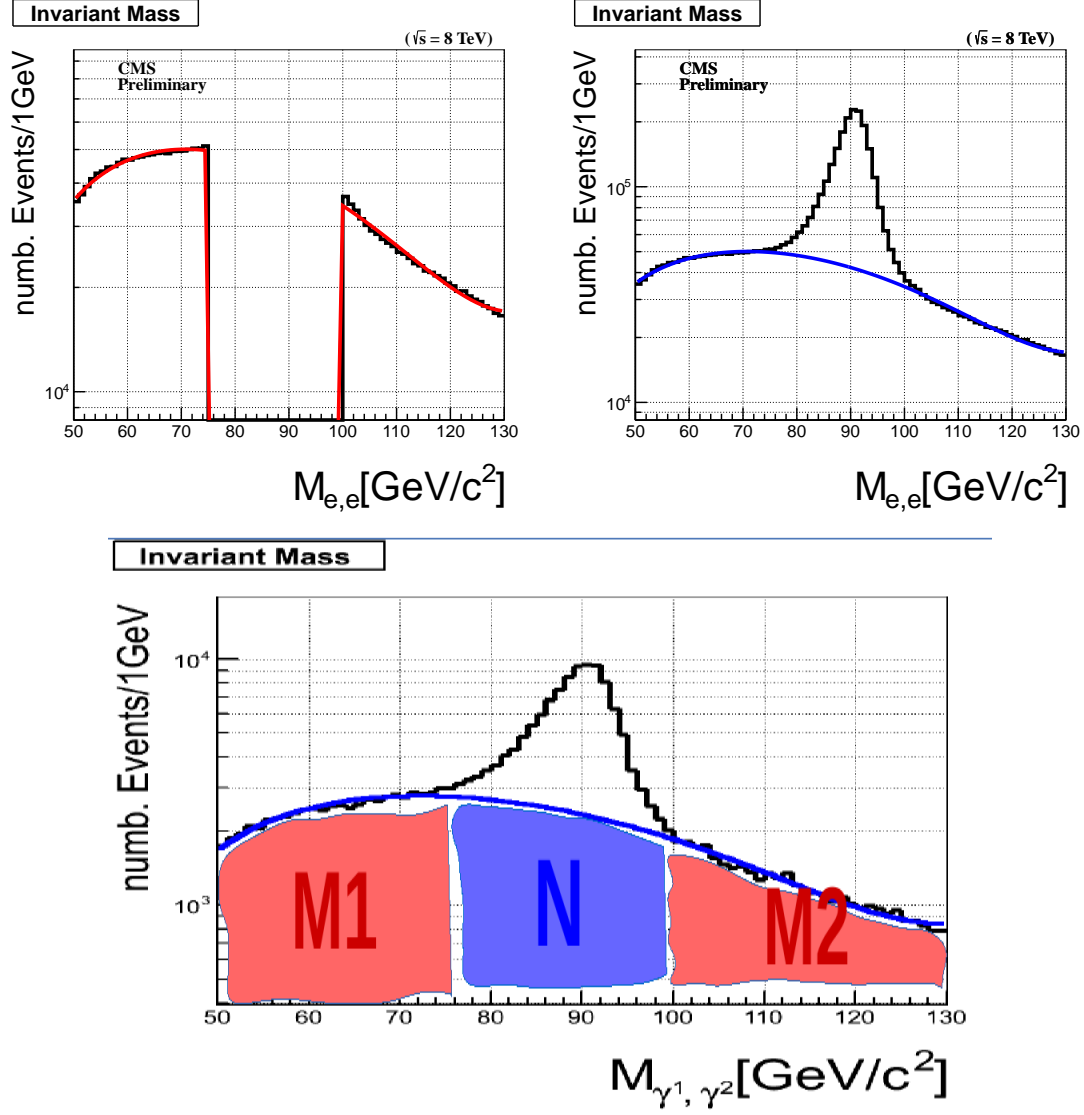


Figure 6.20: *Top*: Control sample (left) and signal sample (right) of di-electron candidate mass distribution. *Bottom*: Figure showing definition of scale factor use in estimating the contributions from control sample in signal sample.

The result of the final timing distribution for genuine Z boson events is shown in figure 6.21. It is not difficult to see that the ratio $N_{t>3 \text{ ns}}/N_{|t|<2.0 \text{ ns}} < 10^{-5}$ confirming that indeed the contribution of electromagnetic objects with large timing $t > 3 \text{ ns}$ is negligible and in agreement with our assumption that most collision events contain photons which

are mostly in-time, $|t| \leq 2$ ns. It's important to note that, we have not applied any E_T^{miss} selection cuts here. A simple cut, $E_T^{\text{miss}} > 60$ GeV could further reduce this ratio to an even smaller number as assumed in our above background estimation.

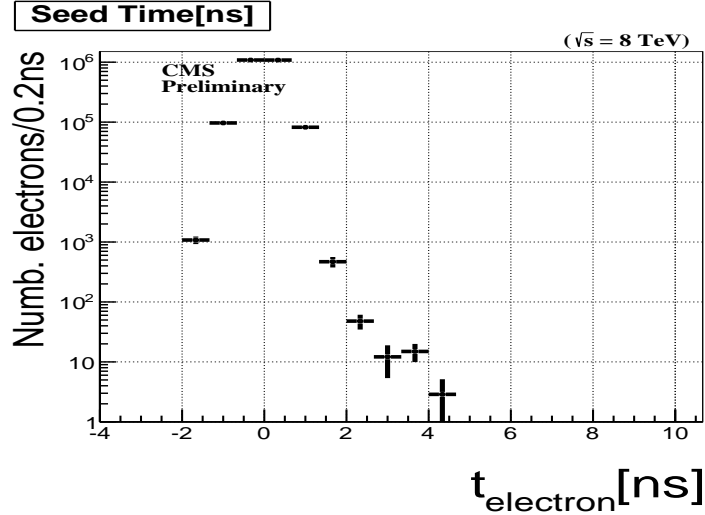


Figure 6.21: Timing distribution of genuine Z bosons after background contribution has been subtracted.

6.4 Systematic Studies

The different sources of systematic which affect this analysis and the estimated contribution of each identified source of systematic is shown in table 6.10. These systematic is also used in the calculation of the upper limit on observed signal cross-section. We obtained these systematic percentage by varying each individual source and see how that affects the number of events passing our selection cuts. The systematic uncertainty on luminosity measurement has the recommended value of 2.2% provided by CMS and LHC luminosity measurements. The uncertainty for the jet energy corrections (JEC) and jet energy scale (JES) has also been measured using the standard CMSSW tool by [52] and provided by the CMS JEMET working group. The uncertainty on the photon energy scale in barrel was estimated to be 1.0% and based on the final-state radiation (FSR) in $Z \rightarrow \mu\mu\gamma$ events [53]. The uncertainty from parton density functions (PDF) evaluated using the re-weighting technique using the Master Equation of CTEQ65 model set

described in [54]. The uncertainty on the E_T^{miss} resolution uses a conservative estimate from [55]. The uncertainty on the ECAL timing obtained by comparing the peak in the timing distribution between $\gamma + \text{jet}$ sample and data events with time $|t| < 2 \text{ ns}$ is found to be of the order of 200 ps per event and from a study of high p_T photons beyond gain transitions has agreed by ECAL DPG to be a conservative estimate. Another important source of systematic is in the selection of the background control samples and our background estimation and individual systematic in the tagging and miss-tagging of non-collision background and estimating background contributions from collisions. We combined these separate systematic contributions into a single background estimation systematic referred here as our background estimation systematic. This is our largest source of uncertainty in our analysis which we estimate to vary from 50% to 200%.

Source	Uncertainty on $\sigma_{UL}^{\text{Exp}}(\%)$
Photon energy scale (1.0%)	< 3.0%
Jet energy scale	< 0.05%
Jet energy resolution (10%)	< 1.90%
PDF uncertainty (10%)	< 1.70%
E_T^{miss} resolution (10%)	< 2.8%
ECAL time uncertainty (0.5 ns)	< 5.0%
Background estimation uncertainty (50.0)	< 51.0%
Luminosity (4.5%)	< 2.2%

Table 6.10: Summary of systematic uncertainties used in this analysis and applied to our cross-section upper limit, σ_{UL} calculation.

6.5 Results

Finally, we perform our background estimation on signal samples which are events with at least 2 jets, at least one high $p_T > 80 \text{ GeV}/c$ isolated photon with ECAL time $3.0 < t_\gamma < 13.0 \text{ ns}$ or $-10.0 < t_\gamma < -3.0 \text{ ns}$ and $\cancel{E}_T > 60 \text{ GeV}$, $\cancel{E}_T > 60 \text{ GeV}$. We observed 1 event and expected $0.0888^{+0.1869}_{-0.0444}$ background events within our statistical uncertainties. Our complete result is shown in table 6.11 and in table 6.12, we show the number of GMSB SPS8 signal events passing our final selection for $\Lambda = 180 \text{ TeV}$ with

different $c\tau$ values of the neutralino.

Non-Collision	$\not{E}_T < 60 \text{ GeV}$	$\not{E}_T > 60 \text{ GeV}$
$3.0 < t_\gamma < 13.0 \text{ ns}$	$C(0)$	$D(\textcolor{blue}{1})$
$-10.0 < t_\gamma < -3.0 \text{ ns}$	$A(5)$	$B(1)$
Collision	$\not{E}_T < 60 \text{ GeV}$	$\not{E}_T > 60 \text{ GeV}$
$3.0 < t_\gamma < 13.0 \text{ ns}$	$D'(5)$	$D \textcolor{red}{0.0888}^{+0.1869}_{-0.0444}$
$-2.0 < t_\gamma < 2.0 \text{ ns}$	$F'(657663)$	$F(30242)$
$-10.0 < t_\gamma < -3.0 \text{ ns}$	$B'(1)$	$B \textcolor{black}{0.23}^{+0.092}_{-0.118})$

Table 6.11: Result of observed events and estimated background from signal sample, events with at least 2-jets. Numbers in bracket represent our observed number of events while numbers not in bracket are our expected number of background events estimated using ABCD method.

SPS8 GMSB Signal	Number of Events
GMSB(SPS8) ($\Lambda = 180 \text{ TeV}, c\tau = 250 \text{ mm}$)	0.2096
GMSB(SPS8) ($\Lambda = 180 \text{ TeV}, c\tau = 500 \text{ mm}$)	4.5423
GMSB(SPS8) ($\Lambda = 180 \text{ TeV}, c\tau = 1000 \text{ mm}$)	6.3646
GMSB(SPS8) ($\Lambda = 180 \text{ TeV}, c\tau = 2000 \text{ mm}$)	6.3968
GMSB(SPS8) ($\Lambda = 180 \text{ TeV}, c\tau = 4000 \text{ mm}$)	6.1442
GMSB(SPS8) ($\Lambda = 180 \text{ TeV}, c\tau = 6000 \text{ mm}$)	4.6498
GMSB(SPS8) ($\Lambda = 180 \text{ TeV}, c\tau = 12000 \text{ mm}$)	2.918

Table 6.12: Final number for $\Lambda = 180 \text{ TeV}$ GMSB SPS8 MC signal events passing our selection cuts.

Chapter 7

Statistical Analysis

7.1 Limit Computation

The upper limit calculation procedure used in this analysis is the CLs technique. We fed carefully estimated amounts of background and signal with systematic to obtain the limit. The variable for which the 95% upper limit is set unlike previous experiments is based entirely on the neutralino proper decay length, $c\tau_{\tilde{\chi}_1^0}$.

The method we used in our upper limit calculation is by first performing a Hypothesis test and then use the result of this test to derived our confidence intervals. We do the following:

- We define a NULL hypothesis (H_0) and the Alternate hypothesis (H_1). If we had several other hypothesis, we will defined them also.
- Select a Test statistics ($t(x)$), where x is the data.
- Select a corresponding test statistics calculator.
- Use the result of the hypothesis test to compute the interval by inverting the result of the hypothesis test.

First, we describe the acceptable technique in experimental high energy physics for computing *p-values* used in any search and discovery experiment.

7.1.1 CLs Technique

The CL_s technique [59] is attributed as the standard technique or framework for computing the confidence or exclusion intervals in a search and discovery experiment. It has been shown to work during the search for the Higgs boson at LEP and recently in the discovery of the scalar boson in 2012, by both CMS and ATLAS experiments with the mass of this boson being: $m_H = 125.36 \pm 0.37(\text{stat.Unc}) \pm 0.18(\text{syst.Unc})$.

This method has been implemented in a unique statistical software package called *HiggsCombine* with the goal of providing direct access to a variety of robust statistical methods with optimised performance for computing limits or confidence intervals. *HiggsCombine* [61] is the official standard tool recommended by the CMS statistical committee and CMS Higgs group for calculating limits in any CMS search and discovery analysis. It takes as input estimates on the number or distribution of signal and background and the observed number or distribution from data and produces an upper limit in the production cross section of a given physics process for a given value of a parameter of interest (POI). *Higgscombine* tool has the advantage in that, it allows for the possibility to use several different statistical methods of calculating the upper limit. This way, one can make comparison and simple checks for any inconsistency. In this analysis, we used an Asymptotic [62] and HybridNew (a hybrid of Frequentist and Bayesian methods),[61], to calculate our observed upper limits. The purpose of the using the CL_s method is to compute reliable upper limits in a search scenario when the observed signal is very small compared to the background. In the CL_s technique, one uses not the p-value (CL_{s+b}) but rather divide this by CL_b (which is 1 minus the p-value for background only hypothesis). The reason for this is to define a conditional probability conditioned to the scenario of observing only background or background only hypothesis. The CL_s is formally defined as:

$$CL_s = \frac{CL_{s+b}}{CL_b} = \frac{p_{s+b}}{1 - p_b} \quad (7.1)$$

where $s + b$ means signal and background.

7.1.2 Statistical Test Formalism

The Neyman-Pearson Theorem states that the likelihood ratio gives the most powerful hypothesis test. Therefore, we construct our test statistics t_μ as a function of the observed data, as a likelihood ratio. In a search analysis, one defines the null hypothesis H_0 describing only known processes, or the background only which is to be tested against an alternate hypothesis H_1 defined as a background and signal. However in the computation of upper limits:

- H_0 being the NULL hypothesis includes the background and signal ($s + b$) while
- H_1 being the ALTERNATE hypothesis includes only the background (b).

Using these, two hypothesis we quantify the level of agreement between our observed data with either of the hypothesis by computing a p -value (p -value if the probability under the assumption of a given hypothesis, of finding data of equal or greater incompatibility with the predictions of the given hypothesis). A given hypothesis is then regarded as being excluded if its p -value is observed below a given threshold. In particle physics, this threshold value for the p -value is 0.05 corresponding to 95% of confidence level (CL). The CMS accepted method of computing upper upper limit is based on mix of frequentist-hybrid significance test using the profilelikelihood ratio as a test statistics (HybridNew method). The parameter of interests in in our case the rate (cross section) of signal process as well as *nuissance parameters* as systematics for the background and signal models. This parametrized systematics effects results, as is always the case, to loss in sensitivity.

In this search experiment, for each event in the signal, we measured the timing of the photon as our observable. We use this value to construct a histogram $\mathbf{n} = (n_1, \dots, n_N)$. The expectation value for each value of n_i can be written as:

$$E[n_i] = \mu s_i + b_i \quad (7.2)$$

where μ is the parameter which determines the signal strength, when $\mu = 0$ means background-only and when $\mu = 1$ then we have the signal and background hypothesis.

The the mean number of entries in the i th bin from signal and background are given as:

$$s_i = s_{tot} \int_{bin,i} f_s(t; \theta_s) \quad b_i = b_{tot} \int_{bin,i} f_b(t; \theta_b) \quad (7.3)$$

with the functions $f_s(t; \theta_s)$ and $f_b(t; \theta_b)$ being the probability density functions (Pdfs) of the variable t for the signal and background events and θ_s and θ_b representing the parameters which characterise the shapes of the pdfs. s_{tot} and b_{tot} represents the total mean numbers of signals and backgrounds while the integrals represent the probabilities for an event to be found in bin i . $\theta = (\theta_s, \theta_b, b_{tot})$ denote all nuisance parameters (systematic uncertainties) while s_{tot} is the signal normalization is fixed to the value predicted by the nominal signal model.

The likelihood function is the product of the Poisson probabilities for all bins:

$$\mathcal{L}(\mu, \theta) = \prod_{r=1}^N \frac{(\mu s_r + b_r)^{n_r}}{n_r!} e^{-(\mu s_r + b_r)} \cdot \mathcal{G}(\theta) \quad (7.4)$$

where $\mathcal{G}(\theta)$ is a discrete (Poisson) distribution of the nuisance parameters. This distribution can be different for different nuisance parameter.

Using the likelihood function, the profilelikelihood ratio is then defined as:

$$\lambda(\mu) = \frac{\mathcal{L}(\mu, \hat{\theta})}{\mathcal{L}(\hat{\mu}, \hat{\theta})} \quad (7.5)$$

Here $\hat{\theta}$ is the the value of θ that maximizes \mathcal{L} for a specified μ , thus, it is referred to as the *conditional maximum-likelihood estimator* (CMLE) of θ (given as a function of μ). While $\mathcal{L}(\hat{\mu}, \hat{\theta})$ is the maximized (unconditional) likelihood function with $\hat{\mu}$ and $\hat{\theta}$ being its *maximum likelihood* (ML) estimators. The nuisance parameters broadens the profilelikelihood as a function of μ relative to what is expected if their values where fixed and this reflects in the loss of sensitivity or information about μ due to the systematic uncertainties.

7.1.3 Test Statistics and p -values

The above expression for $\lambda(\mu)$ shows that $0 \leq \lambda \leq 1$, where λ close to 1 indicates a very good agreement between the data and hypothesis value of μ . The test statistics to be used for our statistical test is defined as:

$$t_\mu = -2 \ln \lambda(\mu) \quad (7.6)$$

It is important to note that the test statistics approach to any statistical test is favourable because just by looking at the values of the test statistics, higher values corresponds to increasing incompatibility between the data and the value of μ which is from the signal hypothesis. This incompatibility or disagreement between the data and a given hypothesis is quantified by calculating the probability or p -value as:

$$CL_{s+b} = p_u = \int_{t_{\mu,obs}}^{\infty} f(t_\mu|\mu) dt_\mu \quad (7.7)$$

where, $t_{\mu,obs}$ is the value of the test statistics t_μ obtained from the data and $f(t_\mu|\mu)$ is a pdf constructed from t_μ depending on the signal strength μ . The set of values for μ that are rejected because their p -value is below a specified threshold value α lying on either sides of those not rejected gives a two sided confidence interval of μ and if just on one side of the ones not rejected gives an upper limit on the rejected values of μ .

In the background only scenario i.e $\mu = 0$, the test statistics is defined as:

$$q_\mu = \begin{cases} -2 \ln \lambda(0), & \hat{\mu} \geq 0 \\ 0, & \hat{\mu} \leq 0 \end{cases}$$

where $\lambda(0)$ is the profilelikelihood ratio for $\mu = 0$ defined in 7.5. and again to quantify the disagreement between the background-only hypothesis ($\mu = 0$) and the data is given by the p -value as:

$$CL_b = p_0 = \int_{q_{0,obs}}^{\infty} f(q_0|0) dq_0 \quad (7.8)$$

where $f(q_0|0)$ denotes the pdf if the test statistics q_0 under the background-only ($\mu = 0$) hypothesis. Figure 7.1 shows a sampling distributions of the test statistics and how the

p-values can be extracted from these distributions.

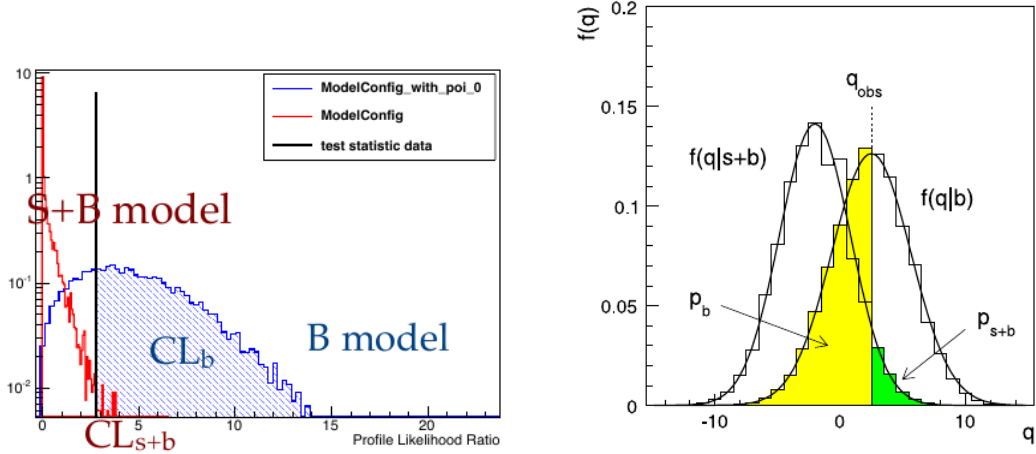


Figure 7.1: Sampling distributions for $f(t_\mu|\mu)$ showing how one extracts the p -values. left: is the using a analytic of the Asymptotic method and right: is from the HybridNew method.

In addition to the p -value, for expressing the disagreement between the data and a given hypothesis, the Higgscombine tool also provides a quantity known as the *significance* (\mathcal{Z}). \mathcal{Z} and the p -value have a very non-linear relation. Once can defined that relation using a two-sided fluctuation if a Gaussian variable σ , with 5σ significance corresponding to a p -value of $p = 5.7 \times 10^{-7}$ to denote a discovery. Since, we have not observed any significant excess of events over our standard model background, we will not mention a lot about significance in this thesis, but rather talk about p -values as they are indispensable in computing limits.

The important question is always, how does one obtain an expression or a distribution of the test statistics and $f(t_\mu|\mu)$ from the likelihood function? To answer this question, the HiggsCombine tool was developed which consist of various ways of both analytically (e.g the Asymptotic statistical method [62]) or through numerical integration or Monte Carlo computation (e.g the HybridNew statistical method) obtain the test statistics and $f(t_\mu|\mu)$. We have shown the limit computation results of both methods as used in this analysis. As an example, the pdf $f(q_\mu|\mu)$ of the test statistics (q_μ) obtained though the **Asymptotic** statistical method as given in [62] is:

$$f(t_\mu|\mu') = \Phi\left(\frac{\mu - \mu'}{\sigma}\right)\delta(t_\mu) + \frac{1}{2}\frac{1}{\sqrt{2\pi}}\frac{1}{t_\mu}\exp\left[-\frac{1}{2}\left(\sqrt{t_\mu} - \frac{\mu - \mu'}{\sigma}\right)^2\right] \quad (7.9)$$

where result to a half-chi-square distribution when $\mu = \mu'$.

In subtle point worth mentioning is that in the HybridNew approach, systematics uncertainties are taken into account through the Bayesian prior density $\pi(\theta)$, and the distribution of the test statistics is computed under the assumption if the Bayesian model of average given as:

$$f(q) = \int f(q|\theta)\pi(\theta)d\theta$$

and the prior pdf $\pi(\theta)$ is obtained from some measurements characterised by a given likelihood function $\mathcal{L}_\theta(\theta)$ which is then used to find the prior using Bayes' Theorem. Unlike other cases where systematic uncertainties are taking as being part of the data and incorporated directly through $\mathcal{G}(\theta)$ as shown in equation 7.4. Nevertheless, they arrive at the same result.

In summary, the hypothesis test is performed using a given statistical method on each value of a chosen parameter of interest (POI)(usually denoted μ). The p -value if obtained from the sampling distribution of the test statistics being used. Can either obtain this test statistics analytically or through Monte Carlo computation and numerical integration. By plotting the p-value as a function of the POI, we obtain the p-value curve (in this case the $CL_s = \frac{CL_{s+b}}{CL_b}$). The value of μ which has a p-value α (e.g 0.05) is the upper limit (for 1-dimensional limits,2-dimensional limits gives lower and upper limits) of $1 - \alpha$ confidence interval (e.g 95%).

combined result

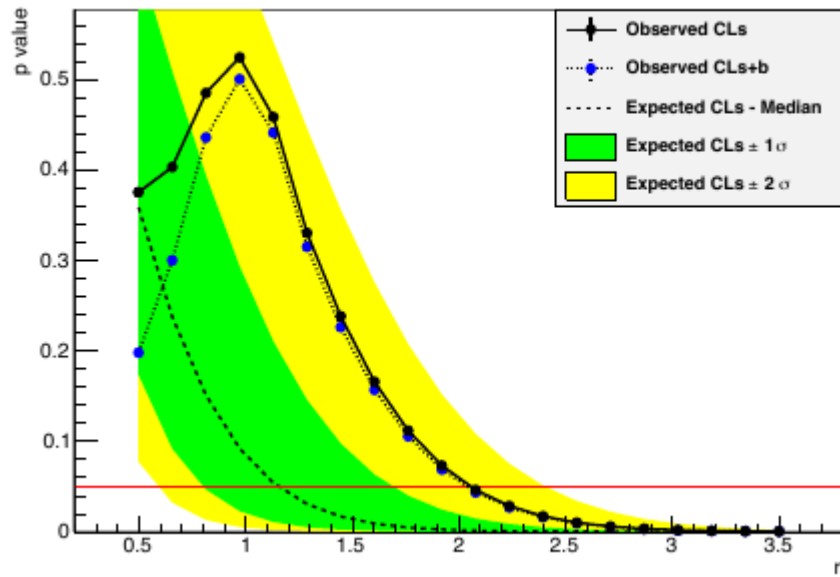


Figure 7.2: Distribution of p -values showing how upper limit on μ is extracted for a given threshold probability.

Chapter 8

Limit Interpretation

Using the CL_s technique, the HiggsCombine tool produces an upper limit along with the expected limit at different quantiles as the signal strength computed which is a ratio of Number of Signal events over the Number of Expected signal events i.e

$$r = \frac{N^{Obs}}{N_{expect}} \quad (8.1)$$

and using the equation as given in chapter 3 on the cross-section $\sigma = \frac{N}{\varepsilon \cdot A \cdot \mathcal{L}}$ and hence the observed cross-section upper limit is given as:

$$\sigma_{UL}^{Obs} = \frac{r \cdot N^{expect}}{\varepsilon \cdot A \cdot \mathcal{L}} \quad (8.2)$$

where \mathcal{L} is the integrated luminosity (19 fb^{-1}) and ε and A are the signal selection efficiency and Acceptance respectively. In addition to the observed limits (Solid black line), the uncertainties on the expected limits at 68%/16% ($\pm 1\sigma$) and at 98%/2.5% ($\pm 2\sigma$) provide the **GREEN** and **YELLOW** respectively, the error from the median (50%) expected limits (dashed red line) shown in figure 8.2.

8.1 Signal Efficiency and Acceptance

The efficiency times acceptance ($\varepsilon \times A$) combined as one is seen the figure 8.1.

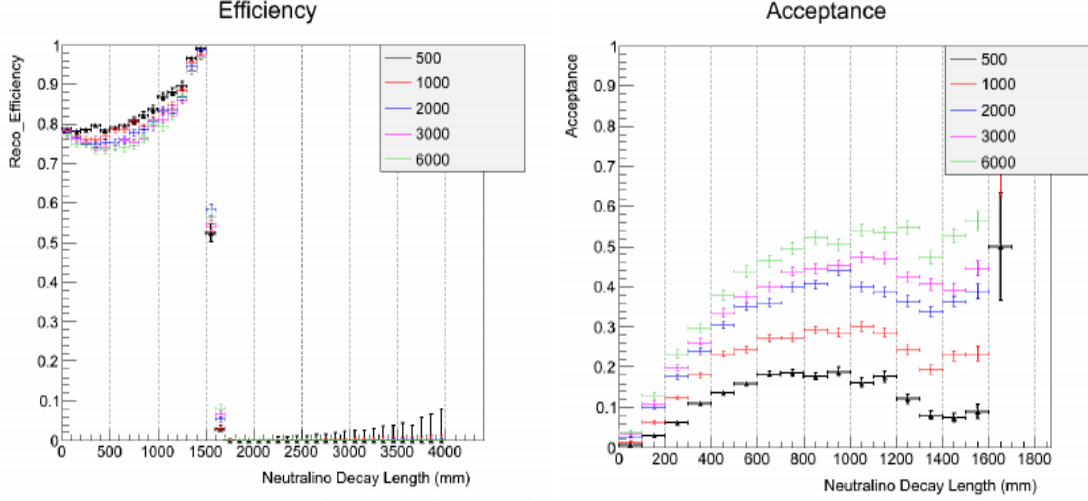


Figure 8.1: The reconstruction and selection efficiency (left) \times Acceptance ($t > 3$ ns) (right) against transverse decay length in laboratory frame for different $c\tau$ points.

The $\frac{N_{expet}}{\mathcal{L}}$ defines the expected signal cross section which is obtained from a given signal model. In our scenario, our choice of signal model we want to produce exclusion limits on the possible production and decay of a long-lived particle described by this signal model is GMSB. Thus the interpretation of our search analysis is given within the context of any GMSB model with a long-live neutral particle decaying to a photon and gravitino. Such a model is the minimal GMSB or the SPS8 model and the general GMSB model. However, the results provided are based on interpretation within the context of the SPS8 model. In GMSB, the neutralino $\tilde{\chi}_1^0$ is the NLSP and decays to the gravitino \tilde{G} the LSP (as a result of R-parity conservation) in association with a very energetic photon γ . Because of the smallness in mass difference between the $\tilde{\chi}_1^0$ and the \tilde{G} as well as the coupling, the $\tilde{\chi}_1^0$ decay to \tilde{G} is delayed and as a result, the photon emitted can arrive late in the calorimeter crystals. Measuring the arrival time of the photon on ECAL crystals, we can extract important parameters of theory of GMSB.

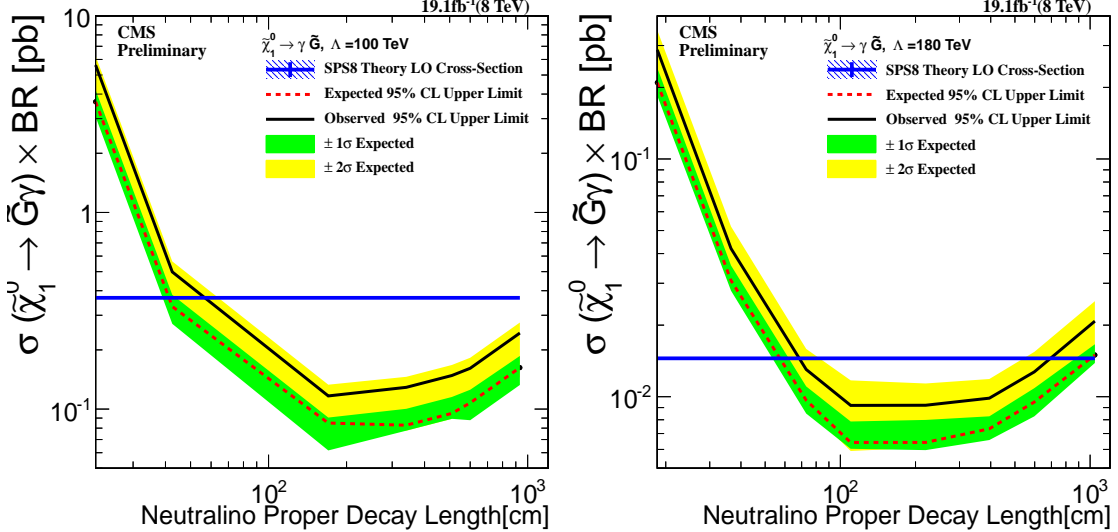


Figure 8.2: Neutralino production cross section against proper delay length upper limit interpretation in SPS8 model. (Left) $\Lambda = 100 \text{ TeV}$, (Right)(left) $\Lambda = 180 \text{ TeV}$

In the SPS8 model, the parameter space for long-live neutralinos is governed by $\Lambda_m - c\tau$ 2-dimensional parameter space. For each Λ_m point, we have a fixed neutralino mass with different proper lifetimes $c\tau$. We have obtained limits for Λ_m ranging from 100 TeV to 180 TeV corresponding to lightest neutralino mass $m_{\tilde{\chi}_1^0}$ between 90 to 255 GeV/c^2 and proper lifetime $c\tau$ ranging from 250 to 12000 mm corresponding to $\tau_{\tilde{\chi}_1^0}$ from 0.8 ns to 40 ns.

For a given value of $\Lambda_m = 180 \text{ TeV}$, we have a lightest neutralino production cross section times branching ratio plot shown in figure 8.2, showing that the ECAL detector is sensitive to lightest neutralinos of mass $m_{\tilde{\chi}_1^0} = 255 \text{ GeV}/c^2$ and life time upto 30 ns and we are 95% confident that we have not missed any neutralino whose mass is $m_{\tilde{\chi}_1^0} = 255 \text{ GeV}/c^2$ and lifetime is $\tau \leq 30 \text{ ns}$.

For a given lifetime of $\tau = 20 \text{ ns}$, we can also obtain upper limits on the production cross section times branching ratio when compared against their theoretically expected values for a lightest neutralino with mass ranging from $m_{\tilde{\chi}_1^0} = 90 \text{ GeV}/c^2$ to $m_{\tilde{\chi}_1^0} = 255 \text{ GeV}/c^2$. The observed upper limit on this cross section is $\sigma_{\tilde{\chi}_1^0}^{UP} \geq XX \text{ pb}$ with proper lifetime of $\tau = 30 \text{ ns}$.

Using both the mass and proper lifetime of the lightest neutralino, we present possible

2-dimensional limits simultaneously on $m_{\tilde{\chi}_1^0}$ or Λ_m and $c\tau$ or τ in the SPS8 model, comparing this with the result of previous experiments. This is shown in figure 8.3.

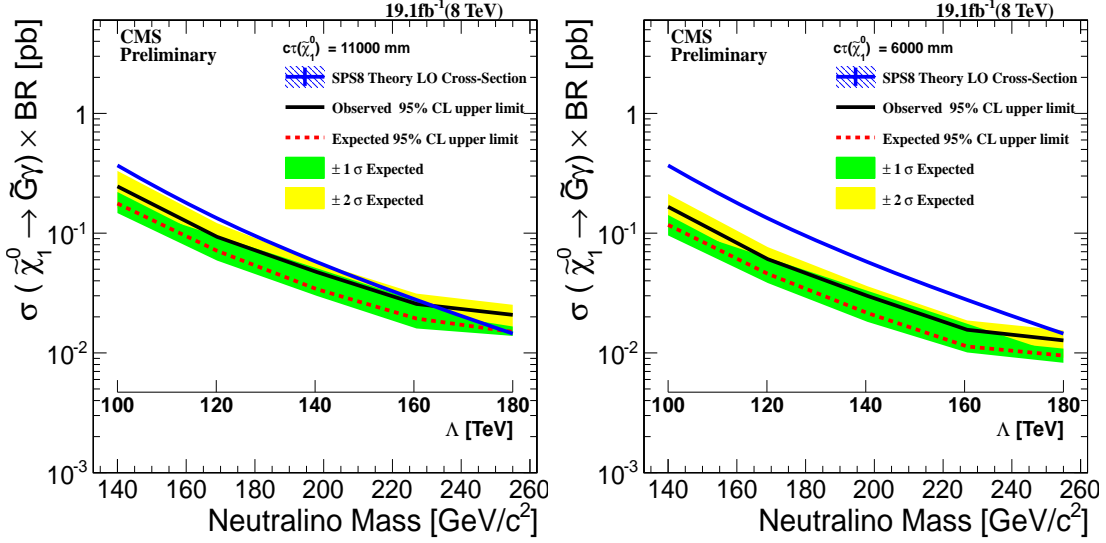


Figure 8.3: Neutralino production cross section against neutralino mass upper limit at 95% confidence levels interpretation in SPS8 model.(Left) $C\tau = 11000$ mm, (Right) $C\tau = 6000$ mm

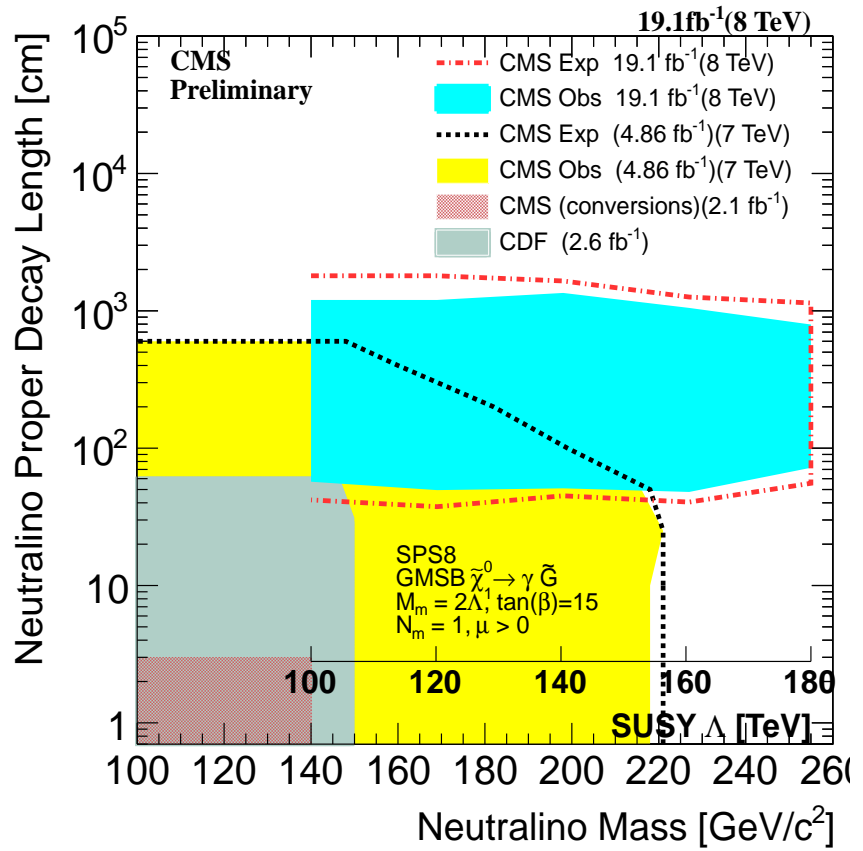


Figure 8.4: Neutralino two dimensional exclusion limit of neutralino mass (Λ) against proper delay length upper limit interpretation in SPS8 model in the decay $\tilde{\chi}_1^0 \rightarrow \gamma + \tilde{G}$ with limits from previous experiments shown.

Chapter 9

Conclusion

We have performed a search analysis for NMLLP decaying to photons using the time of arrival of the photon as measured by the ECAL sub detector of the CMS detector. Haven fail to find any significant signal of delayed photons over the standard model background, we interpreted our results in SUSY models with NMLLP like SPS8 of minimal GBSM or general GMSB models. We showed that, neutralinos whose production and decay mechanism is described in the SPS8 mGMSB model, with $m_{\tilde{\chi}_1^0} \leq 235 \text{ GeV}/c^2$ and $\tau_{\tilde{\chi}_1^0} \leq 35 \text{ ns}$ are ruled out of existence at 95% confidence level using the 2012 8 TeV LHC dataset. This corresponds to an upper limit of $\sigma_{\tilde{\chi}_1^0}^{UP} \geq 0.02 \text{ pb}$ on the production cross section times branching ratio in a hadron collider. In addition, we mention some of the limitations in this particular analysis from a detector point of view and how in future studies can be improved. We hope that in the future, with increase in center of mass energy of the LHC collider as well as luminosity and an improve in timing resolution beyond what is already very reliable, we will surely find a new fundamental particle whose dynamics cannot be described by the already very successful standard model of particle physics.

Bibliography

- [1] N. Jarosik et al. (WMAP), *Astrophys. J. Suppl.* **192**, 14 (2011); Overview: K.A. Olive et al.(PDG), *Chin.Phys.C***38**,090001(2014).
- [2] M. Kuhlen, M Vogelsberger, R. Angulo, *Phys.Dark Univ.***1**,50(2012).
- [3] Ellis John, Olive Keith A. (2010). “Supersymmetric Dark Matter Candidates”. arXiv:1001.3651 [astro-ph]
- [4] Laura Covi “Gravitino Dark Matter confronts LHC” *Journal of Physics: Conference Series* 485 (2014) 012002
- [5] J.Ellis, J.Hagelin, D. Nanopoulos, K.A. Olive and M. Srednicki; *Nucl. Phys.* B238 (1984) 453; H. Goldberg, *Phys. Rev. Lett* 50 (1983) 1419; J. Ellis, T. Falk, G. Ganis, K.A. Olive and M. Srednicki, *Phys. Lett. B* 510 (2001) 236, arXiv: hep-ph/0102098.
- [6] B.Allanach et al,arXiv:hep-ph/0202233v1;
- [7] “*Observation of a new boson at a mass of 125 GeV with the CMS experiment at LHC*”, *Phys. Lett. B* 716 (2012) 30-61
- [8] Steven Weinberg, “A Model of Leptons”, *Phys. Rev. Lett.* 19, 12641266 (1967)
- [9] “Observation of a Charged Charmoniumlike Structure in $e^-e^+ \rightarrow \pi^+\pi^-J/\psi$ at $\sqrt{S} = 4.26\text{GeV}$ ” M. Ablikim et al. *Phys. Rev. Lett.* 110, 252001 (2013), “Study of $e^-e^+ \rightarrow \pi^+\pi^-J/\psi$ and Observation of a Charged Charmoniumlike State at Belle”, Z. Q. Liu et al. *Phys. Rev. Lett.* 110, 252002 (2013);

- [10] Peter W. Higgs “Broken symmetries and the masses of gauge bosons”, *Phys.Rev.Lett.* 13.508, 19 October, 1964;
- [11] Haag,Rudolf; Sohnius, Martin; opuszaski, Jan T. “All possible generators of supersymmetries of the S-matrix”, *Nuclear Physics B* 88: 257274 (1975);
- [12] S.Mathin, arXiv:hep-ph/9709356;
- [13] Howard Baer, Xerxes Tata “Weak Scale Supersymmetry: From Superfields to Scattering Events”
- [14] S. Ambrosanio 1 , Graham D. Kribs 2 , and Stephen P. Martin hep-ph/9703211 arXiv:hep-ph/9703211v2.
- [15] G.F. Giudice and R. Rattazzi “ Theories with Gauge-Mediated Supersymmetry Breaking” arXiv:hep-ph/9801271v2
- [16] J.Dann et al.(LEPSUSY Working Group), Internal note LEPSUSYWG/97-04(1997), P. Janot, talk at the EPS Conference, Jerusalem, 1997.
- [17] CDF Collaboration, “Search for Supersymmetry with Gauge-Mediated Breaking in Diphoton Events with Missing Transverse Energy at CDFII “, *Phys. Rev. Lett.*
- [18] ATLAS Collaboration “Search for Diphoton Events with Large Missing Transverse Momentum in $1 fb^{-1}$ of 7TeV Proton-Proton Collision Data with the ATLAS Detector”, arXiv:1111.4116v1, 17th Nov 2011.
- [19] CMS Draft Analysis, “Search for Long-Lived Particles using Displaced Photons in PP Collision at $\sqrt{S} = 7TeV$ ”, CMS AN AN-11-081 104(2010)011801,
- [20] ATLAS Collaboration, J. High Energy Phys. 1212, 124 (2012), arXiv:1210.4457 [hep-ex]
- [21] The LHC Machine, Lyndon Evans and Philip Bryant *Jinst*,
- [22] CMS Collaboration, “CMS Physics: Technical design report, Volume 1” CERN-LHCC-2006-001
- [23] The CERN Brochure 2009-003-Eng

- [24] CMS Collaboration, “The CMS experiment at the CERN LHC”, JINST 0803:S08004, 2008.
- [25] CMS uses a right-handed coordinate system, with the origin at the nominal interaction point, the x -axis pointing to the center of the LHC, the y -axis pointing up (perpendicular to the LHC plane), and the z -axis along the counterclockwise-beam direction. The polar angle, θ , is measured from the positive z -axis and the azimuthal angle, ϕ , is measured in the x - y plane. $\eta = -\ln \tan(\theta/2)$. The transverse energy and momentum are defined as $E_T = E \sin \theta$ and $p_T = p \sin \theta$ where E is the energy measured in the tracking system. $E_T^{\text{miss}} = | - \sum_i E_T^i \vec{n}_i |$ where \vec{n}_i is a unit vector that points from the interaction vertex to the transverse plane.
- [26] “Timing Distribution at the LHC”, B.G. Taylor Colmar, 9-13 September 2002
- [27] “An FPGA based multiprocessing CPU for Beam Synchronous Timing in CERNs SPS and LHC”. *Proceedings of ICAL EPICS 2003, Gyeongju, Korea ICAL EPICS 2003*
- [28] “Timing and Synchronization in the LHC Experiments”, Varela, J. Krakv, 11-15 September 2000.
- [29] <http://ttc.web.cern.ch/TTC/intro.html>
- [30] “Study of the LHC ghost charge and satellite bunches for luminosity calibration.”, CERN-ATS-Note-2012-029 PERF
- [31] “LHC bunch current normalisation for the April-May 2010 luminosity calibration measurements.”, CERN-ATS-Note-2011-004 PERF
- [32] CMS Collaboration, “The electromagnetic calorimeter. Technical design report”,. CERN-LHCC-97-33
- [33] Bo Lofstedt, “The digital readout system for the CMS electromagnetic Calorimeter”, *Nucl. Inst. Methods in Physics Research*, A 453 (2000) 433-439
- [34] CMS Electromagnetic Calorimeter Collaboration, “Energy resolution of the barrel of the CMS Electromagnetic Calorimeter”, JINST 2(2007)P04004.

- [35] CMS Collaboration, “Time Reconstruction and Performance of the CMS Crystal Electromagnetic Calorimeter”, CFT-09-006, 2009.
- [36] <https://twiki.cern.ch/twiki/bin/viewauth/CMS/ECALDPGTimeCalibration>
- [37] <https://twiki.cern.ch/twiki/bin/viewauth/CMS/ECALDPGHWTimeCalibration>
- [38] CMS Collaboration, “The CMS ECAL performance With examples”, JINST 9 C02008, 2014.
- [39] CMS-DP-2014/011: “*ECAL Timing Performance Run1*”
- [40] <https://twiki.cern.ch/twiki/bin/view/CMSPublic/EcalDPGResultsCMSDP2014011>
- [41] <https://twiki.cern.ch/twiki/bin/view/CMSPublic/EcalDPGResultsCMSDP2014012>
- [42] “Characterization and treatment of anomalous signals in the CMS Electromagnetic Calorimeter” CMS AN AN-10-357
- [43] “ Mitigation of Anomalous APD signals in the CMS ECAL”, 2013, *JINST 8 C03020*, W.Bialas and D.A. Petyt
- [44] CMS Collaboration, “CMS trigger and data taking in 2010 ”, *CMS CR-2011/051*.
- [45] CMS Collaboration, “Reconstruction of the signal amplitude of the CMS electromagnetic Calorimeter”, Eur.Phys.J. C46S1(2006)23-35.
- [46] D.del Re et al “An algorithm for the determination of the flight path of long-lived particles decaying into photons” CMS AN -2010/212.
- [47] CMS Collaboration, “Particle-Flow Event Reconstruction in CMS and Performance for Jets, taus and \cancel{E}_T ”, CMS Physics Analysis Summary CMS-PAS-PFT-09-001(2009).
- [48] CMS Collaboration, Missing Transverse Energy Performance in Minimum-Bias and Jet Events from Proton-Proton Collisions at $\sqrt{s} = 7$ TeV , CMS Physics Analysis Summary CMS-PAS-JME-10-004 (2010).
- [49] MET JINST (arXiv:1106.5048)

- [50] CMS Collaboration, “Missing transverse energy performance of the CMS detector”; arXiv:1106.5048v1
- [51] CMS Collaboration, “CMS Physics: Technical design report, Volume 2” CERN-LHCC-2006-001.
- [52] CMS Collaboration, “Determination of Jet Energy Scale in CMS with pp collisions at $\sqrt{S} = 8$ TeV”, *JME-10-010(2012)*
- [53] “<https://twiki.cern.ch/twiki/bin/viewauth/CMS/EGamma2012>.”
- [54] “Parton distributions for the LHC” *Eur.Phys.J C63(2009) 189-285* or arXiv:0901.0002
- [55] CMS Collaboration, “Search for ADD Extra-dimensions with Photon + MET signature”, *AN-11-319(2011)*
- [56] ISAJET 7.84 F.E. Paige, S.D. Protopopescu, H. Baer and X. Tata, <http://www.nhn.ou.edu/~isajet/>
- [57] T. Sj ostrand, S. Mrenna, and P. Skands, PYTHIA 6.4 physics and manual, *JHEP 05 (2006) 026*, doi:10.1088/1126-6708/2006/05/026, arXiv:hep-ph/0603175
- [58] GEANT4 Collaboration, GEANT4a simulation toolkit, *Nucl. Instrum. Meth. A 506(2003) 250*, doi:10.1016/S0168-9002(03)01368-8.
- [59] “Presentation of search results: the CLs technique”, *A. L Read 2002 J. Phys. G: Nucl. Part. Phys. 28 2693*
- [60] “Computation of confidence levels for search experiments with fractional event counting and the treatment of systematic errors”, *Peter Bock JHEP01(2007)080*
- [61] <https://twiki.cern.ch/twiki/bin/viewauth/CMS/>
- [62] “Asymptotic formulae for likelihood-based tests of new physics” *G. Cowan et al, arXiv:1007.1727v3*
- [63] N.-E. Bomark and L. Roszkowski “3.5 keV x-ray line from decaying gravitino dark matter” *Phys. Rev. D 90, 011701(R)* Published 18 July 2014

Appendix A

Glossary and Acronyms

Care has been taken in this thesis to minimize the use of jargon and acronyms, but this cannot always be achieved. This appendix defines jargon terms in a glossary, and contains a table of acronyms and their meaning.

A.1 Glossary

- **Cosmic-Ray Muon (CR μ)** – A muon coming from the abundant energetic particles originating outside of the Earth’s atmosphere.
- **SUSY** – A theoretical model based on a fundamental symmetry called supersymmetry in which the fermions and bosons can exchange their spin, extending the standard model to account for the stability in the observed Higgs boson mass and to also predicting the existence of many extra new particles which could be candidates of dark matter.

A.2 Acronyms

Table A.1: Acronyms

NMLLP	Neutral Massive Long-Lived Particles.
DM	Dark Matter.
DE	Dark Energy.
GMSB	Gauge Mediated Supersymmetry Breaking
LHC	Large Hadron Collider
CMS	Compact Muon Solenoid
CR μ	Cosmic-Ray Muon